

**Enhancing the Noise Performance of Low Noise Amplifiers - With
Applications for Future Cosmic Microwave Background
Observatories**

A thesis submitted to the University of Manchester for the degree of Doctor of
Philosophy in the Faculty of Engineering and Physical Sciences

2013

Mark Anthony McCulloch

School of Physics and Astronomy

Contents

List of Figures	9
List of Tables	13
List of Abbreviations	15
Abstract	17
Declaration	19
Copyright	21
Acknowledgements	23
Preface	26
1 Low Noise Amplifiers (LNA) and Radio Astronomy	27
1.1 Radio Astronomy and the Importance of Amplification	28
1.1.1 The Radio Spectrum	28
1.1.2 Radio Receivers	28
1.1.3 Coherent Receivers	30
1.2 The Cosmic Microwave Background (CMB)	32
1.2.1 Early Work	33
1.2.2 Penzias and Wilson	36

1.2.3	CMB and CMB Anisotropies Observatories	36
1.2.4	Current Observational Aims	42
1.2.5	Polarisation Observatories	46
2	Low Noise Amplification and The Problem of Noise	49
2.1	Low Noise Amplifiers (LNAs)	50
2.1.1	Noise Figure and Gain	50
2.1.2	S Parameters	51
2.2	Semi-conductors	53
2.2.1	Band Theory	53
2.2.2	Doping	55
2.2.3	Electron Mobility	56
2.3	The Field Effect Transistor	56
2.3.1	Development	57
2.3.2	Heterostructure	57
2.3.3	The FET as an Amplifier	60
2.4	High Electron Mobility Transistors (HEMTs)	62
2.4.1	Basic Structure	64
2.4.2	Band Bending and the 2-DEG	65
2.4.3	The T-gate	67
2.5	The Equivalent Circuit	69
2.5.1	The Parameters	70
2.6	Noise	72
2.6.1	Sources of Noise	75
2.7	The Modeling of Noise	78
2.7.1	Noise Parameters	78
2.7.2	The Pospieszalski Equivalent Temperatures	80

3	Ultra Low Temperature Operations	83
3.1	Noise Temperature and Physical Temperature	84
3.1.1	Noise Parameters and Temperature	84
3.1.2	The Pospieszalski Temperature Parameters	85
3.2	The Cryostat	88
3.2.1	Layout	89
3.2.2	Thermal Break	89
3.2.3	Temperature Control and Monitoring	90
3.2.4	The 1 K Fridge	91
3.3	The Noise Test Set-up	92
3.3.1	The Noise Figure Meter	92
3.3.2	The Mixer	93
3.3.3	Local oscillator	94
3.3.4	Variable Temperature Load	94
3.3.5	Noise Source	95
3.3.6	The Y-factor	96
3.4	Drain Current and Temperature	97
3.5	Physical Temperature	99
3.5.1	JPL MMIC Amplifier	100
3.5.2	QUIJOTE 1.3	103
3.6	Uncertainties	105
3.7	Discussion	107
3.8	Conclusions	108
4	The Transistor in front of MMIC (T+MMIC) LNA	111
4.1	LNAs	111
4.1.1	MIC LNAs	112

4.1.2	MMIC LNAs	117
4.2	T+MMIC LNA	121
4.2.1	Theoretical Background	121
4.2.2	The Transistor and the MMIC	123
4.2.3	The LNA Module	124
4.2.4	Theoretical Noise Performance	127
4.3	Modeling	128
4.3.1	The Equivalent Circuit Parameters	129
4.3.2	The Faraday MMIC's S Parameters	130
4.3.3	Passive Components	132
4.3.4	The Model	136
4.4	Performance	138
4.4.1	27-33 GHz Performance	138
4.4.2	26-36 GHz (MMIC band) Performance	139
4.4.3	Stability	142
4.5	Discussion	143
4.5.1	20 K Physical Temperature Performance	143
4.5.2	Input Matching and Transmission Lines	143
4.5.3	Applications	145
4.6	Conclusion	145

5 Future Applications 147

5.1	Drawbacks to Cooling and the T+MMIC Approach	147
5.2	T+MMIC Version 2.0	150
5.2.1	First Stage Design	150
5.3	Potential Performance	155
5.4	Drain Temperature Investigation	156

6	Concluding Remarks and the Future	157
6.1	Conclusion	157
6.2	The Future	159
6.2.1	Increasing the Number of Receivers	159
6.2.2	Transistors	159
6.2.3	New Types of Amplifier	161
6.3	Closing Remarks	162
	Appendix A Derivation of the RMS Thermal Noise Voltage (V_n)	165
	Appendix B T+MMIC LNA Module: Designs	169
	Bibliography	175
	Number of Words: 45639	

List of Figures

1.1	Coherent and bolometer receiver systems	29
1.2	Illustration of the radiometer used by Penzias and Wilson	37
1.3	5 Year WMAP CMB angular power spectrum	39
1.4	The 9 year WMAP all sky map	40
1.5	The Planck all sky map	41
1.6	The development of a quadrupole radiation field	43
1.7	E and B mode polarization patterns.	45
2.1.1	The noise figure and gain of an amplifier	50
2.1.2	A basic 2 port network	51
2.2.1	The band structure of metals, semi-conductors and insulators	54
2.3.1	The structure of a GaAs based FET	57
2.3.2	Band diagrams illustrating the formation of the depletion region	59
2.3.3	The FET as an amplifier	61
2.3.4	Why FETs make good amplifiers	62
2.4.1	The relationship between electron mobility and temperature for a FET and a HEMT	63
2.4.2	The structure of a basic InP HEMT	64
2.4.3	Conduction and valence band characteristics at the hetero-junction be- tween 2 semi-conductors	66

2.4.4	A T-gate	67
2.4.5	SEM images of a Hughes $4 \times 25 \mu m$ HEMT	69
2.5.1	A small signal transistor equivalent circuit	71
2.5.2	A 3D transistor equivalent circuit	72
2.6.1	The voltage output of a resistor of resistance R at temperature T	73
2.6.2	A Thévenin equivalent circuit	74
2.6.3	Noise temperature of an amplifier	75
2.6.4	A simplified noise equivalent circuit	76
2.7.1	The Pospieszalski noise equivalent circuit	81
3.2.1	The layout of the 1 K cryostat	90
3.2.2	CAD images of the thermal break	91
3.3.1	Block diagram illustrating the noise test set up	92
3.3.2	Image of the noise test set-up	93
3.3.3	The variable temperature load	95
3.3.4	The Y-factor approach to measuring an LNA's noise temperature	96
3.4.1	Mean noise temperature with respect to drain current at various temperatures for the Planck EBB amplifier	98
3.4.2	Mean noise temperature with respect to drain current at various temperatures for the T+MMIC amplifier	99
3.5.1	The JPL MMIC LNA	101
3.5.2	JPL LNA: noise and gain performance at 6 K physical temperature	102
3.5.3	Mean noise temperature of the JPL MMIC from 2 K to 290 K	102
3.5.4	Image of the QUIJOTE 1.3 LNA	103
3.5.5	QUIJOTE LNA: noise and gain performance at 8 K physical temperature	104
3.5.6	Mean noise temperature of the Faraday LNA from 4 K to 290 K	105
3.6.1	Repeat measurements for the Planck EBB	106

4.1.1 A Microwave Integrated Circuit LNA	113
4.1.2 An MIC resistor and capacitor	113
4.1.3 Layout of a DC blocking capacitor	114
4.1.4 A cross-sectional view of a typical microstrip	115
4.1.5 Ka-band MMIC based LNA	120
4.2.1 The noise of a cascaded system	122
4.2.2 The T+MMIC's transistor and MMIC	124
4.2.3 Computer aided design image of the T+MMIC LNA's module	125
4.2.4 T+MMIC module pin identification	125
4.2.5 LNA RF circuit layout	127
4.2.6 The assembled T+MMIC LNA	127
4.3.1 A transistor equivalent circuit, suitable for use in Agilent's ADS	130
4.3.2 Signal flow diagram graphically illustrating the S parameters of the MMIC and the input and output fixtures	131
4.3.3 HFSS model of the QUIJOTE 1.3 input probe	133
4.3.4 Close up of the waveguide to microstrip probe transition	133
4.3.5 The simulated performance of the QUIJOTE module input and output probes	134
4.3.6 The ADS de-embedding circuit	134
4.3.7 The transmission line like behaviour of a bond wire	135
4.3.8 The full ADS 8 K model	137
4.4.1 Room temperature T+MMIC noise and gain performance	139
4.4.2 8 K T+MMIC noise and gain performance	140
4.4.3 The modelled and measured room temperature performance of the T+MMIC LNA across the MMIC's design band	141
4.4.4 The modelled and measured 8 K physical temperature performance of the T+MMIC LNA across the MMIC's design band	141

4.4.5 The Stability of the T+MMIC amplifier at 8 K	142
4.5.1 The noise temperature of the T+MMIC LNA at 19 K and 8 K, compared to the average noise temperature of the Planck amplifiers	144
5.1.1 Proposed layout for the discrete block approach to LNAs	148
5.1.2 Future multi-frequency transistor test cryostat	149
5.1.3 A next generation thermal break	149
5.2.1 Preliminary ADS design for a single transistor amplifier	152
5.2.2 Single stage HRL 2 x 50 μm HEMT based amplifier	153
5.2.3 HRL 2 x 50 μm single stage amplifier: stability	154
5.3.1 Potential performance of a future Ka-band T+MMIC (discrete block) LNA	155
6.2.1 A collapsed T-gate	160
6.2.2 An impression of an I-gate	161
6.2.3 A parametric amplifier	162
6.3.1 Dusk at QUIET	163
A.0.1A cuboidal blackbody cavity containing photons representing an ideal conductor	166

List of Tables

1.1	The Radio Spectrum	28
1.2	Advantages and disadvantages of coherent and incoherent radiometers . . .	30
2.1	The properties of some semi-conductors at 300 K	56
2.2	Electron mobility for a conventional GaAs MESFET and HEMT structure at 300 and 77 K	63
3.1	Comparison of the noise parameters of two FETs at 297 and 12.5 K	85
3.2	Fit statistics for the JPL amplifier	100
3.3	Fit statistics for the QUIJOTE amplifier	104
3.4	Noise Temperatures for 290 K, 20 K, 4 K and 2 K physical temperature for the JPL and QUIJOTE 1.3 amplifiers	108
4.1	Current state of the art LNAs for selected frequencies.	112
4.2	Dielectric constants and loss tangents for typically used dielectrics	116
4.3	The advantages and disadvantages of MICs and MMICs	119
4.4	The T+MMIC pin outs	126
4.5	The widths and lengths of the T+MMIC LNA's microstrip lines	126
4.6	Cryo-3 temperature dependent equivalent circuit parameters	129
4.7	Cryo-3 extrinsic and intrinsic equivalent circuit parameters	130
5.1	HRL 2x50 μ m HEMT extrinsic and intrinsic equivalent circuit parameters	151

List of Abbreviations

ADS Advanced Design System

BJT Bipolar-Junction-Transistor

CAD Computer Aided Design

CBI Cosmic Background Imager

CHOP Cryogenic HEMT Optimisation Program

CMB Cosmic Microwave Background

CMBR Cosmic Microwave Background Radiation

DASI Degree Angular Scale Interferometer

DUT Device Under Test

ENR Excess Noise Ratio

ESA European Space Agency

FET Field Effect Transistor

FIRAS Far Infrared Absolute Spectrometer

GaAs Gallium Arsenide

HEMT High Electron Mobility Transistor

HFSS High Frequency Structure Simulator

IEEE Institute of Electrical and Electronics Engineers

IF Intermediate Frequency

InP Indium Phosphide

JPL Jet Propulsion Laboratory

LFI Low Frequency Instrument

LNA Low Noise Amplifier

LO Local Oscillator

MESFET Metal-Semiconductor-Field-Effect-Transistor

MIC Microwave Integrated Circuit

MMIC Monolithic Microwave Integrated Circuit

MOSFET Metal-Oxide-Semiconductor-Field-Effect-Transistor

NASA National Aeronautics and Space Administration

NFM Noise Figure Meter

NGST Northrop Grumman Space Technologies

OMT Ortho-mode Transducer

QUAD QUEST at DASI

QUIJOTE Q-U-I-JOint-Tenerife-Experiment

RF Radio Frequency

T+MMIC Transistor in front of MMIC

Abstract

The University of Manchester

Mark Anthony McCulloch

Doctor of Philosophy Physics and Astronomy

**Enhancing the Noise Performance of Low Noise Amplifiers - With Applications for
Future Cosmic Microwave Background Observatories**

2013

Low Noise Amplifiers (LNAs) are one of the most important components found in some of the radio receivers used in radio astronomy. A good LNA should simultaneously possess both a gain in excess of 25 dB and as low a noise contribution as possible. This is because the gain is used to suppress the noise contribution of the subsequent components but the noise generated by the LNA adds directly to the noise of the overall receiver. The work presented in this thesis aimed to further enhance the noise performance through a variety of techniques with the aim of applying these techniques to the study of the polarisation of the Cosmic Microwave Background. One particular technique investigated was to cool the LNAs beyond the standard 20 K typically used in experiments to 2 K. In doing so it was found that the noise performance increased by between 20 and 30% depending on the amplifier. Another technique investigated involved uniting the two technologies (MICs and MMIC) used in LNA fabrication to lower the noise performance of the LNA. Such an LNA, known as a T+MMIC LNA was successfully developed and possessed an average noise temperature of 9.4 K and a gain in excess of 40 dB for a 27-33 GHz bandwidth at 8 K physical temperature. Potential “in field” applications for these technologies are discussed, and a design for a variant of the T+MMIC LNA that utilises both of these technologies is presented. This particular LNA with a predicted average noise temperature of 6.8 K for a 26-36 GHz bandwidth, would if fabricated successfully represent the lowest noise Ka-band LNA ever reported.

Declaration

I declare that no portion of the work referred to in the thesis has been submitted in support of an application for another degree or qualification of this or any other university or other institute of learning.

Copyright

The author of this thesis (including any appendices and/or schedules to this thesis) owns certain copyright or related rights in it (the Copyright) and s/he has given The University of Manchester certain rights to use such Copyright, including for administrative purposes.

Copies of this thesis, either in full or in extracts and whether in hard or electronic copy, may be made only in accordance with the Copyright, Designs and Patents Act 1988 (as amended) and regulations issued under it or, where appropriate, in accordance with licensing agreements which the University has from time to time. This page must form part of any such copies made.

The ownership of certain Copyright, patents, designs, trade marks and other intellectual property (the Intellectual Property) and any reproductions of copyright works in the thesis, for example graphs and tables (Reproductions), which may be described in this thesis, may not be owned by the author and may be owned by third parties. Such Intellectual Property and Reproductions cannot and must not be made available for use without the prior written permission of the owner(s) of the relevant Intellectual Property and/or Reproductions.

Further information on the conditions under which disclosure, publication and commercialisation of this thesis, the Copyright and any Intellectual Property and/or Reproductions described in it may take place is available in the University IP Policy (see <http://documents.manchester.ac.uk/DocuInfo.aspx?DocID=487>), in any relevant Thesis restriction declarations deposited in the University Library, The University Library's regulations (see <http://www.manchester.ac.uk/library/aboutus/>).

Acknowledgements

There are many people who deserve my thanks for helping me to complete this thesis. Firstly I would like to thank my supervisor Prof. Lucio Piccirillo for his support and guidance throughout this PhD. I would also like to thank the following colleagues at JBCA and JBO: Dr Simon Melhuish for his help in assembling the test equipment used for this work, his general guidance and for his help in using several pieces of software, Eddie Blackhurst for assembling some of the LNAs used in this work, Adrian Galtres for producing the required engineering drawings and Darren Shepard for his skills with a milling machine and never ceasing in his ability to turn a drawing in to a reality.

I would also like to thank my friends: Greg Toby, James, Will and Matthew for their support and for providing plenty of enjoyable distractions over the years. Finally to my family; thanks to my Gran for always providing someone to talk to and lastly and most of all, thanks to my Mum and Dad for their never ending support and for getting me involved in this field in the first place.

Preface

Low Noise Amplifiers (LNAs) have been an integral part of coherent radio receivers for many years, and their continued development has been of crucial importance to radio astronomy for the last few decades. Through enhancing the performance of LNAs radio astronomy has offered astronomers the opportunity to study some of the most fundamental aspects of the universe. For example, “a good” LNA was at the heart of the one of the most significant discoveries of the 20th century, the accidental observation of the Cosmic Microwave Background (CMB) by Arthur Penzias and Robert Wilson in 1964.

Therefore given their value to radio astronomy, the work presented in this thesis was motivated by a desire to enhance the performance of LNAs further, and owing to the author’s involvement in several CMB experiments this was done with a special focus on applying these techniques to the study of the CMB. Chapter 1 will therefore discuss radio astronomy in general, before focusing on the role that LNAs have played in developing our understanding of the CMB, through a chronological review covering CMB theory, observatories and the aims for the future.

Chapter 2 then discusses LNAs themselves, initially outlining the parameters used to describe the LNA. Then given the importance of the transistor to LNAs, Chapter 2 will discuss the transistors themselves including their operation and modeling. The 2nd half of Chapter 2 then reviews the topic of electronic noise theory, how it can be used to describe noise in terms of a noise temperature and the modeling of a transistor’s noise behaviour.

The author’s work in using a variety of techniques to push the noise performance of LNAs towards what is known as the ‘quantum noise limit’ ($N_q \approx hf/k$)¹ will then be outlined. Chapter 3 details the author’s investigations into the relationship between the noise performance of an amplifier and physical temperature. Chapter 4 details a hybridisation of the existing MIC and MMIC approaches to LNA design, creating a new arrangement known as the T+MMIC LNA.

¹where f is the frequency, h is Planck’s constant and k is the Boltzmann constant

Having laid the foundations for enhancing the performance of LNAs, Chapter 5 looks to exploit these ideas by proposing a design for what could, with a predicted average noise temperature of 6.8 K be the lowest noise Ka-band LNA ever reported.

Finally this thesis will conclude by summarising these results and discussing other future developments in LNA technology.

M. A. McCulloch

Manchester, UK

September 2013

Chapter 1

Low Noise Amplifiers (LNA) and Radio Astronomy

One of the most significant components in a coherent radio receiving system is the one that is responsible for the initial amplification of the incoming signal. This is because this component (the LNA) has two roles; firstly it must provide sufficient gain to make the noise contribution of the subsequent components negligible, whilst contributing as little noise as possible to the overall system noise. Secondly, a lower system noise allows astronomers to gain their required sensitivity in a shorter observing time. LNA's come in several forms, however the LNAs most commonly used for radio astronomy are based around Indium Phosphide (InP) high electron mobility transistors (HEMTs). In turn these HEMTs along with other components are either placed discretely within a metallic module or chassis, an arrangement known as the microwave integrated circuit (MIC) or integrated into an individual chip, an arrangement known as a monolithic microwave integrated circuit (MMIC). This chapter will present a discussion on radio astronomy in general and one application of radio astronomy in particular, the study of the Cosmic Microwave Background (CMB).

Band	Frequency	Use
LF	30 - 300 kHz	AM radio, Aviation Navigation Beacons
HF	3 - 30 MHz	Trans-Oceanic Aircraft / Marine Communications, Amateur radio
VHF	30 - 300 MHz	Aircraft Communications, FM radio
UHF	300 - 3000 MHz	Television, Mobile Phones
C	4 - 8 GHz	Wi-Fi, Satellite Communications
X	8 - 12 GHz	Satellite Communications, Radar
K	18 - 26.5 GHz	Radar, Astronomy, Communications
Ka	26.5 - 40 GHz	Radar, Astronomy, Satellite Communications
Q	33 - 50.5 GHz	Radar, Astronomy, Communications
W	75 - 110 GHz	Radar, Astronomy, Satellite Communications

Table 1.1: The Radio Spectrum.

1.1 Radio Astronomy and the Importance of Amplification

1.1.1 The Radio Spectrum

The radio spectrum covers the frequency range below 100 GHz and is heavily used for long distance communications. Over the years this spectrum has been standardised into a series of bands; table 1.1 lists some of the more commonly used frequency bands and those that are of interest to radio astronomy. The radio spectrum is of importance to astronomy because the atmosphere is largely transparent to radio waves.

1.1.2 Radio Receivers

There are two types of receiver available for use in radio astronomy; coherent (figure 1.1a) and incoherent receivers (figure 1.1b). With coherent systems the phase of an incoming signal is preserved, the incoming signal is amplified and the signal is detected, such as by a square law detector. For frequencies above 100 GHz the incoming signal is down-converted to a lower frequency. This is done to facilitate subsequent signal processing,

since lower frequencies are easier and cheaper to manipulate. The down-conversion is performed by a mixer, and amplification is supplied at this intermediate frequency (IF). At lower frequencies, down-conversion may still be used, but in order to increase sensitivity, it takes place after amplification and processing by passive components such as ortho-mode transducers and filters.

Whereas the amplifiers in the coherent system amplify the electric field, bolometers used in the incoherent system detect total power and so such systems do not preserve phase information. Bolometers act like a very sensitive thermometer and consist of an absorber with a certain specific heat capacity, which is connected to a thermal bath. When incident radiation strikes the absorber it heats up and a thermometer detects the temperature rise and converts it into an electrical signal. Bolometer sensitivity is determined by what they are made out of, the integration time and their level of shielding from cosmic rays and radio transmissions [1, 2].

The advantages and disadvantages of the two systems are summarised in table 1.2. For the sensitivities; [3] assumes antimonide based HEMT devices operating at 3 times the quantum noise limit, whilst for the bolometers less sensitive devices are assumed for the ground based case. The HEMT values include a factor of $\sqrt{2}$ since the phase preservation of the coherent systems allows them to simultaneously detect both the Q and U Stokes parameters (see section 1.2.4).

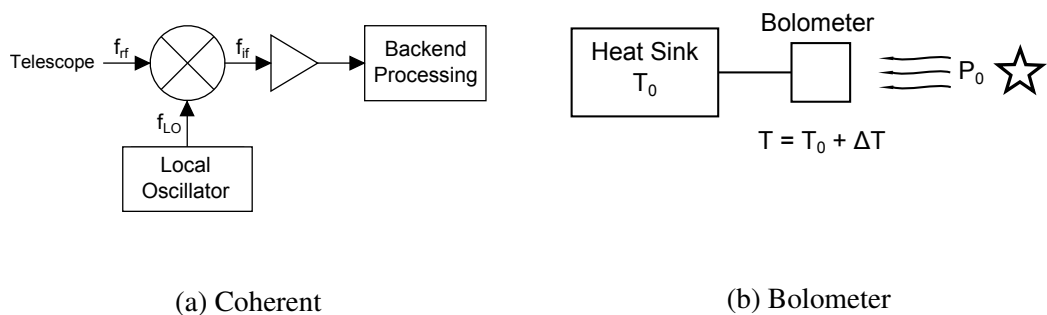


Figure 1.1: (a) shows a coherent receiver system that is configured for down-conversion. (b) a bolometer receiver system.

Parameter	Coherent*	Incoherent
Frequency	< 250 GHz	< 1000 GHz
Bandwidth	Narrow < 30%	Wide (limited by external factors such as intense spectral lines, filters)
Sensitivity (Space)	30 GHz 42 $[\mu K \sqrt{s}]$ 100 GHz 69 $[\mu K \sqrt{s}]$	39 $[\mu K \sqrt{s}]$ 27 $[\mu K \sqrt{s}]$
Sensitivity (Ground)	30 GHz 125 $[\mu K \sqrt{s}]$ 100 GHz 247 $[\mu K \sqrt{s}]$	250 $[\mu K \sqrt{s}]$ 250 $[\mu K \sqrt{s}]$
Minimum Noise Temperature	Limited by the quantum noise limit	Limited by background noise
Operating Temperature	20 K - Room temperature	50 - 300 mK
Phase Preservation	Yes	No

Table 1.2: Summary of the advantages and disadvantages of coherent and incoherent radiometers. The sensitivity values are from [3]. * Coherent system with direct amplification.

1.1.3 Coherent Receivers

The remainder of this thesis will primarily focus on coherent systems and their transistor based LNAs in particular and the remainder of this section will define the relevant terms.

Sensitivity

Due to the weakness of the astronomical signal a good low noise LNA is of particular significance to radio astronomy. This is due to the impact that the LNA has on a receiver's system temperature (see section 2.1 and section 4.2.1). The output of a square law detector is given by (1.1) and it can be shown [4] that the minimum noise level ΔT in Kelvin that can be detected is given by (1.1.2), where B is the bandwidth of the receiver, τ the integration time and T_{sys} the system temperature, which includes the source contribution and contributions from the ground and atmosphere. Therefore for a given integration time

(can be years) the size of the signal that can be detected is determined by the bandwidth of the receiver which is typically limited to $\sim 30\%$ and the system temperature. Observing a weak signal requires either a very long integration time or a low system temperature.

$$P_{out} = kT_{sys}GB \quad (1.1.1)$$

$$\Delta T = \frac{T_{sys}}{\sqrt{B\tau}} \quad (1.1.2)$$

Quantum Noise Limit

The system temperature however can never just be the sum of the source, atmosphere and ground contributions since the receiver temperature can never be zero. This is because the amplifier is subject to the quantum noise limit, the origins of which can be understood by considering the Heisenberg uncertainty principle (1.1.3), where ΔE and Δt are the uncertainty in energy (1.1.4) and time (1.1.5), n is the number of photons, ϕ the phase and f the frequency.

$$\Delta E \Delta T \geq h/4\pi \quad (1.1.3)$$

$$\Delta E = hf \Delta n \quad (1.1.4)$$

$$\Delta T = \Delta \phi / 2\pi f \quad (1.1.5)$$

If the number of photons and the phase possess a Gaussian distribution then (1.1.3) becomes (1.1.6) [4]. For a noiseless amplifier where the power gain (G) is greater than 1, the number of photons at the output n_{out} equals the number of photons at the input n_{in} multiplied by G and the phase (barring a constant phase shift) remains the same ($\phi_{in} = \phi_{out}$). Therefore the output of the ideal amplifier is given by (1.1.7), whilst the input is given by (1.1.8)

$$\Delta \phi \Delta n = 1/2 \quad (1.1.6)$$

$$\Delta\phi_{out}\Delta n_{out} = 1/2 \quad (1.1.7)$$

$$\Delta\phi_{in}\Delta n_{in} = 1/2G \quad (1.1.8)$$

However, this final result (1.1.8) is not consistent with (1.1.6) and this inconsistency can only be resolved if the amplifier is noisy, with the minimum amount of noise per unit bandwidth at the output given by (1.1.9) and at the input by (1.1.10). Letting G become large, results in a minimum noise of hf and the receiver possessing a minimum noise temperature of $\sim hf/k$. Bolometers on the other hand, do not suffer from this limit since they do not preserve the phase of the incoming radiation.

$$(G - 1)hf \quad (1.1.9)$$

$$(1 - (1/G))hf \quad (1.1.10)$$

The quantum noise limit is usually expressed as an approximation. This is because the actual derivation is some what more complex than the simple derivation given here, with the exact role of zero point fluctuations being in debate, hence the quantum noise is sometimes expressed with either a $\ln 2$ or $\ln 3$ in the divisor. The nature of quantum noise is further explored in [5, 6].

1.2 The Cosmic Microwave Background (CMB)

The development of LNAs is unquestionably of strategic importance to all areas of radio astronomy. However, the study of the CMB in particular can benefit from the enhancement of LNAs, since the interesting anisotropy and polarisation signals are very weak and so in order to be detectable on a realistic time scale, the LNAs need to be very low noise. The author has also been involved in two CMB projects and the research outlined in this thesis was carried out with the aim of applying the developments to the study of the

CMB. Therefore the remainder of this thesis will focus on the enhancing the performance of LNAs for future studies of the CMB .

The initial discovery of the CMB was itself in part due to the development of a very good LNA and some of the subsequent CMB observatories and their results have also only been possible due to the development of ever lower noise LNAs. Given this important relationship, this section will present a chronological overview of the theoretical development of modern cosmology, the discovery of the CMB, a brief description of some more recent CMB observatories and a discussion on the current observational aims, chiefly the analysis of the CMB's polarisation signal.

1.2.1 Early Work

The work that would eventually lead to the discovery of the CMB began in 1912 at the Lowell observatory in Arizona where V. M. Silpher was studying the movement of galaxies. Silpher's work would show that most galaxies were moving away from us at high speeds [7].

In 1916 A. Einstein published his general theory of relativity [8] which offered insights² into the dynamics of the universe. One solution proposed by Einstein [9] described a matter filled static universe, whilst a second developed by de Sitter [10] described an empty static universe. The static nature of these universes arose due to Einstein's use of a non zero cosmological constant [11].

However, in 1922, A. Friedman (Friedmann) proposed a third solution [12], which unlike the previous two solutions predicted a time dependent universe. In effect one that would undergo expansion. Lemaitre also came to a similar conclusion and hinted at the possible existence of a 'primeval atom' [13]. Confirmation of this dynamic universe came in 1929 when Hubble showed that the universe was expanding [14]. In 1932 Einstein and

²The theory proposed a series of field equations, the solutions to which described a variety of different universes

de Sitter removed the cosmological constant from Einstein's field equations, leading to solutions that described a flat, expanding universe [15].

This early research would subsequently change our view of the universe, particularly once a way was found to investigate the conditions that had existed in the early universe. This ability would be brought about by measurements of the cosmic microwave background; which was unknowingly detected in 1937 and then discovered by accident in 1964.

In 1937 W. Adams and T. Dunham [16] observed several unknown interstellar lines in the spectra of various stars. In an effort to explain these lines they made observations of the star ζ Ophiuchi, which had previously proved useful in the identification of unknown spectral lines. Additional analysis with the assistance of A. Mckellar [16] showed that one such line, with a wavelength of 3874\AA belonged to the Cyanogen molecule. Further analysis [17] showed that the existence of this line required the 'rotational' temperature of interstellar space to be around 2 K, and it was thought that this temperature was due to inter-particle collisions, even though the necessary collision rate was quite high by the standards of the interstellar medium [18]. This temperature discrepancy would therefore, for the time being remain an anomaly.

In the 1940s G. Gamow began offering theoretical insights into the conditions that had existed in the early universe. In the first [19] of three papers Gamow considered the temperature and density of the early universe and how these conditions related to the relative abundances of chemical elements. In the second [20] Gamow in collaboration with R. A. Alpher and H. Bethe examined the build up of elements during the initial expansion phase. This paper would in time provide the basis for nucleosynthesis. The third paper [21] looked at the cosmological consequences of the previous papers. In this paper Gamow noted that at some point in the past, as the universe cooled it must have undergone a transition from a radiation dominated state to a matter dominated state. Significantly Gamow also noted that the radiation from that earlier stage should, following

this transition continue to propagate out into the now matter dominated universe, cooling as it went. Alpher [22] followed up this idea and found that today the radiation would have a temperature of around 5 K.

By the 1960s the idea of the expanding universe was explained by two competing models: the steady state theory [23] and Wheelers singularity model [24]. In 1964 the latter idea was partially being explored by R. Dicke, P. Peebles, P. Roll and D. Wilkinson at Princeton [25]. Dicke and his colleagues like Gamow were intrigued by the conditions in the early universe and they had begun building a radiometer to search for any radiation that might have originated there.

Simultaneously, A. Penzias and R. Wilson were completing their characterisation of the 20 foot horn antenna at Bell Labs, and to their surprise they found that the antenna was $3.5 \pm 1\text{K}$ hotter than they had expected [26]. They deduced that since this additional temperature was independent of direction and lacked a seasonal variation, it was unlikely to be terrestrial in origin.³

To help solve the mystery, Penzias contacted one of his colleagues B. Burke, who suggested that he should contact Dicke and his colleagues [28]. Dicke [25] proposed that early on in the universe's life the temperature had been very hot, around 10^{10}K creating a fireball. Dicke required this fireball in order to to break down or 'decompose' all of the heavy elements from the previous universe, as at the time it was thought that the universe was created from a previous universe as part of an ongoing cycle. However, Dicke noted that the existence of this fireball was also consistent with the idea of a singularity. Dicke also proposed that the radiation from that fireball would still be propagating through the universe, though expansion would have cooled it to around 3.5 K and that it should possess a black body spectrum.

³The discovery of this anomaly would later be re-told by R. Wilson as part of his Nobel lecture [27].

1.2.2 Penzias and Wilson

This was the radiation was discovered by Penzias and Wilson in 1964 [26]. Penzias and Wilson were able to detect what would become known as the Cosmic Microwave Background Radiation due to their access to two important pieces of equipment. Firstly the Bell Lab's horn antenna; originally it had been designed to detect low noise signals from satellites, so it had excellent ground shielding, the ground contributed a mere 0.5 K to the antenna temperature [27]. Its shape also allowed its noise characteristics to be accurately measured. Secondly, amplification was provided by low noise ruby masers, which were cooled with liquid helium to 4.2 K and had an overall noise temperature of 3.5 K, which was 3 times better than had been possible previously [29]. This cooling allowed Penzias and Wilson to make accurate measurements of the antenna's temperature. They did this by building a switch (figure 1.2) to connect the maser and the detectors to either the antenna or a helium cooled reference load at 5 K. By switching between the two, they were able to use the Y factor method (1.2.1), which will be elaborated on further in section 3.3.6, to measure Y the ratio of the noise produced by the antenna to the noise produced by the reference load. Since the equivalent temperature of the amplifier T_e was known to be 3.5 K and T_2 was the temperature of the reference load, T_1 the antenna temperature could be deduced. They found a temperature of $6.7 \pm 0.3K$ of which only $3.3 \pm 0.7K$ could be accounted for [27].

$$T_e = \frac{T_1 - Y T_2}{Y - 1} \quad (1.2.1)$$

1.2.3 CMB and CMB Anisotropies Observatories

Following Penzias and Wilson's discovery a variety of ground based, balloon based and space based observatories were constructed to observe the CMB. Some of these observatories used coherent detection systems, whilst others have been bolometer based. This is

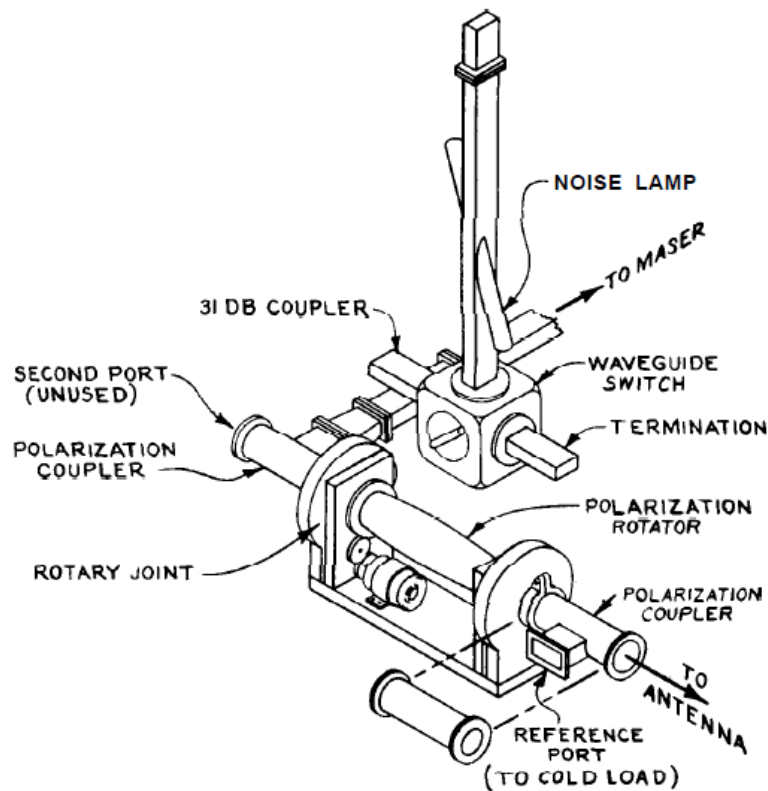


Figure 1.2: Illustration of the radiometer used by Penzias and Wilson. From: Wilson 1978, figure 3 [27].

advantageous as coherent and bolometer systems suffer from different systematic effects, therefore a detection by both approaches would be re-assuring. These effects are further outlined in [30, 3] with Lawrence [3] noting that there are advantageous and disadvantages to both systems; for space based observatories bolometers are more sensitive, but for ground based experiments below 100 GHz the opposite is true, coherent detectors also have preferable systematic issues.

The Cosmic Background Explorer satellite (COBE) was the first satellite dedicated to the study of the CMB. Using the Far Infrared Absolute Spectrometer (FIRAS); COBE could measure the CMB spectrum at sub mm to mm wavelengths to an accuracy of 0.1% relative to a Planck blackbody spectrum [31]. COBE was able to confirm that the CMB possessed a black body spectrum, with the final COBE data set [32] showing an almost

perfect black body spectrum with a peak temperature of $2.728 \pm 0.004K$.

COBE also detected temperature anisotropies (fluctuations) on large angular scales but other more interesting anisotropies were believed to occur on angular scales of less than 1° . These anisotropies however are only $10 - 100\mu K$ in size and so a more sensitive detector was required.

QMAP [33] was a balloon borne experiment that flew twice in 1996 from Texas and New Mexico and aimed to measure temperature anisotropies on angular scales of between $l = 40$ and $l = 140$ using 6 HEMT based amplifiers at 2 frequency bands centred on 31 (2 amplifiers) and 42 GHz (4 amplifiers). The balloon's gondola was subsequently adapted for ground use and turned into the **Mobile Anisotropy Telescope on Cerro Toco (MAP/TOCO)**, which added two SIS mixers at 144 GHz to improve the angular resolution to 0.2° [34]. The adaptation also converted the cooling systems from liquid cryogenics to mechanical cryogenics.

Boomerang was also a balloon borne experiment designed to look for these tiny variations in the temperature. It was expected that their discovery would provide details of the energy density, baryon content and the shape of the early universe [35].

The Boomerang instrument [1, 36], was designed to measure angular scales varying from 0.2° to 4° and was comprised of a 1.3 m telescope with an array of bolometric detectors, which were cooled with liquid Nitrogen and liquid Helium to 300 mK.

Wilkinson Microwave Anisotropy Probe (WMAP) was launched by NASA in 2001, and mapped the entire sky down to an angular resolution of 0.2° . The main goal of WMAP was to measure CMB anisotropies and to produce an angular power spectrum of the CMB. The 5 year data results are shown in figure 1.3.

The angular power spectrum is useful as the size and the position of the peaks provide information about the early universe.

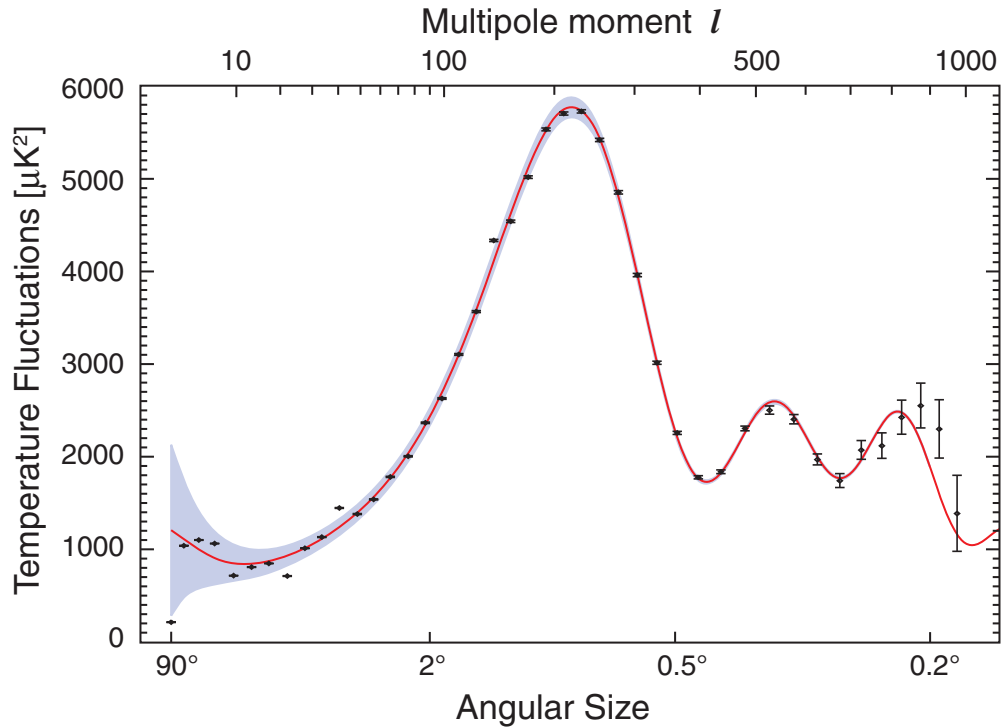


Figure 1.3: CMB angular power spectrum as measured by the WMAP satellite after 5 years of data collection. The Plot also illustrates the relationship between angular size and multi-pole moment. Source: NASA/WMAP Science Team [37].

These temperature anisotropies exist due to quantum mechanical fluctuations in the energy density that arose immediately after the Big Bang. Like any disturbance in a fluid these propagated as a sound wave, with gravity trying to pull the dense regions together, whilst radiation pressure tried to push them apart [38]. As long as radiation pressure provided resistance these waves propagated as a series of compressions and rarefractions [39], but at recombination radiation pressure ceased and as the photons were released the waves were frozen in length. However, photons from overly dense regions were hotter than average whereas those from the under dense regions were cooler, these regions can be seen in WMAP's all sky images 1.4.

The peaks in the power spectrum represent these waves, the first peak corresponds to a wave that was one wavelength long at recombination, whilst the other peaks represent higher harmonics [39]. The position of the first peak at $l \approx 200$ provides details of the

geometry and the overall energy density of the universe [40], whilst the presence of the higher harmonics suggests the presence of an inflationary era in the universe's past [39]. The ratio of the first to 2nd peak can lead to an estimate of the baryon content of the early universe [40]. Finally cosmological models can be fit to the power spectrum and the model's free parameters such as the Hubble constant and the contributions made by dark matter and dark energy to the overall energy density of the universe can be tested [40].

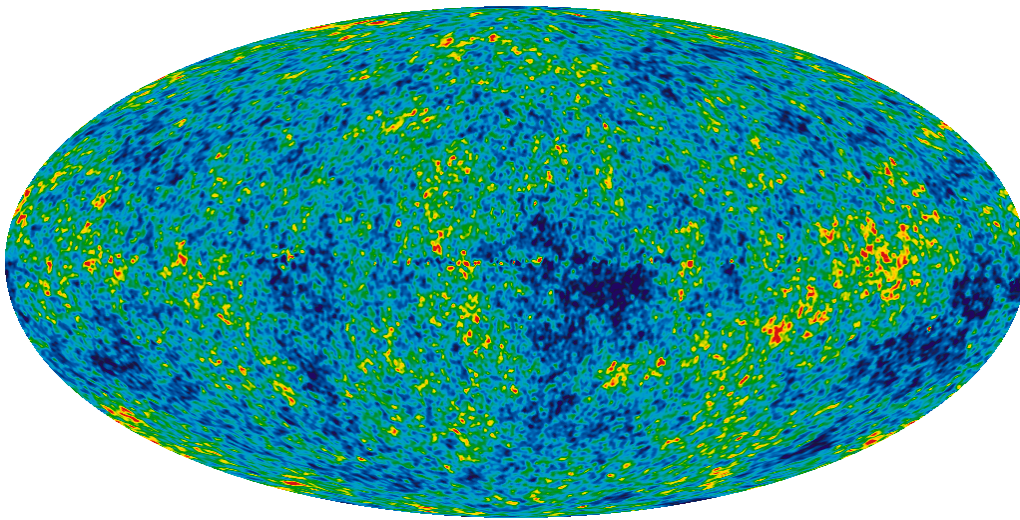


Figure 1.4: The 9 year WMAP all sky map. The temperature range is $\pm 200mK$. Source: NASA/WMAP Science Team [41].

The Very Small Array (VSA) was a ground based Ka-band observatory situated on Mount Teide in Tenerife. VSA was a 14 element interferometer developed from the earlier Cosmic Anisotropy Telescope (CAT) [42] and was designed to measure temperature anisotropies on angular scales of less than 1° . Following an upgrade the array was able to resolve the first 3 acoustic peaks and start to constrain the position and height of the forth [43]. The array used HEMT based amplifiers that were cooled to 20 K and had a tunable bandwidth of 1.5 GHz [44].

The Atacama Cosmology Telescope (ACT) [45, 46] is a recent ground based telescope that was situated in the Atacama Desert in Chile. The telescope looked at the contribution

of the Sunyaev-Zel'dovich (SZ) effect⁴ to the CMB's power spectrum at $l = 300 - 1000$. The telescope observed at three frequencies (148, 218, 277 GHz) using transition edged sensor (TES) bolometers that were cooled to 300 mK by a two stage helium sorption fridge.

Planck is a space based observatory manufactured by the European Space Agency (ESA) that has three times the angular resolution of WMAP and aims to map the angular power spectrum to an even greater accuracy and to measure the E mode polarisation spectrum (CMB polarisation will be discussed later in this chapter) out to $l = 1500$ [38]. This should allow the temperature spectrum and the E mode power spectrum to be compared, which as well as providing constrains on cosmological parameters can also tell us about the universe following recombination such as when the first stars formed [40]. Planck's resolution has also confirmed early hints from WMAP that the standard model is not correct in assuming that the universe is isotropic at large angular scales [47], as there is an observable difference between the northern and southern hemispheres (figure 1.5).

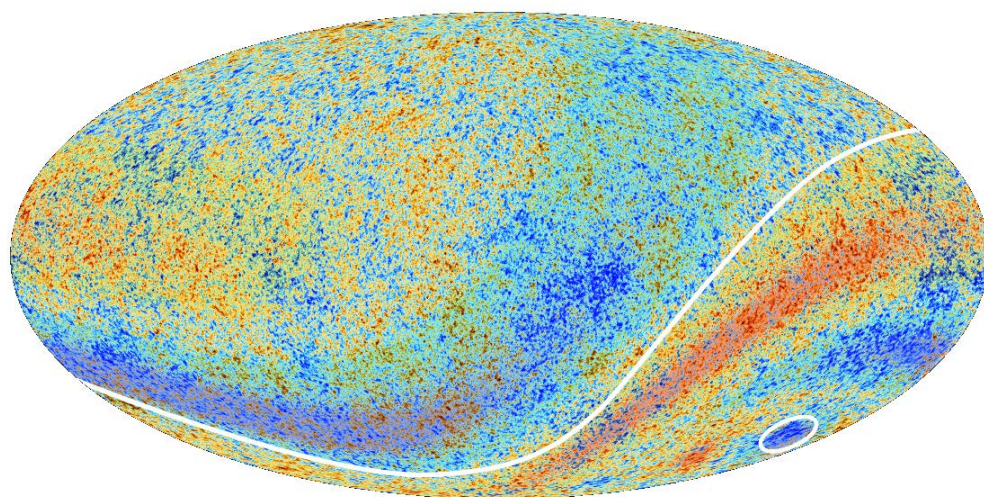


Figure 1.5: The Planck all sky map showing potential temperature anomalies. Copyright: ESA and the Planck Collaboration [48].

⁴The SZ effect is a distortion in the CMB's blackbody spectrum that arises from the inverse Compton scattering of the CMB's photons by high energy electrons in galaxy clusters.

1.2.4 Current Observational Aims

Inflation

Observations of the CMB have proved very useful in developing our current understanding of cosmology and nucleosynthesis. There are, however, still unanswered questions. Many Grand Unified Theories predict the existence of magnetic monopoles and yet they are nowhere to be seen. The universe is also observed to be flat, but big bang cosmology views a flat universe as unstable, since any initial curvature should grow in size [49]. There is also the problem that COBE and WMAP observations indicate that the universe is effectively isothermal, which implies that in the past, different widely spaced regions of sky were in thermodynamic equilibrium with one another. However, these regions are so far apart that light from one region has not yet had time to reach the other, therefore how can they be isothermal? This problem is known as the horizon problem.

The current preferred solution to these problems is inflation. Inflationary models assume that the universe that we can see today (the observable universe) measuring some 45 billion light years in radius [39] started from a sphere of very smooth space that was only 10^{-26} m in diameter [49]. This tiny region of space then underwent a very rapid period of expansion, expanding by a factor of 10^{26} in only 10^{-34} seconds [49]. This exponential expansion resulted in any nearby magnetic monopoles being ‘thrown’, either to the furthest edges of, or even beyond the observable universe. Similarly the rapid expansion deals with any curvature that may have existed in our region of the universe by effectively flattening it out.

Inflation can also explain the horizon problem since it allows different areas of the sky to of been much closer together in the distant past, than they otherwise appear to of been. This is because the rapid expansion associated with the inflationary era would then have moved the different regions apart at speeds well above the speed of light [50].

Inflation also offers an explanation for the universe’s large scale structure. This is

because the quantum mechanical fluctuations that led to the temperature anisotropies were very small in the very early universe; inflation then vastly increased their size, allowing them to act as the basis for universal structure [51]. Therefore as with the CMB's early theoretical work what is needed is a way to probe these inflationary models and one such probe is the CMB's polarisation power spectrum.

Polarisation

The CMB is polarised because of Thomson scattering in the primordial plasma. For most of the plasma's existence the photons were scattered by the electrons but there was no net polarisation, since the radiation field was isotropic (figure 1.6a) [52]. However just prior to recombination there were perturbations in the plasma, which led to velocity gradients causing the electrons to see a quadrupolar field instead (figure 1.6b) [53]. These perturbations had different sources and they lead to different modes of polarisation, these modes are known as E and B (figure 1.7).

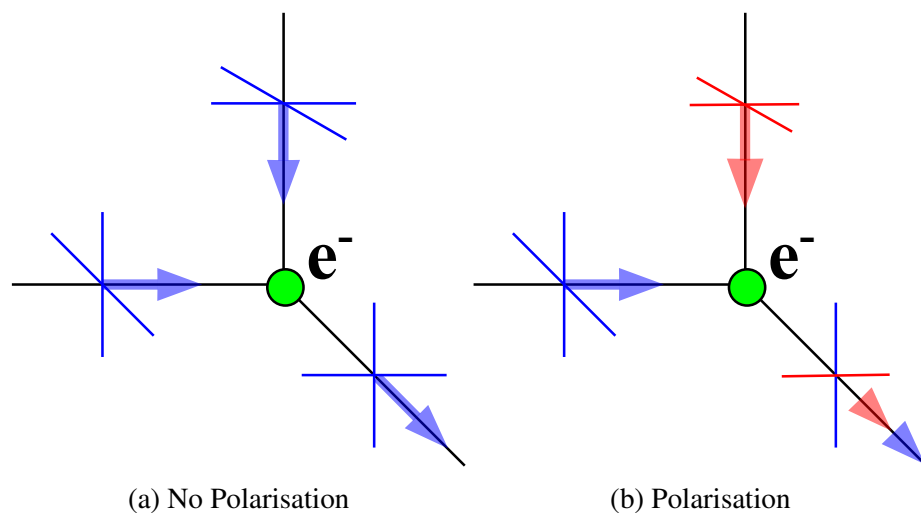


Figure 1.6: The development of a quadrupole radiation field. In (a) the radiation from the left which is incident on the electron (e^-) is identical to from the top. Therefore the polarisations resulting from the scattering with the electron cancel each other out so there is no net polarisation. Whereas in (b) the radiation from the left has a greater intensity than that from the top. This results in a small net polarisation. Source: W. Hu et al (1997), figure 1, [52].

One such perturbation, is variations in the energy density in the primordial plasma. These density perturbations result in polarisation since photons coming out of the over dense and under dense regions had different velocities and so due to the Doppler effect different energies, this created a quadrupole variation in intensity. These density fluctuations are linear in nature and so are known as scalar perturbations [52] and result in the formation of an E mode.

The primordial plasma also underwent tensor perturbations due to fluctuations in the fabric of space resulting from primordial gravity waves passing through the plasma. Unlike the scalar perturbations arising from variations in the energy density these perturbations aren't linear, since the travelling gravity wave induces a vorticity in the plasma resulting in a handedness to the polarization pattern [46]. This pattern is known as a B-mode.

It is also predicted that eddy currents in the plasma just prior to recombination would have given rise to a quadrupole intensity variation. But the size of this polarization signal should be negligible and so can be ignored [54].

Stokes Parameters; measuring the polarisation power spectrum requires measurements to be made of 3 of the 4 Stokes parameters I, Q, and U, which are given along with the forth V by equations 1.2.2 to 1.2.5 [55]. These 4 equations describe the nature of the polarisation via the x and y components (E_x, E_y) of the electric field and their phases (θ_x, θ_y); with I describing the total intensity, Q and U describing the orientation of the x and y components and V is the ellipticity parameter [55]. Though since the CMB is expected to be linearly polarised, V should be zero [56].

$$I = \langle E_x^2 + E_y^2 \rangle \quad (1.2.2)$$

$$Q = \langle E_x^2 - E_y^2 \rangle \quad (1.2.3)$$

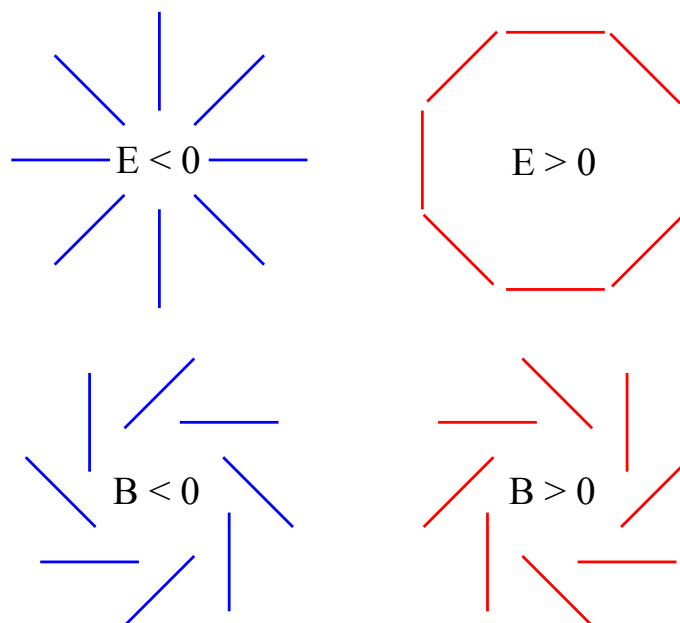


Figure 1.7: E and B mode polarization patterns around hot and cold spots as they appear on the sky. Note E modes have a non-zero divergence and zero curl, whereas the opposite is true for B modes. Source D Baumann (2009), Figure 4, [49].

$$U = 2 \langle E_x E_y \cos(\theta_x - \theta_y) \rangle \quad (1.2.4)$$

$$V = 2 \langle E_x E_y \sin(\theta_x - \theta_y) \rangle \quad (1.2.5)$$

The study of these early perturbations in the plasma is of great significance to cosmologists since it allows them to further constrain the parameters in their models of the early universe. For example, WMAP data suggests that r an important parameter known as the scalar to tensor ratio is greater than 0.02 [57], but if r is found to be smaller than that, then mainstream inflation models would effectively be ruled out [57]. Alternatively if B modes exist then r is greater than zero and this would effectively rule out almost all of the non inflationary models [49]. Because of this, the discovery of primordial B modes⁵ has been described [49, 51, 57] as inflation's ‘smoking gun’, making the detection of B modes of great importance. The detection of B modes is also tantamount to confirming the existence of primordial gravitational waves.

⁵B modes can also result from gravitational lensing.

1.2.5 Polarisation Observatories

Given the obvious usefulness of the E and B mode polarisation signal, several observatories have been constructed to search for and to analyse the E mode signal, which is over an order of magnitude lower than the temperature anisotropy signal [58].

DASI (Degree Angular Scale Interferometer) was the first experiment to observe the CMB's polarisation [59]. To detect it DASI [60] comprised thirteen 20 cm telescopes, which were arranged as an interferometer, with the baselines varying between 25 and 121 cm, allowing DASI to look at angular scales in the region 0.2° and 1.3° ($l \approx 140 - 900$) [61]. To achieve the required sensitivity DASI's amplifiers were based around Indium Phosphide HEMTs [61].

QUAD (Quest at DASI) was a 31 pixel bolometric array with 12 pixels at 100 GHz and 19 pixels at 150 GHz [62]. It aimed to measure the E and B modes and in particular B-modes arising from gravitational lensing⁶. It was the first experiment to detect multiple acoustic peaks in the E-mode spectrum [63].

CBI (Cosmic Background Imager) was a 13x0.9 m diameter interferometer [64] that made measurements of the E-mode polarisation spectrum from 2002 to 2004 [65]. Situated in the Atacama Desert in Chile at over 5000 m, CBI used InP HEMT based MIC amplifiers operating across a frequency band of 26–36 GHz with a minimum noise temperature of 13 K to achieve the required sensitivity.

QUIET I (Q/U Imaging Experiment) [66, 67, 68] was a recent ground based imaging observatory that aimed to measure the E-mode power spectrum and search for the B-mode signal. It was situated at 5080m on the Chajnantor Plateau in Northern Chile, where the

⁶Gravitational lensing can convert E modes into B modes.

atmosphere is very dry and contributes a mere ~ 1 K to the system temperature at Ka-band [64]. Like DASI, QUIET utilised HEMT based LNAs and thanks to its design it was capable of simultaneously measuring the Q and U Stokes parameters. The author was fortunate enough to visit the telescope in 2010 and take part in the observations.

WMAP and Planck have also been used to investigate the CMB's polarisation spectrum. Although designed principally to measure temperature anisotropies WMAP measured the I, Q and U Stokes parameters for the entire sky on angular scales of less than 0.2° across all 5 of its frequency bands⁷ [69]. WMAP detected the CMB's E-mode polarisation and was able to improve our understanding of the foregrounds⁸ that would need to be removed by any future B-mode hunting observatory [70]. Planck also attempted to measure the polarisation spectrum and the results are due to be published shortly.

Efforts are continuing to try and detect the B mode signal but it is at least an order of magnitude smaller than the E mode signal. Therefore if B-modes are to be detected by a coherent detection system, the observatory will require some very good, very low noise LNAs.

⁷The WMAP observing bands were centred on 23, 33, 41, 61, 94 GHz.

⁸Known foregrounds include synchrotron and free-free emission below 40 GHz and dust above 90 GHz.

Chapter 2

Low Noise Amplification and The Problem of Noise

As alluded to in the previous chapter the LNA is one of the most significant components within a radio receiver and lowering the noise temperature of LNAs has been a fundamental goal of LNA development since the early days of radio astronomy. In the case of the transistor based LNAs this goal is limited by the quantum noise limit, with the current lowest noise LNAs possessing a noise temperature approximately 3 times this limit at Ka-band. The first half of this chapter discusses LNAs in detail; the parameters used to describe their performance, the solid state physics that allows them to work, why the field effect transistor makes a good amplifier and why HEMTs like those used in DASI and CBI are the current preferred choice for radio astronomy LNAs. The second half of this chapter discusses the efforts that investigators have gone to to model the HEMT and to describe its noise and gain behaviour.

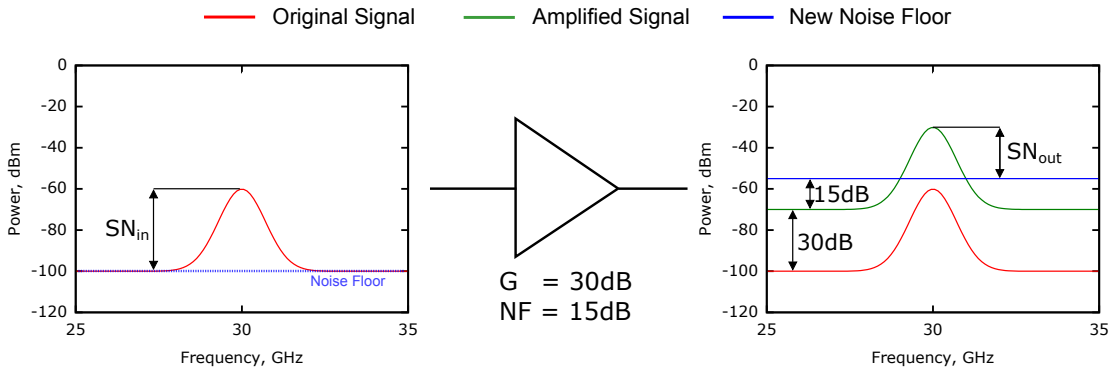


Figure 2.1.1: The noise figure (NF) and gain (G) of an amplifier. SN illustrates the signal to noise ratio.

2.1 Low Noise Amplifiers (LNAs)

2.1.1 Noise Figure and Gain

A low noise amplifier's two most important figures of merit are its gain (how much it amplifies the signal) and its noise figure (how much additional noise its adds to the system). Figure 2.1.1 illustrates how these two characteristics are defined. Both of these terms are typically expressed in decibels (dB)⁹ although noise figure is also expressed as a noise temperature, the two are related by (2.1.1). The amplifier illustrated in figure 2.1.1 possesses a power gain of 30 dB, therefore it amplifies the incoming signal (peak signal strength -60 dBm¹⁰) by 30 dB resulting in a amplified signal with a peak signal strength of -30 dBm. The amplifier also amplifies the noise floor (which in the original case is -100 dBm) by 30 dB and so for an ideal noiseless amplifier the noise floor of the amplified signal would be -70 dBm and the signal to noise ratio at the output (SN_{out}) would equal the signal to noise ratio at the input (SN_{in}). However, the amplifier is not ideal, since it possesses a noise figure (NF) of 15 dB and this noise is added to the noise floor of the amplified signal, resulting in the output signal having a signal to noise ratio of 25 dB. Thus the noise figure is defined as the degradation in the signal (S) to noise (N) ratio (2.1.2).

⁹The decibel is a logarithmic unit that expresses the ratio of two powers.

¹⁰Power (dBm) = $10\log_{10}(\text{Power(W)} / 1 \text{ mW})$, i.e. 1 mW = 0 dBm.

$$T_n(K) = 290 \times (10^{NF/10} - 1) \quad (2.1.1)$$

$$NF = \frac{SN_{in}}{SN_{out}} = \frac{S_{in}/N_{in}}{S_{out}/N_{out}} = \frac{-60/-100}{-30/-55} = 15dB \quad (2.1.2)$$

2.1.2 S Parameters

Another important way of characterising an amplifier, or any microwave component in fact is to make use of the component's S or scattering parameters, which are given for a 2 port device (figure 2.1.2) by (2.1.3), where V_n^- is the amplitude of the voltage wave emerging from port n and V_m^+ is the amplitude of the voltage wave into port m . S parameters can also be described in terms of a power wave.



Figure 2.1.2: A basic 2 port network.

$$\begin{bmatrix} V_1^- \\ V_2^- \end{bmatrix} = \begin{bmatrix} S_{1,1} & S_{2,1} \\ S_{1,2} & S_{2,2} \end{bmatrix} \begin{bmatrix} V_1^+ \\ V_2^+ \end{bmatrix} \quad (2.1.3)$$

The value of an individual element can be determined from (2.1.4)

$$S_{n,m} = \frac{V_n^-}{V_m^+} \Big|_{V_k^+ = 0 \text{ for } k \neq m} \quad (2.1.4)$$

For example, $S_{1,1}$ is calculated by terminating port 2 with a matched load (a matched load prevents reflections) and measuring the ratio of the amplitudes of the voltage waves into and out of port 1. Thus because port 2 is terminated, S_{11} is actually the reflection coefficient seen looking into port 1, likewise $S_{2,1}$ would be the transmission co-efficient

for a signal passing from port 1 to port 2. Hence, the S parameters can be used to provide a measure of the amplifier's return loss and its insertion loss (gain).

Return Loss ($S_{1,1}$)

The return loss ($b1/a1$) is a measure of how much of the input signal is reflected back out of the amplifier, thus it is equivalent to $S_{1,1}$ and it is given in terms of decibels¹¹ by (2.1.5), where P_{in} is the power into port 1 and P_{ref} is the power reflected by port 1. A good value for an LNA is less than -10 dB.

$$RL(\text{dB}) = 10 \log_{10} \frac{P_{in}}{P_{ref}} = -20 \log_{10} |S_{1,1}| \quad (2.1.5)$$

Insertion Loss ($S_{2,1}$)

The insertion loss ($b2/a1$) is a measure of how much of the signal is lost as it is transmitted through the component, obviously in the case of amplifiers this loss is actually a gain and it is equivalent to $S_{2,1}$ and it is given by (2.1.6) where P_{rec} is the power received at port 2. A typical value for an LNA is $\sim 25 - 40$ dB.

$$IL(\text{dB}) = 10 \log_{10} \frac{P_{in}}{P_{rec}} = -20 \log_{10} |S_{2,1}| \quad (2.1.6)$$

The remaining 2-port S parameters are known as the output return loss ($S_{2,2}$) and the reverse gain ($S_{1,2}$). With the important parameters defined, the remainder of this chapter will focus on the characteristics of the transistors that are used in LNAs, starting with the theory of semi-conductors.

¹¹The difference in the multiplication factors (10 and 20) depending on whether you take the ratio of the power or the voltage arises because power is proportional to the square of the voltage.

2.2 Semi-conductors

Materials can depending on the nature of their electrical conductivity be divided up into 3 categories: conductors, insulators and semi-conductors. Conductors such as gold and copper have a low electrical resistance and conduct electricity with relative ease, insulators such as poly-tetra-fluro-ethylene (PTFE) and air have very high resistances and under most circumstances will not conduct electricity. Semi-conductors however, can depending on their exposure to external stimuli be either conductors or insulators and this transition can be explained by considering their band structure.

2.2.1 Band Theory

The positions of electrons within a substance can be described by a band structure (figure 2.2.1), and the bands within this structure can be divided up into two types.

The Conduction bands hold electrons that are free to move between parent atoms. For metals these bands are populated by numerous electrons, whereas for insulators these bands are rarely populated. For semi-conductors, this band can be become populated given the right conditions.

The Valence bands hold electrons that are (for most energies) permanently bonded to the parent atoms, however should an electron be promoted to a conduction band, the resulting hole in the valence band now allows the electrons in the valence band to move.

The ease of movement of electrons between these bands is what gives rise to the electrical properties of a substance. For example metals (figure 2.2.1.a) have a high conductivity as the conduction and valence bands overlap, consequently a large number of electrons are free to move around within the metal. This is in stark contrast to the behaviour of the electrons within an insulator (figure 2.2.1.c), where there is a large energy gap between the valence and conduction bands, consequently with the exception of cer-

tain extreme conditions the conduction bands are empty and the conductivity is very low. Semi-conductors (figure 2.2.1.b) on the other hand have a sufficiently small band gap that it is possible for electrons from the valence band to access the conduction band and permit conduction. When this occurs an oppositely charged hole forms in the valence band, which is also free to move.

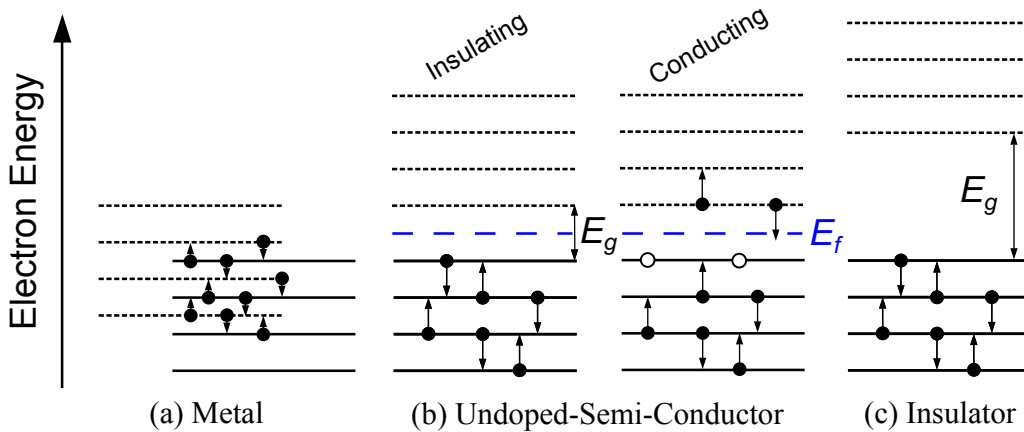


Figure 2.2.1: The band structure of metals, semi-conductors and insulators. E_g is the band gap energy, E_f is the Fermi energy. The valence bands are represented by solid lines, whilst dashed lines represent the conduction bands. Electrons are represented by solid circles, whilst holes are represented by open circles. Developed from D. L Pulfrey et al, figure 2.13 [71].

Figure 2.2.1 also illustrates two other important terms:

The Fermi level E_f is the energy level for which the probability of finding an electron within a material in thermodynamic equilibrium is exactly 0.5. Put more simply, it is the highest energy level occupied by electrons at 0 K with all lower levels filled.

The Band Gap E_g is the term used to describe the difference in energy between the valence bands and the conduction bands. For metals the band gap is effectively zero and the valence and conduction bands simply blend into one another. Whereas for insulators the band gap is sufficiently large that it is greater than the energy required to liberate an electron. For semi-conductors however, E_g is a very important parameter as it dictates the energy at which a semi-conductor switches from an insulator to a conductor. The

transition is generally very abrupt and can be triggered by raising the temperature or by applying an electric field

2.2.2 Doping

From figure (figure 2.2.1.b) it is obvious that for a pure material the concentration of electrons (n_i) in the conduction band must equal the concentration of holes (p_i) in the valence bands. However, this relationship can be disturbed by the addition of impurities which can donate or accept electrons from the atoms within the bulk material. To be an effective dopant an impurity must be able to substitute itself for a semiconductor atom at a lattice site [71]. Therefore it should have a similar atomic mass to the semiconductor atom that it is substituting. For example in the case of Indium Phosphide, Aluminium (mass number ~ 27) is a good substitute for the Phosphorus (~ 31), whilst Antimony (~ 122) is a good substitute for Indium (~ 115). The effect of doping on several semi-conductor properties can be seen in table 2.1.

A dopant which donates electrons is known as an n-type, whilst a dopant that accepts electrons is known as a p-type. The nature of the dopant is dependent on the number of electrons left over once the dopant atom has substituted itself into the semiconductor's lattice. For example Silicon being a group IV element has 4 valence electrons available for bonding, therefore it bonds to 4 other silicon atoms. However, if one of those silicon atoms is substituted for a phosphorus atom (group V), 4 of its valence electrons will be used to bond with the 4 surrounding silicon atoms. The 5th however is only loosely bonded to the phosphorus atom and it will only take a small amount of energy to raise it into a conduction band and for the phosphorus atom to become a positively charged ion. This is an example of n-type doping. At microwave frequencies only n-type doping is used, as the mobility of electrons is considerably higher than the mobility of holes [71]

In terms of the Fermi energy; the more n-type a material, the closer the Fermi level is to the conduction bands, whilst the more p-type a material, the closer the Fermi level is to

the valence bands.

2.2.3 Electron Mobility

Different semi-conductors possess different electron mobilities. Table 2.1 shows the electron mobility for several semi-conductors. The electron mobility is important in terms of LNAs because it has a role in determining the noise performance of the LNA, with a higher mobility being associated with lower noise due to less coulomb scattering [72]. Improved mobility also offers higher device speeds [73]. Electron mobility σ can be determined from (2.2.1), where E is the electric field in V/cm and v_d is the electron drift velocity in cm/s .

$$\sigma = \frac{E}{v_d} \quad (2.2.1)$$

Semiconductor	Band Gap (eV)	ϵ_r	Lattice Constant (\AA)	Electron Mobility (cm^2/Vs)
Ge	0.66	16.0	5.66	3900
Si	1.12	11.8	5.43	1500
GaAs	1.43	10.9	5.65	8500
InP	1.29	14.0	5.87	1600
InAs	0.33	14.5	6.06	33000
InSb	0.16	17.0	6.48	78000
Ga _{0.15} In _{0.85} As	1.2	-	5.85	9500
Ga _{0.47} In _{0.53} As	0.75	-	5.85	15000

Table 2.1: The properties of some semi-conductors at 300 K. Data sourced from [74].

2.3 The Field Effect Transistor

There are several different types of transistor that may be found in amplifiers, such as bipolar-junction-transistors (BJT), metal-oxide-semiconductor-field-effect-transistors (MOS-

FET), metal-semiconductor-field-effect-transistor (MESFET). However, the transistor of most interest to the LNAs that are commonly used for radio astronomy is the High Electron Mobility Transistor (HEMT), which is a development of the Field Effect Transistor (FET).

2.3.1 Development

The FET was first proposed back in 1938, the basic field theory was developed by Shockley in 1952 and shortly after the first one was fabricated on Silicon [75]. However, the higher electron mobility of GaAs offered the possibility for lower noise and higher speed and the first GaAs FETs were subsequently developed in the 1960's [76].

2.3.2 Heterostructure

In its simplest form the FET is comprised of several layers of semi-conductor, on top of which are a series of metal contacts, which provide connectivity to the rest of the circuit. A schematic of a basic GaAs FET is shown in figure 2.3.1.

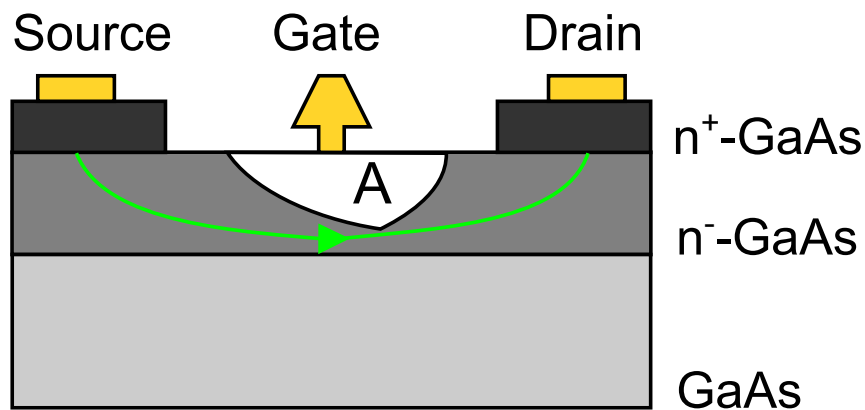


Figure 2.3.1: The structure of a GaAs based FET . The region below the gate (A) is known as the depletion region. The depletion is slightly asymmetric due to the source drain voltage.

Figure 2.3.1 shows that the FET can be divided up into several distinct regions; the ohmic contacts comprising the drain and source pads and their respective heavily doped

regions of GaAs, a lightly doped region of GaAs where the current flows, a semi insulating region of un-doped GaAs, the gate contact and a depletion region.

The Gate Contact

The gate contact is used to control the HEMT device. It is a metallic contact, which sits directly on top of the lightly doped (n^-) GaAs region. However, due to gold's tendency to diffuse into the semi-conductor, a thin (~ 5 nm) layer of titanium or platinum is placed between the gold and the GaAs. Since the metal is placed directly on top of the lightly doped semiconductor; conduction electrons in the semi-conductor can drift towards the gold resulting in the formation of a Schottky Barrier and a depletion region in the semiconductor within the vicinity of the gate.

The Depletion Region

Figure 2.3.2a shows the band diagram for a metal and a doped semi-conductor; when they are far apart the Fermi energy levels are different and the bands are flat. However, if the Fermi level in the semiconductor is higher than that of the metal, (i.e. (2.3.1) holds true, where Φ_m is the metal's work function¹² and $q\chi$ is the electron affinity¹³) and the metal and semi-conductor are brought together, electrons will flow across the interface into the metal in an effort to equalise out the Fermi levels. This results in the region below the gate being devoid of electrons (**depletion region**) resulting in the region possessing a slight positive charge (figure 2.3.2b). As the electrons drift across the junction the positive charge increases and exerts a force (red arrow F_+) that resists further flow of electrons across the interface leading to an equilibrium condition.

$$\chi + V_{cf} < \Phi_m \quad (2.3.1)$$

¹²the energy required to liberate an electron

¹³the energy required to liberate an electron from the lowest conduction band

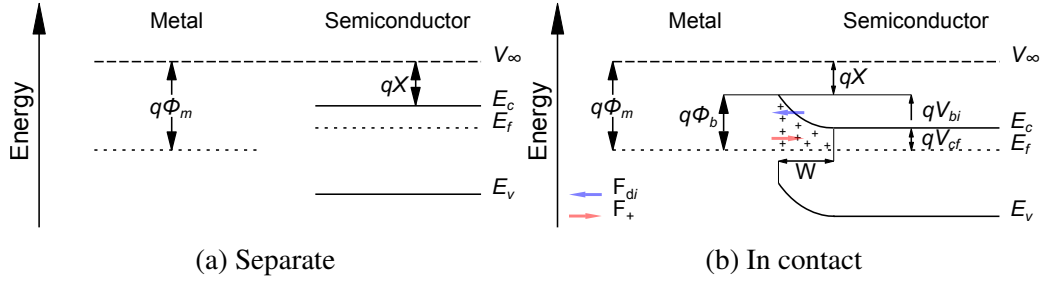


Figure 2.3.2: Band diagrams illustrating the formation of the depletion region.

This equilibrium condition can also be seen by considering the barrier potentials. Figure 2.3.2 also shows that the bands in the semiconductor bend as they near the junction; this is due to the forces that cause the electrons to flow across the border. The degree of band bending is given by the built in potential (V_{bi}) (2.3.2), which must be overcome by an electron before it can cross the junction. Similarly electrons in the metal must overcome the Schottky barrier Φ_b (2.3.3) before they can flow across the junction back into the semiconductor.

$$V_{bi} = \Phi_m - \chi - V_{cf} \quad (2.3.2)$$

$$\Phi_b = \Phi_m - \chi \quad (2.3.3)$$

The size of (V_{bi}) and Φ_b is also significant when the gate contact has an external potential (bias) applied to it. Should the gate contact be positively biased, F_{di} is increased resulting in an increased flow of electrons into the gate contact, this arrangement is known as forward bias. The effect of the positive potential on the band shape is to reduce the level of bending resulting in a lower V_{bi} thus lowering the energy required by electrons to flow across the junction, though Φ_m remains unchanged. Should a negative bias be applied the opposite is true, this arrangement is known as reverse bias.

The width (W) of the depletion region is given by (2.3.4) [77], where V is the applied voltage, k is the Boltzmann Constant, T is the physical temperature, N_d is the donor doping concentration. (2.3.4) shows how varying the bias can alter the width of the depletion

region.

$$W = \sqrt{\frac{2\epsilon_r \epsilon_0}{qN_d} \left(V_{bi} - V - \frac{kT}{q} \right)} \quad (2.3.4)$$

The Ohmic (Drain and Source) Contacts

The ohmic contacts consist of two regions, a metal contact pad and a heavily doped region of semi conductor. The pads are typically made of gold since this has a very low resistance, does not rectify any input signal and has a linear current resistance relationship (hence ohmic). The heavily n-doped GaAs layer is required to prevent the formation of a Schottky barrier. However, one still forms but the depletion region is sufficiently thin ($\sim 1-3$ nm) that the electrons are able to tunnel through the region, resulting in a very low resistance contact.

Lightly Doped and the Semi-Insulating Region

The lightly doped region is the source of the channel electrons, whilst the semi-insulating region separates the active channel from the ground plane on the base of the transistor. This layer helps reduce the size of the parasitic capacitance between the contacts and the ground plane leading to faster devices [78].

2.3.3 The FET as an Amplifier

Achieving Gain

The FET is controlled by varying the voltage applied to the gate, this in turn varies the size of the depletion region below the gate (2.3.4). This variation subsequently alters the flow of charge carriers between the source and the drain. This is the key to making the FET an effective amplifier. If an input bias and an output circuit are connected to the drain, as shown in figure 2.3.3, then modulating the voltage on the gate will modulate the

drain source current which will result in a modulation in the output, thus if the circuit is correctly set up, the transistor will amplify any signal attached to the gate. This property is known as the transconductance (2.3.5) and can be seen graphically in figure 2.3.4. Figure 2.3.4 shows the DC $V_g I_d$ characteristics (these were measured using a probe station¹⁴) for a Hughes Laboratories InP HEMT. In the case of this transistor, a gate voltage variation of ± 0.05 V will result in a ~ 5.9 mA change in the drain current.

$$g_m = \frac{\Delta I_{ds}}{\Delta V_{gs}} \quad (2.3.5)$$

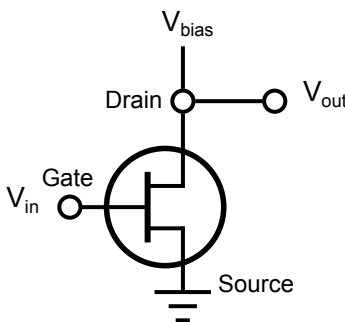


Figure 2.3.3: The FET as an amplifier .

¹⁴An instrument capable of subjecting an individual device to both RF and DC signals in order to measure its performance.

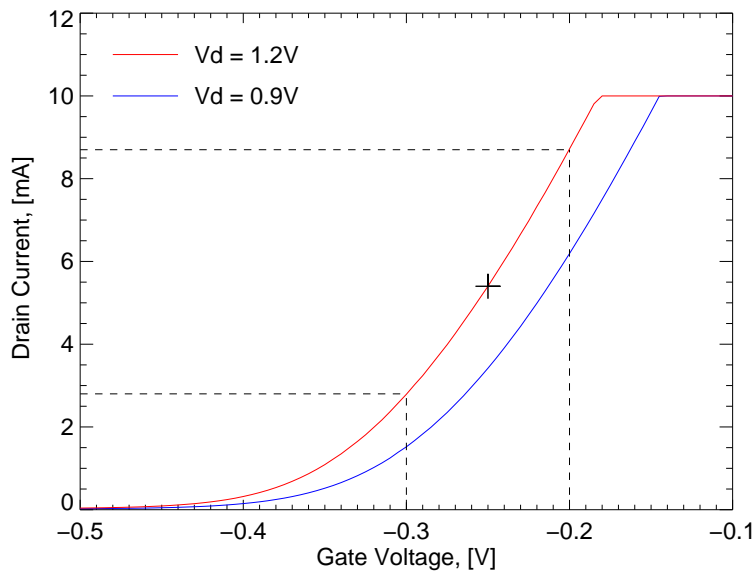


Figure 2.3.4: Measured I_d (drain current) V_g (gate voltage) characteristics for a HRL Laboratories $4 \times 25 \mu\text{m}$ HEMT, illustrating why FETs make good amplifiers. Data taken with the assistance of Mr K. Williams, School of Electrical and Electron Engineering.

2.4 High Electron Mobility Transistors (HEMTs)

Whilst FETs make very good amplifiers, an inherent weakness in the FET design is that the electron channel also contains the donor atoms themselves. This leads to considerable coulomb scattering between the electrons and their donor ions. This effect restricts the overall electron mobility and is a considerable contributor to the FET's noise figure. However, by adjusting the heterostructure (the layers of semi-conductor) it is possible to separate the electrons from their donor atoms, thus reducing the level of impurity scattering. This type of transistor is known as a HEMT and was developed in 1980 by T. Mimura et al [79]. HEMTs represent a considerable improvement over the FET since they increase the electron mobility by trapping the conduction electrons within a two dimensional region. This increase in electron mobility for a HEMT over a conventional FET can be seen in table 2.2.

The removal of impurity scattering becomes even more significant when the HEMT is cooled. Table 2.2 shows the increase in the electron mobility that occurs when the HEMT

2.4. HIGH ELECTRON MOBILITY TRANSISTORS (HEMTS)

	MESFET	HEMT
Electron Mobility at 300 K (cm^2/Vs)	4000	8500
Electron Mobility at 77 K (cm^2/Vs)	6000	80000

Table 2.2: Electron mobility for a conventional GaAs MESFET and HEMT structure at 300 and 77 K [74].

is cooled to 77 K. This rise can be understood by considering the nature of the scattering that takes place within the semiconductor layers. The variation in mobility with respect to temperature for a FET and a HEMT can be seen in figure 2.4.1. Figure 2.4.1 shows that at some temperature impurity scattering prevents any further increase in mobility and the mobility of the electrons decreases. The HEMT overcomes this problem by separating the electrons from their donors (the source of the impurity scattering). This results in virtually no impurity scattering allowing a dramatic increase in electron mobility with lowering temperature.

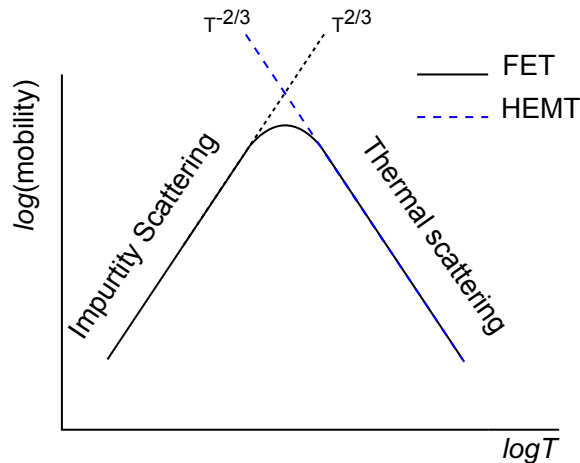


Figure 2.4.1: The relationship between electron mobility and temperature for a FET and a HEMT. Note the HEMT's mobility does not increase indefinitely with decreasing temperature.

2.4.1 Basic Structure

The HEMT structure differs from the one seen for the FET in figure 2.3.1, by the addition of two layers of semi conductor. For a typical HEMT one would be an n-doped Al-GaAs layer and the other would be a very thin un-doped layer of Al-GaAs. These additional layers, which can be seen in figure 2.4.2, adjust the position of the transfer current, moving it into the un-doped InGaAs region.

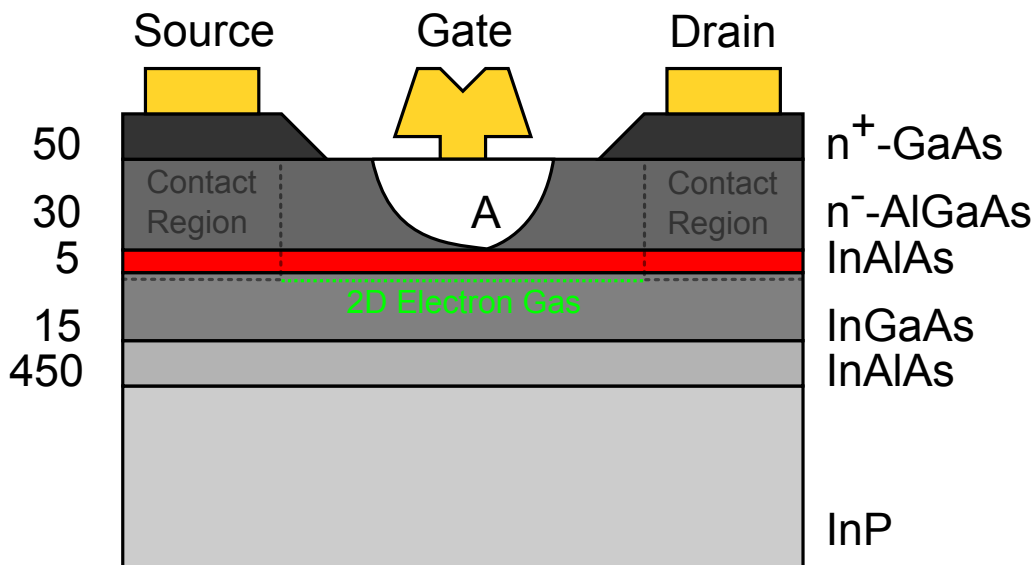


Figure 2.4.2: The structure of a basic InP HEMT structure (not to scale), the semiconductor layers are listed on the right, whilst a typical thickness (in nm) for each of the layers is shown on the left.

The n^- AlGaAs layer performs two roles; it is within this layer that the depletion region that controls the HEMT exists, secondly this layer provides the electrons for the transmission of the signal within the GaAs layer.

Un-doped InAlAs spacer is a very thin layer ($\sim 50\text{\AA}$), which is designed to increase the electron mobility. It does this by increasing the separation distance of the electrons from their donor ions. Work by Pospieszalski [80] showed that at 77 K a spacer layer can increase the electron mobility from $19900\text{cm}^2/Vs$ to $99500\text{cm}^2/Vs$ and at cryogenic

temperatures the spacer layer reduces the noise temperature by a factor of 3 and increases the operating bandwidth.

The InGaAs layer is an un-doped layer of InGaAs and it is within this layer that the transfer current flows between the drain and source terminals. It is also within this layer that the interesting device physics takes place as the conduction electrons are confined to a 2 dimensional layer and so behave as a 2 dimensional electron gas (2-DEG).

The InAlAs layer aids lattice matching between the InGaAs and the InP.

InP based HEMTs offer lower noise and higher operating speeds than earlier GaAs devices and this is due to the higher electron mobility of InP based devices. However, table 2.1 showed that the electron mobility of GaAs is greater than that of InP, thus the increased mobility actually arises from one of the other semiconductors that make up the device, for example $\text{Ga}_{0.47}\text{In}_{0.53}\text{As}$. $\text{Ga}_{0.47}\text{In}_{0.53}\text{As}$ however cannot be used with GaAs as the presence of the indium distorts the crystal lattice resulting in poor electrical performance, therefore InP is used as the substrate instead as it has a 'good' lattice match with the InGaAs. As in the FET, the InP layer also insulates the active region from the transistor's ground plane.

2.4.2 Band Bending and the 2-DEG

Unlike the FET, the HEMT is made up of differing layers of semi-conductor. However, as in the FET the Fermi level must still be continuous across the interface that exists between the two semi-conductors. This interface is known as a hetero-junction and a 2-DEG will form below this hetero-junction if the doped semi conductor possesses a larger band gap than the un-doped semi conductor [81, 82].

If this is the case, when the semi-conductors are brought together, the donor electrons in the doped semi-conductor will migrate into the un-doped semi-conductor. This mi-

gration has several consequences; firstly the Fermi energy is equalised throughout both semi-conductors and secondly a large electric field (around $10^5 Vcm^{-1}$ [83]) is generated at the interface. This field alters the shape of the conduction band and results in the formation of a discontinuity E_{dc} . E_{dc} is equal to the difference in the electron affinities of the two semi-conductors and for most semi-conductors this discontinuity is greater than the thermal energy of the electrons at room temperature [84]. This results in the donor electrons becoming trapped on the un-doped side of the interface.

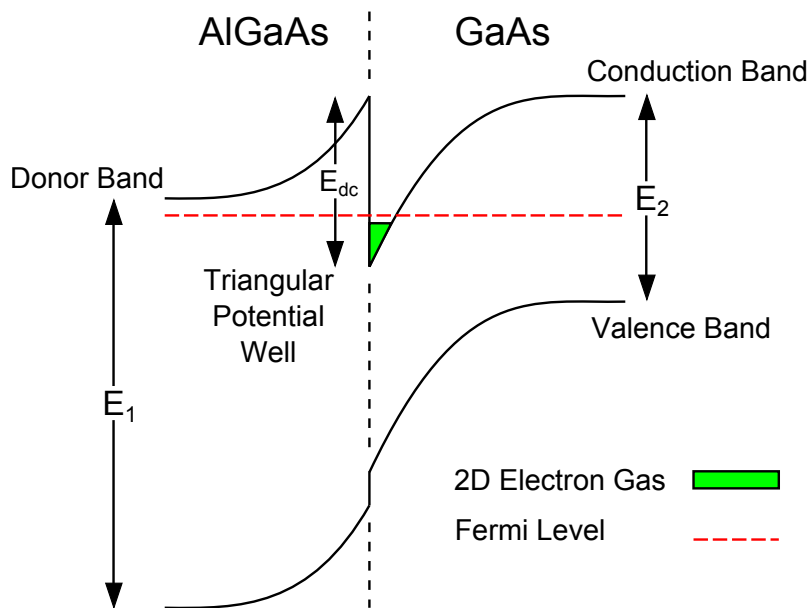


Figure 2.4.3: Conduction and valence band characteristics at the hetero-junction between 2 semi-conductors.

As can be seen from figure 2.4.3 the potential well that forms on the un-doped side of the interface is roughly triangular in shape and as it is only around 100\AA deep, the quantum mechanics behind the formation of the 2-DEG is outlined further in [84, 85]. The depth of the potential well can be varied by changing the gate voltage. For a depletion mode device¹⁵, making the gate more negative reduces the depth of the potential well, which in turn lowers the electron density in the 2-DEG gas resulting in a reduction in the current flowing between the source and the drain. Thus like a FET the current flowing through

¹⁵Depletion mode: the transistor is on for $V_{gs} = 0$.

the device can be controlled by varying the gate voltage. However, whereas in the FET, the gate varied the resistance of the channel by altering the depth of the depletion region, the HEMT works by controlling the density of electrons within the channel. In the case of enhancement mode devices¹⁶, there will be no current flow without a forward gate bias.

2.4.3 The T-gate

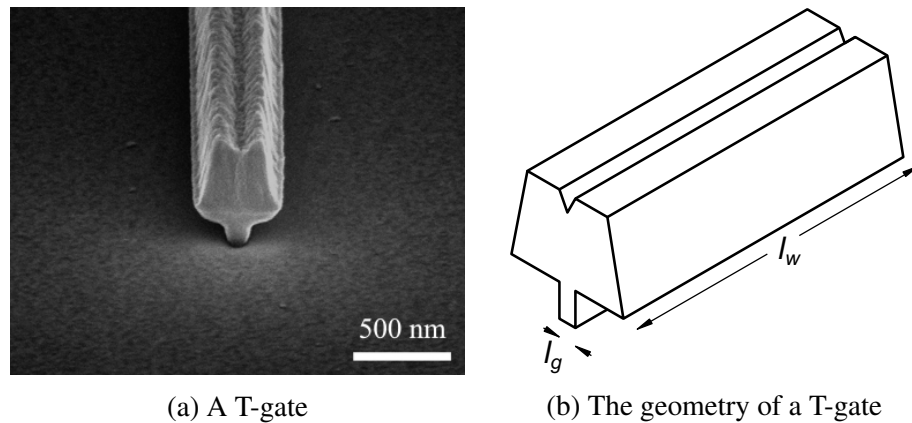


Figure 2.4.4: (a) shows an actual image of a T-gate taken by an SEM at an oblique angle [86]. (b) shows the geometry of a T-gate.

The HEMT's gate contact is mushroom or T-shaped since the T-section (figure 2.4.4a) provides the structure with sufficient cross sectional area to carry the required current, without increasing the gate capacitance as much as a big flat gate would. The transistor's gate geometry is described by two dimensions which can be seen in figure 2.4.4b, the gate length l_g which paradoxically is the size of the T's footprint on the semi-conductor, whilst l_w the gate width is the length of the gate from its tip to its pad (the gate finger). Typically l_g is $< 250\text{nm}$ whilst l_w is $< 50\mu\text{m}$, however it is the gate length that is most significant in terms of the noise temperature, with small gate lengths generally offering the lowest noise temperatures and higher operating frequencies. The current state of the art T-gates have gate lengths of $\sim 20\text{ nm}$ [87] whilst transistors with gate lengths of 35 nm have been

¹⁶Enhancement mode: the transistor is off for $V_{gs} = 0$.

successfully integrated into LNAs [88]. The small ‘divot’ in the top of the t-gate is a by-product of the fabrication process.

Images of a Transistor

As the dimensions of a HEMT’s metallic contacts typically measure in the 10s of nm to a few microns, it is necessary to view the metallic structure under a microscope or preferably a scanning electron microscope (SEM). Figure 2.4.5 shows a collection of SEM images taken of the Hughes Laboratories $4 \times 25 \mu m$ HEMT. The images illustrate the small scale of the structures that make up a modern transistor. Figure 2.4.5a shows the $4 \times 25 \mu m$ long gate fingers, the 2 drain fingers and the large source pads. Figure 2.4.5b shows a close up of the gate finger. Figures 2.4.5c and 2.4.5d illustrate the use of an air bridge to connect the source fingers together.

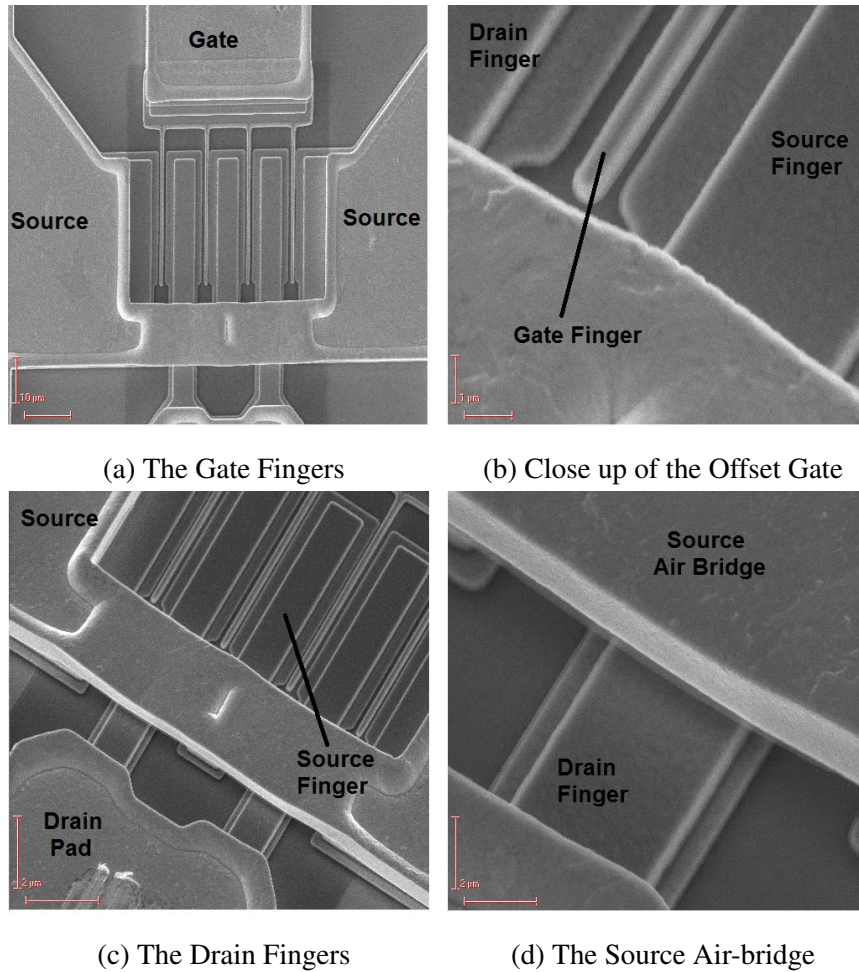


Figure 2.4.5: SEM images of a Hughes $4 \times 25 \mu\text{m}$, gate length = 100nm HEMT. Images taken with the assistance of Dr S. Lewis.

2.5 The Equivalent Circuit

In order to design an effective LNA, it is necessary to simulate the interactions that take place between the various components and the transistors. This requires a way of simulating the behaviour of the transistor, which is achieved through the use of a device model. There are a variety of such models available, however the one that is most relevant to the LNAs used for radio astronomy is the small signal equivalent circuit model. This model uses a series of ideal components (resistors, capacitors, inductors) and a transconductance to model the performance of a transistor. This model also allows the physics of the transistor itself to be investigated, which also makes this model useful for device

development.

A typical equivalent circuit is shown in figure 2.5.1 and a 3D schematic of a HEMT showing the idealised physical locations of these components can be seen in figure 2.5.2.

2.5.1 The Parameters

The Inductances

L_g, L_d, L_s represent the inductance that arises in the gate, drain and source pads respectively. An interesting feature of the inductance components is that there is very little variation between devices due to the pads on different devices all being a similar size [78]. It should also be noted that in addition to these inductances there also exists an inductance caused by the attaching bond wire (section 4.3.3), which typically dominates the device inductance.

The Resistances

R_g, R_d, R_s represent the resistance of the gate, drain and source pads, including in the case of R_d and R_s the resistance of the heavily doped ohmic contact and any resistance arising in the semi-conductor between the contact and the active channel. R_{gs} also expressed as R_i is a frequency independent resistance, known as the charging resistance. It is of questionable physical significance and is included to improve the match to $S_{1,1}$ [78].

R_{ds} which is often expressed as a conductance (g_{ds}) (2.5.1) represents the resistance of the conduction channel. [89, 90, 85]. These resistances are particularly significant at low frequencies [85].

$$g_{ds} = \frac{\delta I_{ds}}{\delta V_{ds}} \quad (2.5.1)$$

The Capacitances

C_{pg}, C_{pd} represent the capacitance generated by the gate and drain contact pads, C_{gd} and C_{gs} model the capacitance caused by changes in the charge of the depletion region with respect to the gate-drain and gate-source voltages. C_{ds} is required in order to model capacitance effects that arise between the source and drain pads.

Transconductance and Delay

The two remaining parameters g_m and τ represent the transconductance and response time of the device. The transconductance represents the FET's intrinsic gain function and is a measure of the incremental change in the devices output current I_{ds} with respect to an incremental change in the input voltage V_{gs} (2.3.5).

The response time represents the delay that exists between a given fluctuation in the gate voltage and the corresponding change in the output current due to the time required by the charges within the device to re-distribute themselves.

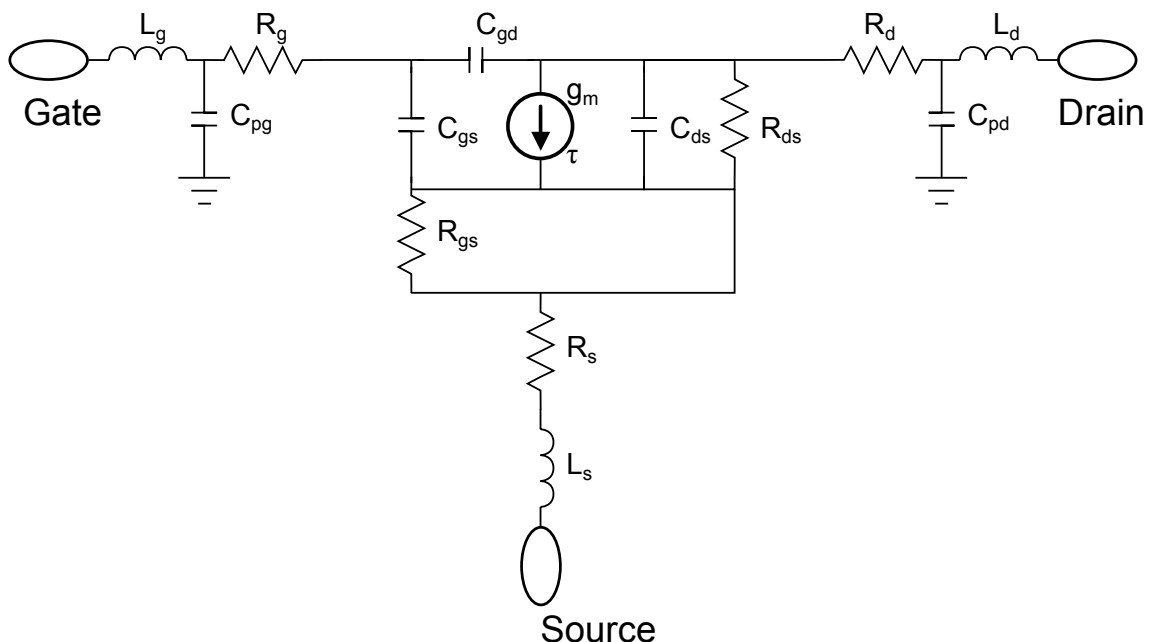


Figure 2.5.1: A small signal transistor equivalent circuit.

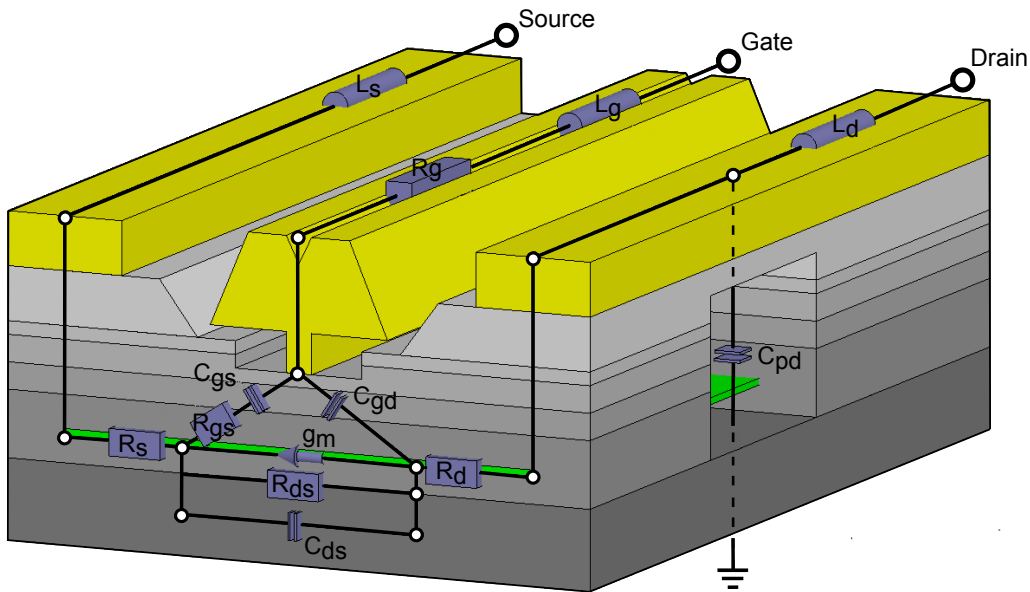


Figure 2.5.2: A 3 Dimensional image of a HEMT illustrating the approximate regions that give rise the various lumped components that make up the transistor's equivalent circuit

Extracting the Equivalent Circuit Parameter

These terms can be found by measuring the S parameters of the device on a probe station, for a certain bias conditions. The procedure is outlined in the following papers [91, 90, 92].

2.6 Noise

Figure 2.1.1 showed that all RF and microwave components add noise to a signal as it propagates through the component. However, there are various forms of electronic noise; some which are thermal in origin, some which are quantum-mechanical in origin, some whose power is independent of frequency, so called white noise sources and some whose noise spectrum shows a frequency dependence. These types include; Nyquist Noise also known as Johnson noise or Thermal noise, which is perhaps the most basic and arises from the random motion of charge carriers within a component due to thermal excitation and shot noise, which is caused by the random fluctuations of charge carriers as they flow

across an energy barrier.

With noise being such a significant feature in amplifiers is it useful to be able to characterise it in terms of a definable quantity. Johnson and Nyquist in 1928 [93, 94] showed that if you connected two conductors together, each with the same resistance and then applied heat to one of them, a current would begin to flow within the circuit. In effect their work showed that it was possible to transfer power from one conductor to the other. Therefore if you take a device capable of measuring a voltage and attach it to either end of a resistive component (figure 2.6.1) it will measure a net voltage of zero but a non-zero root mean squared voltage, which is given by (2.6.1), where k is the Boltzmann constant, B is the bandwidth and T is the physical temperature in Kelvin. (2.6.1) shows that the transfer of power is independent of frequency and it can be shown (Appendix A) that the noise voltage arises due to black body radiation within the conductor itself.

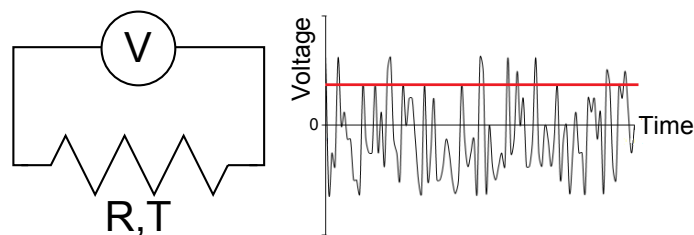


Figure 2.6.1: The voltage output of a resistor of resistance R at temperature T . The red line denotes the root mean squared value.

$$V_n = \sqrt{4kTBR} \quad (2.6.1)$$

This result is actually an approximation that is known as the Rayleigh Jeans approximation and it is valid for all but the highest microwave frequencies and the lowest of temperatures.

Thévenin Equivalent Circuit

(2.6.1) shows that there is relationship between noise and temperature and this relationship allows the noise of some component to be quantified in terms of a noise temperature. Figure 2.6.2 shows a circuit where the noisy resistor of figure 2.6.1 has been replaced by a noiseless resistor R_{in} and a voltage noise generator (V_n) in an arrangement known as a Thévenin equivalent circuit. Connecting this circuit to a load resistor (R_{load}) via an ideal bandpass filter (of bandwidth B) will result in maximum power transfer from the noise source to the load resistor, with the power delivered to the load given by (2.6.2).

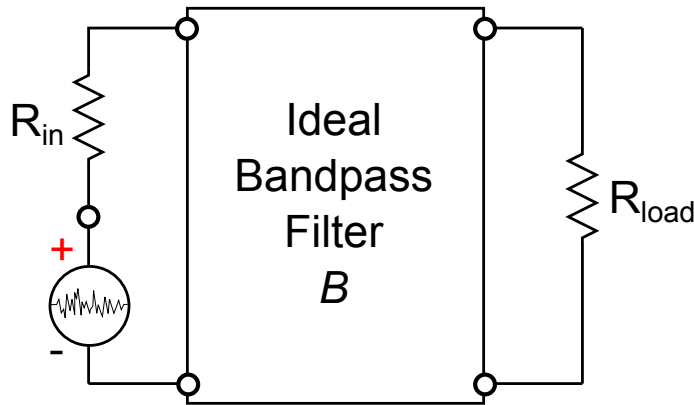


Figure 2.6.2: A Thévenin equivalent circuit. $R_{in} = R_{load}$

$$P_n = \frac{V_n^2}{4R} = kTB \tag{2.6.2}$$

(2.6.2) shows that noise can be expressed as a noise power and that reducing the physical temperature lowers the overall noise power.

Using these relationships it becomes clear that noise sources can be replaced by a resistor of resistance R and temperature T and that this value of T can be tuned to a temperature T_e that will provide the same noise as the noise source. This temperature is known as the equivalent temperature T_e and the resistor is said to have a noise temperature of T_e .

Extending this idea to amplifiers; figure 2.6.3 shows a resistor R_{in} attached to the input

of a noisy amplifier with gain G and a noise temperature T_e , whilst attached to the output is a load resistor R_{load} equal in resistance to R_{in} and attached to the load resistor is noise meter. Since R_{in} is at 0 K, there is no input power in to the amplifier, but the noise meter will still measure a noise power in the load resistor equal to $kGBT_e$, thus it can be said that the amplifier has a noise temperature T_e .

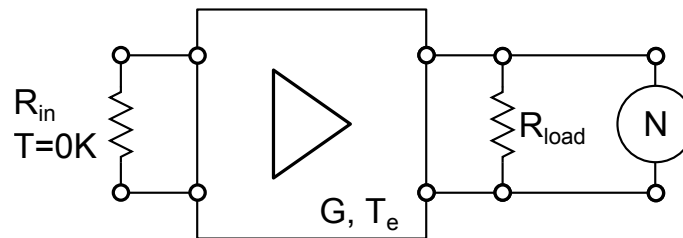


Figure 2.6.3: A noisy amplifier, with an ideal resistor at 0 K on the input and a load resistor and noise meter on the output.

2.6.1 Sources of Noise

By considering the equivalent circuit model (figures 2.5.1 and 2.5.2) it is possible to use the idea of noise power to identify regions within the transistor where noise is generated (figure 2.6.4) and to speculate on the noise generation mechanisms. The Thévenin equivalent circuit can then be used to assign mean squared voltage $\langle e_g \rangle$ and current $\langle i_d \rangle$ noise values to these regions. This treatment is further summarised in [95]

Channel Noise

The most obvious source of noise is the active channel itself, since there is a current flowing between the drain and the source (I_d) and the semi-conductor has a resistance. Although impurity scattering has been greatly reduced in the HEMT and cryogenic cooling reduces phonon scattering further, anything that causes a fluctuation in the electron mobility will add noise to the system. Channel noise was first outlined by Van der Ziel [96] and is described by (2.6.3), where the terms have their standard meanings and P is a fitting factor, with a value of 1 for $V_d = 0$.

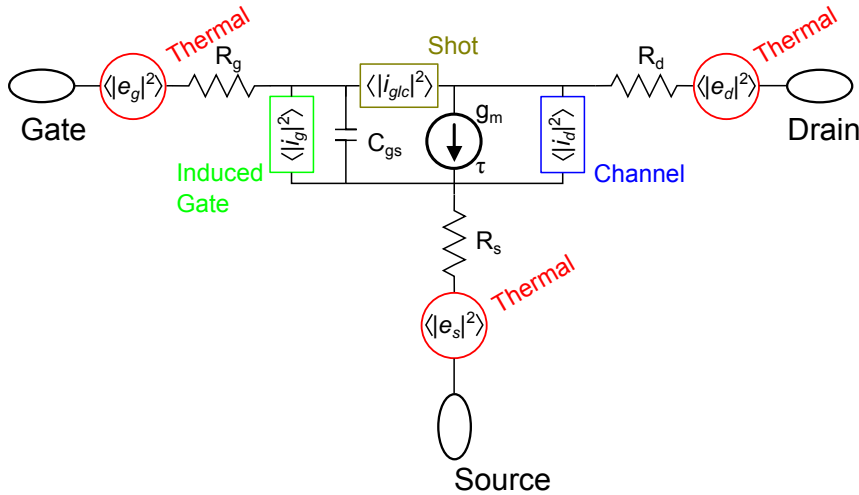


Figure 2.6.4: A simplified noise equivalent circuit showing the regions in a transistor that lead to generation of noise. Developed from: S. Prasad 2009, figure 2.12 [95].

$$\langle |i_d|^2 \rangle = 8kT g_m B P \tag{2.6.3}$$

There are two interesting results from (2.6.3); firstly channel noise is proportional to temperature so the noise has a thermal origin. Secondly it is proportional to g_m , which is also to be expected since a higher g_m means a higher current density in the channel and so more electrons to undergo scattering. This dependence also means that in all likelihood, a transistor that is biased for maximum gain will not be biased for minimum noise.

Thermal Noise

Thermal noise is present in a transistor since the contacts are made of metal, so any current passing through the contact will experience an ohmic resistance. The noise associated with this ohmic resistance can be described by assigning the now familiar noise voltage source (2.6.4-2.6.6) to these regions.

$$\langle |e_g|^2 \rangle = 8kTR_g B \tag{2.6.4}$$

$$\langle |e_d|^2 \rangle = 8kTR_dB \quad (2.6.5)$$

$$\langle |e_s|^2 \rangle = 8kTR_sB \quad (2.6.6)$$

Like the channel noise equations (2.6.4-2.6.6) indicate that cooling the device will reduce the level of thermal noise. Equations (2.6.4-2.6.6) also show that when designing a transistor steps should be taken to try and minimise the resistance of the contacts, indeed in the case of the development of ever smaller gate lengths, the associated rise in r_g would have posed a particular problem, which was solved by the development of the T-shaped gate.

Shot Noise

Shot noise is a quantum mechanical effect and arises whenever a current flows across an energy barrier. In the case of the transistor the gate semi-conductor interface is a Schottky diode and so any current leaking out of the gate across the interface will experience shot noise. Shot noise is described by (2.6.7) where q is the electron charge and I_{glc} is the DC value of the gate leakage current [95].

$$\langle |i_{glc}|^2 \rangle = 8qI_{glc} \quad (2.6.7)$$

Induced Gate Noise

Induced gate noise, which was also predicted by Van de Ziel [97] arises because the gate and the channel are very close together, and so any fluctuation in the channel will induce a corresponding fluctuation in the gate. This effect is described by (2.6.8), where H is a fitting factor, typically between 0.3 and 0.4.

$$\langle |i_g|^2 \rangle = \frac{8kTB(\omega C_{gs})^2 H}{g_m} \quad (2.6.8)$$

(2.6.4 - 2.6.8) show that most sources of noise are in some way dependent on temperature, therefore cooling may offer a route to noise reduction.

Gain Instabilities

In addition to the sources of noise discussed above, instabilities in the gain of the amplifier give rise to Flicker Noise, which has a very strong frequency dependence, typically exhibiting a $1/f$ power spectrum. These gain fluctuations arise due to the development of traps¹⁷ within the semiconductor. It is an issue for amplifiers because detectors are incapable of determining whether or not an increase in power is due to a fluctuation in source temperature or a fluctuation in gain. Its effect on the sensitivity of a receiver system can be seen by extending (1.1.2) to (2.6.9), where G is the gain and ΔG the size of the gain fluctuations [98].

$$\Delta T = T_{sys} \sqrt{\frac{1}{B\tau} + \left(\frac{\Delta G}{G}\right)^2} \quad (2.6.9)$$

2.7 The Modeling of Noise

In order to be able to successfully design an LNA it is useful to have some idea of its noise performance, this is achieved through the use of noise parameters.

2.7.1 Noise Parameters

Whilst the equivalent circuit model outlined in section 2.5 is useful for predicting the S parameters of a transistor, on its own it provides no information regarding the noise

¹⁷These traps develop due to the presence of impurities or dislocations within the semiconductor material that allow the formation of energy levels between the valence and conduction band (forbidden region).

properties of the device. However work by a variety of authors including: Van der Ziel [96, 97], Fukui [99], Cappy [100], Pucel [101] and Pospieszalski [102] has led to the development of several sets of noise parameters.

One such commonly used set is comprised of 4 noise parameters, which are described by Pospieszalski in [103] (2.7.1-2.7.4) as; T_{min} the absolute minimum noise temperature, X_{opt} the optimum source reactance, Γ_{opt} the optimum source reflection co-efficient and R_{opt} the optimum resistance. Z_{opt} is the optimum source impedance and N is given by (2.7.5) and T_0 is 290 K. g_n is the noise conductance, R_n is the noise resistance and ρ is a correlation coefficient between voltage and current noise sources. These parameters can be determined by making measurements of a two port's noise figure for four or more source impedances at a given frequency [74, 104].

$$T_{min} = 2T_0[N + \Re(\rho\sqrt{R_n g_n})] \quad (2.7.1)$$

$$X_{opt} = \frac{\Im(\sqrt{R_n g_n})}{g_n} \quad (2.7.2)$$

$$\Gamma_{opt} = \frac{Z_{op} - Z_0}{Z_{opt} + Z_0} \quad (2.7.3)$$

$$R_{opt} = \sqrt{\frac{R_n}{g_n} - X_{opt}^2} \quad (2.7.4)$$

$$N = R_{opt} g_n \quad (2.7.5)$$

A requirement on these parameters is that in order for them to represent a real device, (2.7.1) must obey the following inequality (2.7.6).

$$\frac{4NT_0}{T_{min}} \geq 1 \quad (2.7.6)$$

2.7.2 The Pospieszalski Equivalent Temperatures

M. Pospieszalski has introduced an alternative set of noise parameters [105, 102] that are particularly useful for LNA development. Figure 2.6.4 and figure 2.5.1 showed that noise is generated at different regions within a transistor and that these regions coincide with a resistive component, whilst section 2.6.1 showed that these noise sources can be defined in terms of either a mean squared voltage or current and the Thévenin Equivalent Circuit shows that noise sources can be related to a noise temperature. Consequently the Pospieszalski approach involves assigning a noise temperature to these resistive equivalent circuit components.

Accordingly the passive extrinsic components (R_g, R_d, R_s) are assigned a noise temperature T_a which is equal to the ambient temperature. The gate source resistance is assigned a noise temperature T_g or gate temperature, which interestingly is approximately equal to the physical temperature [103]. The remaining resistive component the drain source resistance is assigned a noise temperature T_d or drain temperature, which is far higher than physical temperature. The resulting Pospieszalski noise equivalent circuit can be seen in figure 2.7.1.

The Pospieszalski noise temperatures are related to the traditional noise parameters by (2.7.7-2.7.10).

$$T_{min} = 2 \frac{f}{f_t} \sqrt{g_{ds} r_{gs} T_g T_d + \left(\frac{f}{f_t}\right)^2 r_{gs}^2 g_{ds}^2} + 2 \left(\frac{f}{f_t}\right) r_{gs} g_{ds} T_d \quad (2.7.7)$$

$$R_{opt} = \sqrt{\left(\frac{f}{f_t}\right) \frac{r_{gs} T_g}{g_{ds} T_d} + r_{gs}^2} \quad (2.7.8)$$

$$X_{opt} = \frac{1}{\omega C_{gs}} \quad (2.7.9)$$

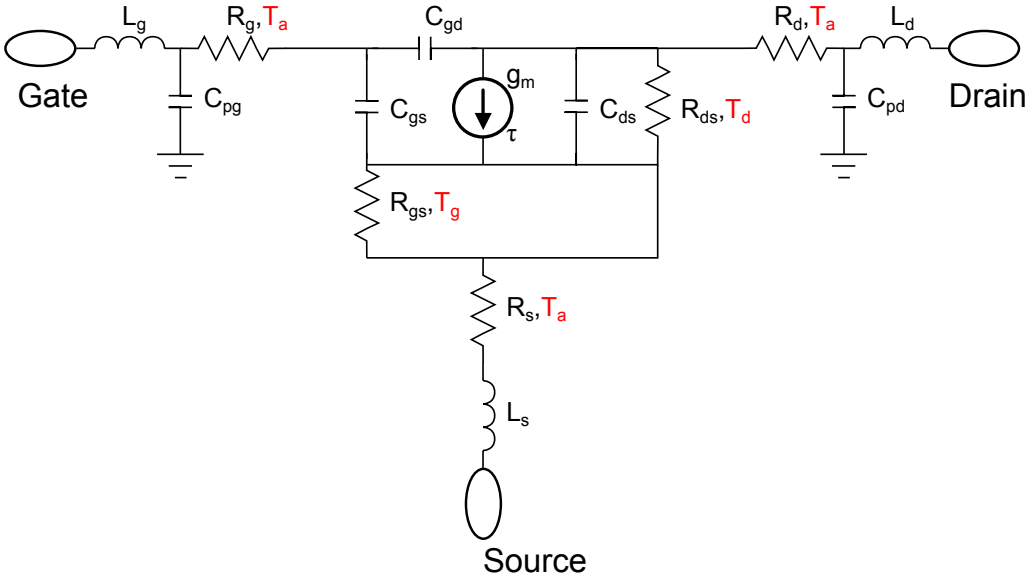


Figure 2.7.1: The Pospieszalski noise equivalent circuit. The temperature parameters assigned to the various resistive components can be seen in red.

$$g_n = \frac{f^2}{f_t} \frac{g_{ds} T_d}{T_0} \tag{2.7.10}$$

The values T_g and T_d are of interest from the point of view of enhancing the noise performance of LNAs. In particular their behaviour with respect to physical temperature, whether or not they actually represent physical quantities and their behaviour with respect to drain current.

Chapter 3

Ultra Low Temperature Operations

As was discussed in section 2 and as is widely practised the noise performance of LNAs can be improved by roughly an order of magnitude through the use of cryogenic cooling, typically to ~ 20 K. Until recently the cooling of a large number LNAs below 20 K in the field has not been practical. However, recent developments in cryo-coolers make sub 20 K cooling a possible proposition. The author therefore undertook an investigation into the behaviour of LNAs below 20 K with the aim of cooling the amplifiers to 1 K. Two potential improvements in the LNA's operations were investigated. First; MIC based amplifiers were used to investigate any reduction in the drain current required for minimum noise, no improvement was expected, but any improvement would ease the level of power dissipation required on any future large N-pixel telescope. More success was expected in the second investigation where two MMIC based amplifiers were cooled to 2 and 4 K respectively. This was done in order to investigate the relationship between noise temperature and physical temperature down to these low temperatures. Before discussing these findings however, this chapter will elaborate further on the relationships between the Pospieszalski noise equivalent temperatures and physical temperature and detail the cryostat and the noise test set-up that was used to carry out these investigations.

3.1 Noise Temperature and Physical Temperature

Chapter 2 showed that the physical temperature does have a considerable effect on the noise temperature of the device. Since radio astronomy generally requires the lowest noise possible, amplifiers are typically cooled within a cryostat to around 20 K, several studies have been carried to see how this affects the equivalent circuit model [106, 107], studies have also been carried out by Pospieszalski into the noise behaviour of the transistor at different temperatures [105, 89, 102, 108, 103]. Monte Carlo simulations have also been carried out in to the properties of electron transport in HEMTs at temperatures between 300 K and 16 K [109]. However, there have only been a few studies [89, 110, 111] into the behaviour of transistors below 20 K and none of these looked at the relationship between noise temperature and physical temperature [112]. Several studies have looked at this relationship at a variety frequencies (C-band [113], Ka-band [114] and 40 GHz [115]) but they used MIC based amplifiers and none of these studies looked at the noise performance below ~ 15 K.

3.1.1 Noise Parameters and Temperature

Thanks to the work of Pospieszalski and the studies outlined above the behaviour of the noise parameters and the noise equivalent temperatures with respect to physical temperature is fairly well understood. In the case of the standard noise parameters work by M. Pospieszalski [89] has shown that cooling a transistor from room temperature to 12.5 K has a considerable impact on the 4 noise parameters (2.7.1-2.7.4). Table 3.1 shows an extract of two tables found in [89].

Table 3.1 shows three important results of cooling a transistor, firstly T_{min} the absolute minimum noise temperature is reduced by about an order of magnitude, as expected. Secondly the gain of the device improves, which is useful and thirdly the variation in R_{opt} implies that a matching network (part of the RF circuit) designed for room temperature

3.1. NOISE TEMPERATURE AND PHYSICAL TEMPERATURE

Transistor	T_{phys} [K]	Noise Parameters				T_{min}		Gain [dB]
		T_{min} [K]	R_{opt} [Ω]	X_{opt} [Ω]	g_n [mS]	Min	Max	
MGF1412	297	122	13.4	40	11.5	-	-	9
	12.5	20	7.1	38	3.7	18	26	12
FSC10FA	297	125	10.7	33	12.8	-	-	7.3
	12.5	20	3.6	32	6.6	15	24	9

Table 3.1: Comparison of the noise parameters of two FETs at 297 and 12.5 K, measured at 8.5 GHz. Data sourced from [89].

may not necessarily work as effectively at cryogenic temperatures. Therefore amplifiers that are intended to be operated at cryogenic temperatures need to be designed for cryogenic operation and good room temperature performance does not necessarily guarantee good cryogenic performance.

3.1.2 The Pospieszalski Temperature Parameters

As was outlined in section 2.7.2 the preferred method for modeling the noise behaviour of the LNAs used in radio astronomy is to use the Pospieszalski noise equivalent temperatures T_a , T_g and T_d .

T_a and T_g

Reviewing figure 2.7.1 in section 2.7.2 the resistive components have a noise temperature associated with them. For the extrinsic resistive components this is taken to be the physical temperature. Since the noise in these components is thermal in origin owing to it being generated within the metallic resistive bond pads. The relationship between T_g and T_{phys} is less obvious. Pospieszalski [102] however has shown that T_g scales almost linearly with T_{phys} , which implies that the source of noise associated with r_{gs} is like the extrinsic parameters thermal in origin [103].

T_d

T_d is different however, since the noise temperature associated with r_{ds} is considerably higher than the physical temperature. Pospieszalski has shown that T_d only has a very weak dependence on T_{phys} , but a very strong dependence on the drain source current [103], (the opposite case applies for T_g). Since T_d scales linearly with drain current all devices will have the same value provided that the same bias, gate length and semiconductor layout are used [103].

Despite T_d displaying differing behaviour to T_a and T_g it too may be thermal in origin; Van der Ziel did show a thermal dependence. The differing behaviour with respect to temperature may in part be due to the nature of the environments. In the case of T_a it is associated with metallised components and so these components are easily cooled by thermal connections (bond wires) to the cold chassis. T_g although associated with a resistance that is embedded within the layers of semi-conductor, it is caused by a very weak current and so the level of power available for heating is low compared to the cooling power that the device is exposed too, allowing it to cool to physical temperature. T_d on the other hand is associated with the channel resistance, where a comparatively large current flows and this current will have considerable heating power. Van der Ziel also demonstrated a dependence on the channels transconductance. Since the layers of semi-conductor act as a good thermal insulator, it is possible that the cooling power of the cryostat cannot be brought fully to bare on the conduction channel and so it is held at a constant temperature which is more dependent on drain current than T_{phys} . Indeed comments by Pospieszalski would appear to support this hypothesis. In [102] Pospieszalski notes that the observed T_d values are consistent with results for a “resistor-like” AlGaAs-GaAs structure [116]. Whilst in [103] Pospieszalski notes that T_d does show dependence on T_{phys} for very low drain current densities per unit width.

Very Low Temperatures

As previously mentioned very little systematic research into the variation in noise temperature with respect to ambient temperature has been carried, with only a few reports for MICs and none for MMICs. Munoz [113] showed an almost but not quite linear relationship between noise temperature and physical temperature and noted that there are signs that this may start to break down below 20 K, they also predicted the behaviour of T_d finding that there exists a parabolic dependence on ambient temperature. Duh [114] favoured a quadratic relationship, that is close to linear, whilst Pospieszalski [115] considered only a discrete frequency rather than averaging over a given bandwidth and also reported a similar relationship to that reported by Munoz.

Pospieszalski also considered variations in drain current at a fixed cryogenic temperature, finding that there exists a fairly broad minimum in the noise temperature with respect to drain current, which Pospieszalski puts down to changes in T_d and f_t mutually compensating for each other. [111] did try 1.1.8 K using super-fluid Helium for a GaAs pHEMT¹⁸, reporting a degradation in performance, although they also had problems with their thermal connections at this temperature.

Pospieszalski has discussed theoretically the behaviour of noise temperature with respect to physical temperature [102]. Referring to (2.7.1), Pospieszalski showed that assuming (3.1.1) holds true then $R_{opt} \gg r_{gs}$ and so (2.7.1) simplifies to (3.1.2).

$$\frac{f}{f_t} \ll \sqrt{\frac{T_g}{T_d r_{gs} g_{ds}}} \quad (3.1.1)$$

$$T_{min} \simeq 2 \frac{f}{f_t} \sqrt{g_{ds} T_d T_g} \quad (3.1.2)$$

Since $T_g \propto T_{phys}$ and $T_d \propto I_d$ and assuming an optimally matched input ($Z_s = Z_{opt}$) we

¹⁸pseudomorphic HEMT, a variant of the HEMT structure that uses a thin layer of semi-conductor to overcome differences in lattice constant between the constituent semi-conductors.

can write (3.1.3).

$$T_n \propto \sqrt{T_{phys}} \sqrt{I_d} \quad (3.1.3)$$

Therefore we should see at least a square root improvement in T_n as we decrease the ambient temperature. Pospieszalski has also considered the limit in which $T_g \rightarrow 0$, i.e. $T_{phys} \rightarrow 0$, finding that in this limit T_{min} is given by (3.1.4).

$$T_{min} = 4 \left(\frac{f}{f_t} \right)^2 r_{gs} g_{ds} T_d \quad (3.1.4)$$

Thus a physical temperature should be reached at which no further improvement in noise temperature can be achieved, which is consistent with the idea that drain current is operating in an environment hotter than its surroundings.

3.2 The Cryostat

The cooling investigation was carried out in a specially designed cryostat 3.2.1. The cryostat is based around a 2 stage pulse tube cooler (PTC) manufactured by Sumitomo Heavy Industries (SDK450). The first stage cools a copper base plate and radiation shield to 50 K and pre-cools the second stage. The second stage then cools its own base plate and radiation shield to approximately 3 K. Attached to this base plate, but thermally isolated from it is the 1 K fridge and the LNA (figure 3.2.1a).

The cryostat was assembled by the author with the assistance of Dr S. Melhuish and Mr L. Martinez. In order to make the cryostat suitable for future noise measurements with the Agilent PNA-X (a vector network analyser (VNA)) the author adjusted the design of the cryostat to include the possibility of fitting an input waveguide. This replaced an earlier layout that used a piece of waveguide containing a ‘dog-leg’. This also increased the versatility of the cryostat as it can now be used for cryogenic S parameter measurements.

The author also investigated some infra-red blocking filters for the output waveguide but they were found to be unsuitable for use at these frequencies.

3.2.1 Layout

The internal layout can be seen in figure 3.2.1b. Gas heat switches are used to provide a thermal connection to the 1 K fridge and the variable temperature load. RF signals can be brought into (for S parameter measurements) and out of the cryostat via waveguide. Between the outside and the 3 K plate this waveguide is made of brass. Between the 3 K stage and the DUT¹⁹ (usually the LNA); gold plated stainless steel waveguide is used to minimise the amount of thermal conduction between the two and to allow the LNA's temperature to be varied.

3.2.2 Thermal Break

In order to achieve the very low temperatures required for these investigations, it was necessary to prevent the existence of a continuous thermal connection between the outside flange and the DUT and the DUT and the thermal load. This was achieved through the use of a series of thermal breaks (figure 3.3.3), which were developed from an earlier design [117]. The thermal breaks consisted of two pieces of rectangular waveguide separated in the vertical direction by a small (~ 0.1 mm) gap. An RF-choke (figure 3.3.3a) is used to prevent RF-leakage. To ensure that the RF transmission was unimpeded, simulations of the breaks were carried out by the author using Ansys' High Frequency Structure Simulator (HFSS) [118]. This is a piece of software capable of simulating the behaviour of the electric and magnetic fields within a structure.

In practise the author found the thermal breaks to be unsuitable for use in the output waveguide, as the stainless steel did not provide sufficient rigidity and this caused the

¹⁹Device-under-test.

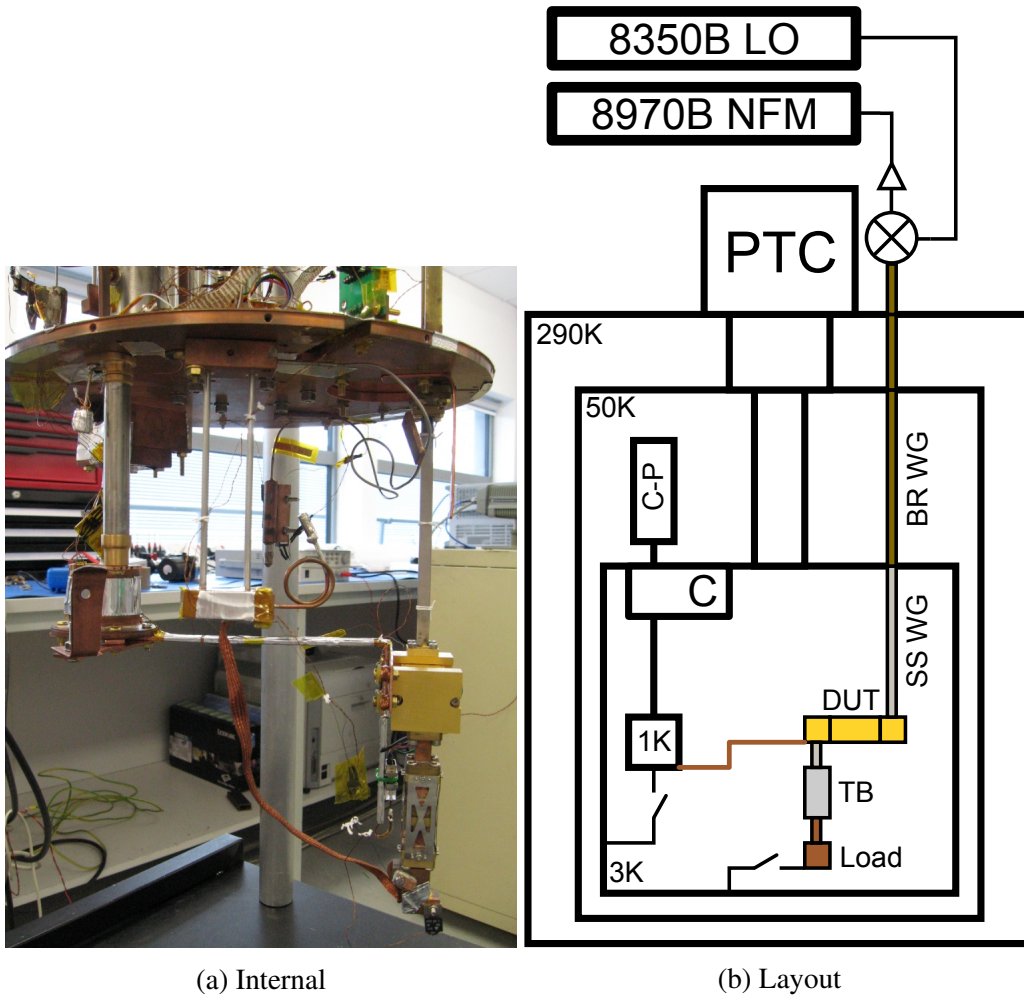


Figure 3.2.1: The layout of the 1 K cryostat. (a) shows the 3 and 1 K stages. The stainless steel waveguide (SS WG) can be replaced with an additional thermal break. C-P is the charcoal pump and C is the condenser.

flanges to move out of alignment. To solve this problem the author replaced the thermal break with gold plated stainless steel which was found to satisfactory (just).

3.2.3 Temperature Control and Monitoring

The temperatures of the various components within the cryostat including the LNA, the reference load, the heat switches and the cryo-pumps can be set through the use of resistors for heating and weak thermal links for cooling. Silicon diode and ruthenium-oxide thermometers, that have been calibrated against a rhodium-iron standard are used to mon-

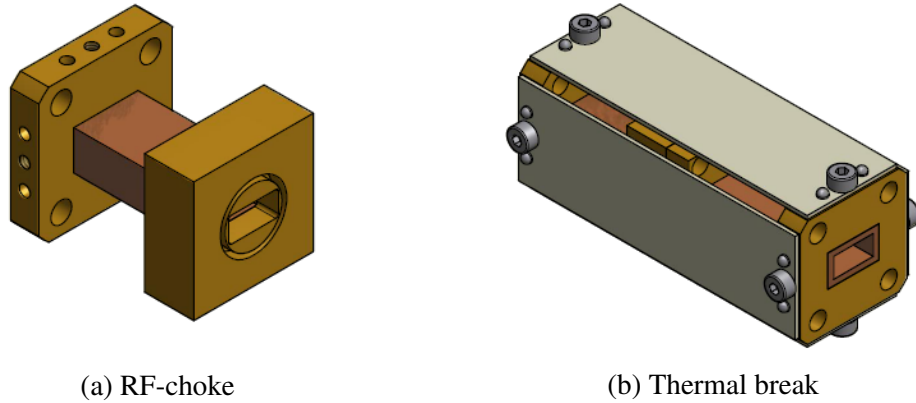


Figure 3.2.2: CAD images of the thermal break. (a) shows the RF choke (ring cavity around the waveguide), (b) shows the design for the thermal break, note the stainless steel coverings underwent subsequent additional milling to lower their thermal conductivity (figure 3.2.1a). CAD image courtesy of A. Galtress.

itor the temperature at various sites throughout the cryostat. The temperatures are controlled by a cryogenic control system that was developed for the QUAD experiment [62].

3.2.4 The 1 K Fridge

Cooling beyond 4 K is achieved through the use of a 4-He adsorption-pumped refrigerator. This is a closed cycle system containing 4-He and a charcoal pump. The charcoal pump (also known as a “cryo pump”) is loaded with charcoal and when heated to ~ 50 K, the helium is de-adsorbed from the charcoal. This helium is then condensed in the condenser (which is connected to the 3 K stage), gravity then causes the helium to fall through a capillary tube into the evaporator chamber at the base of the fridge (denoted 1 K in figure 3.2.1b). During the investigations it was found that for condensation to occur, the biases had to be turned down to avoid excess thermal loading on the 1 K fridge.

The LNA is attached to the 1 K stage via a copper strap, the LNA’s bias cabling is also thermalised along this strap. Once the charcoal has been “hot” for approximately an hour the heater is turned off and the thermal switch connecting the cryo-pump to the 3 K plate is activated, causing the cryo-pump to cool. As it does helium is re-adsorbed by the charcoal forming an efficient vacuum pump. This drop in pressure causes the liquefied

helium in the evaporator to drop in temperature, achieving a minimum temperature in the no load case of 1 K and 2 K with an amplifier. This temperature can be maintained for ~ 45 mins before all of the helium has evaporated and adsorbed back onto the charcoal. At this point the system must be re-cycled.

3.3 The Noise Test Set-up

In order to measure the noise and gain of the amplifier, several pieces of equipment are required. A block diagram of the equipment is shown in figure 3.3.1 and an image can be seen in figure 3.3.2. This test system was assembled by the author and is based on a similar test system used by JBO was amplifier development.

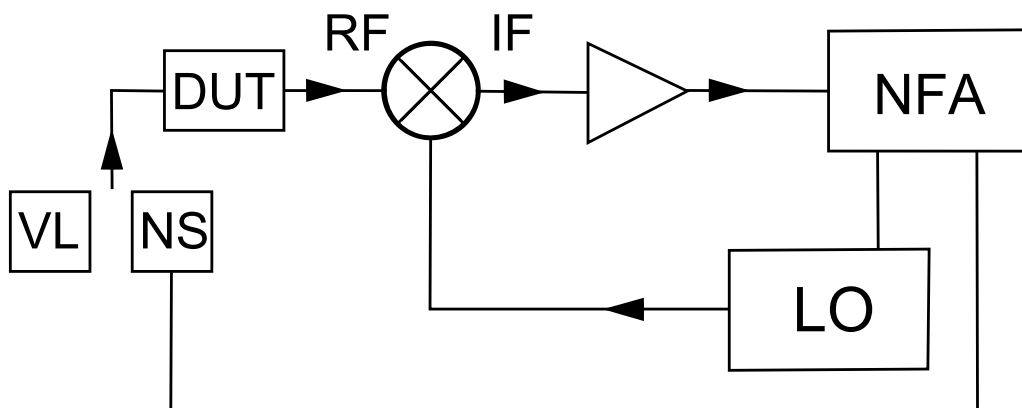


Figure 3.3.1: Block diagram illustrating the noise test set up. The DUT is connected to either a noise source (NS) or a variable temperature load (VL).

3.3.1 The Noise Figure Meter

The noise figure meter (NFM) also known as a noise gain analyser is a radio receiver that is capable of measuring the noise power out of a device under test (DUT). In this case the NFM is a Hewlett Packard (now Agilent Technologies) HP 8350B. However the HP 8350's operating frequency is 50-1600 MHz, therefore it is necessary to down-convert the RF signal from Ka-band to the HP 8350B frequency's band. Fortunately the HP 8350B

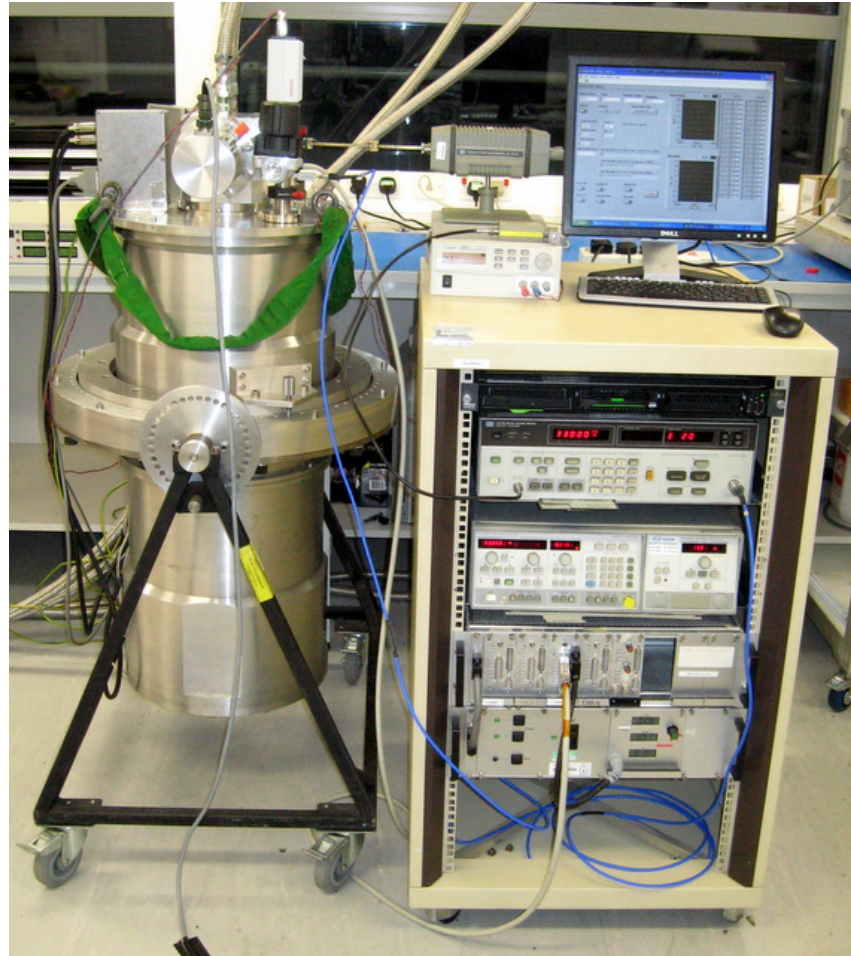


Figure 3.3.2: Image of the noise test set-up

has the capability to be used in conjunction with an external mixer, which can perform the down conversion.

3.3.2 The Mixer

The mixer is an Atlantic Microwave mixer and includes an intermediate frequency (IF) amplifier (biased at +15 V) to amplify IF signal. The mixers role is to down-convert, i.e. lower the frequency of the incoming RF signal. A mixer works by introducing the RF and LO signals to the input of a Schottky junction, which results in the sum of, and difference of the two frequencies appearing at the output, this is known as the IF signal. The workings of a mixer are illustrated by equations (3.3.1) and (3.3.2). For the purposes

of these measurements the RF signal is down converted to 50 MHz.

$$\text{RF Signal: } f_{RF}(t) = \cos 2\pi f_{RF}t \quad (3.3.1a)$$

$$\text{LO Signal: } f_{LO}(t) = \cos 2\pi f_{LO}t \quad (3.3.1b)$$

$$\begin{aligned} \text{IF Signal: } f_{IF}(t) &= f_{RF}(t)f_{LO}(t) = \cos 2\pi f_{RF}(t) \cos 2\pi f_{LO}t \\ f_{IF}(t) &= \frac{1}{2} [\cos 2\pi(f_{RF} - f_{LO})t + \cos 2\pi(f_{RF} + f_{LO})t] \end{aligned} \quad (3.3.2)$$

From (3.3.2) it can be seen that the intermediate frequency is a superposition of the sum and difference of the LO and RF frequencies, therefore with a suitable bandpass filter the required frequency, in this case the difference can be obtained.

3.3.3 Local oscillator

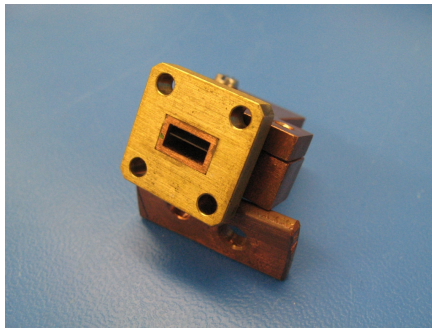
The LO consists of a HP 83550 Sweep Generator which in conjunction with a HP 8355A RF Plug-In Module generates a suitable LO signal. However, the plug in module has a frequency range of 8-20 GHz and so a HP 83500 frequency multiplier is required to multiply the signal up to Ka-band. The LO is connected to the NFM via the HP Interface Bus (HP-IB).

3.3.4 Variable Temperature Load

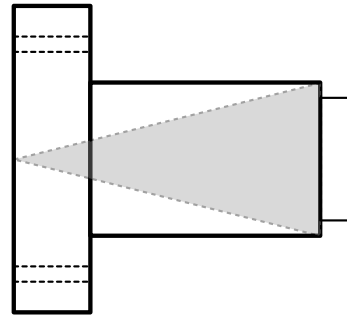
The variable temperature load is a blackbody noise source whose temperature is well known that is connected to the input of the LNA. This can be done optically for example using external loads and a feed horn. In this arrangement the loads can be copper cones whose internal surface has lined with a microwave absorbing material such as eccosorb²⁰. The temperature is varied by using two loads, one that is held at room temperature and one that is immersed in liquid nitrogen at 77 K prior to being placed in front of the feed horn. The noise is then calculated using the Y-factor method from section 3.3.6.

²⁰<http://www.eccosorb.eu/products/eccosorb>

For situations where optical coupling isn't possible, such as inside the 1 K cryostat; the eccosorb can be placed within a section of waveguide and connected directly via a thermal break (to minimise thermal conduction) to the input of an LNA. A $330\ \Omega$ resistor is used in this experiment to vary the temperature of the load from between 3 and 50 K. An image of the load can be seen in figure 3.3.3b.



(a) Load



(b) Layout

Figure 3.3.3: The variable temperature load. (a) shows the load, (b) shows a design drawing for the load, the grey area is eccosorb.

3.3.5 Noise Source

Alternatively room temperature measurements can be carried out using an electronic noise source in this case an Agilent 4530 noise source. The noise source consists of a calibrated diode whose noise is given by a published Excess Noise Ratio (ENR) table, since the noise source is driven by a the NFM, the ENR table must be entered into the NFM. The measurement process involves connecting the noise source to the RF input on the mixer and calibrating the noise test set-up, in effect taking a measurement of the system without the DUT in place. The DUT is then placed between the noise source and the Mixer's RF input (figure 3.3.1) and the measurement is repeated.

3.3.6 The Y-factor

Recalling section 1.2.2; Penzias and Wilson used a technique called the Y-factor to measure the noise temperature of the Bell Labs Antenna. The ideas subsequently expressed in Chapter 2 and the work of Dicke [119] can be used to show the theoretical basis for this technique. The Y-factor approach is based on measuring the ratio of the output power of an LNA for two matched loads of differing temperature, as in figure 3.3.4

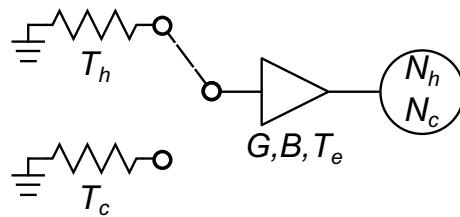


Figure 3.3.4: The Y-factor approach to measuring an LNA's noise temperature.

The output power for each of the loads N_c and N_h is given by (3.3.3), where G is the gain, and T_c and T_h are the temperatures of the cold and hot loads respectively.

$$N_c = GkT_cB + GkT_eB \quad (3.3.3a)$$

$$N_h = GkT_hB + GkT_eB \quad (3.3.3b)$$

The Y-factor is defined by (3.3.4) and rearranging this equation gives the noise temperature of the amplifier (3.3.5).

$$Y = \frac{N_h}{N_c} = \frac{T_h + T_e}{T_c + T_e} \quad (3.3.4)$$

$$T_e = \frac{T_h - YT_c}{Y - 1} \quad (3.3.5)$$

3.4 Drain Current and Temperature

Work by Pospieszalski [103] has indicated that at low temperatures T_d is largely independent of physical temperature but strongly dependent on drain current. If this is the case then the drain current that leads to minimum noise should remain unchanged with decreasing physical temperature. This prediction was investigated for two amplifiers; a Planck EBB²¹ amplifier (see section 4.1.1 for an image) and a newly developed amplifier known as the Transistor in front of MMIC (T+MMIC) that will be discussed further in Chapter 4. The Planck EBB amplifier was developed as part of Planck's Low Frequency Instrument development program and it is based on 4 InP 4x20 μm Cryo-4 HEMTs.

For both amplifiers the noise temperature was measured for a variety of physical temperatures and drain currents (1st stage only). In each case the noise temperature was measured across a 27-33 GHz bandwidth in increments of 250 MHz and was then averaged. Only the drain current of the first stage was varied, since the first stage dominates the noise performance of the amplifier and variations in the 2nd stage were believed to be negligible in terms of noise, which subsequent measurements confirmed.

The results for the Planck EBB amplifier are shown in figure 3.4.1, whilst figure 3.4.2 shows the results for the T+MMIC amplifier.

Conclusion

Figure 3.4.1 hints that a reduction in the minimum bias point with respect to temperature may actually be occurring, although the effect is small. For this LNA minimum noise temperature is occurring between 1.4 and ~ 3 mA. Figure 3.4.1 also shows that the noise temperature is reducing with respect to physical temperature, which is as expected from (3.1.3) and it appears to be tending to ~ 9 K, which is also expected from (3.1.4). The gain (not shown) remained unchanged with respect to temperature although there was a slight

²¹EBB stands for elaborate bread board

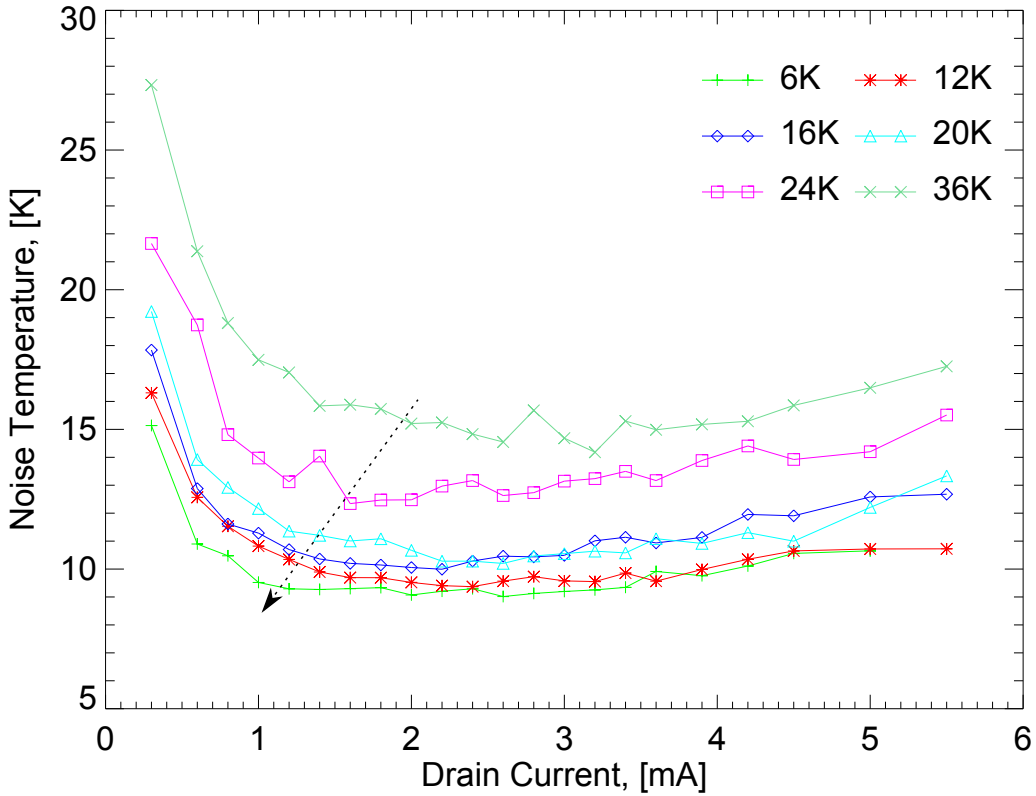


Figure 3.4.1: Mean noise temperature with respect to drain current at various temperatures for the Planck EBB amplifier. $V_d = 0.9$ V. The arrow (drawn by eye) highlights the reduction in I_d for minimum noise.

increase with drain current which again was expected.

Like the Planck amplifier; figure 3.4.2 shows that for the T+MMIC amplifier there is a small reduction in the bias point for minimum noise temperature, with minimum noise also occurring at ~ 2 mA. Figure 3.4.2 also shows that the noise temperature is reducing with respect to physical temperature, and tending to around 9 K. As with the EBB amplifier the gain remain unchanged.

The small reduction in minimum drain current for minimum noise and it supports M. Pospieszalski's view that T_d has a weak dependence on physical temperature. However, it must be stressed that further study will be needed to confirm that this is indeed a real effect.

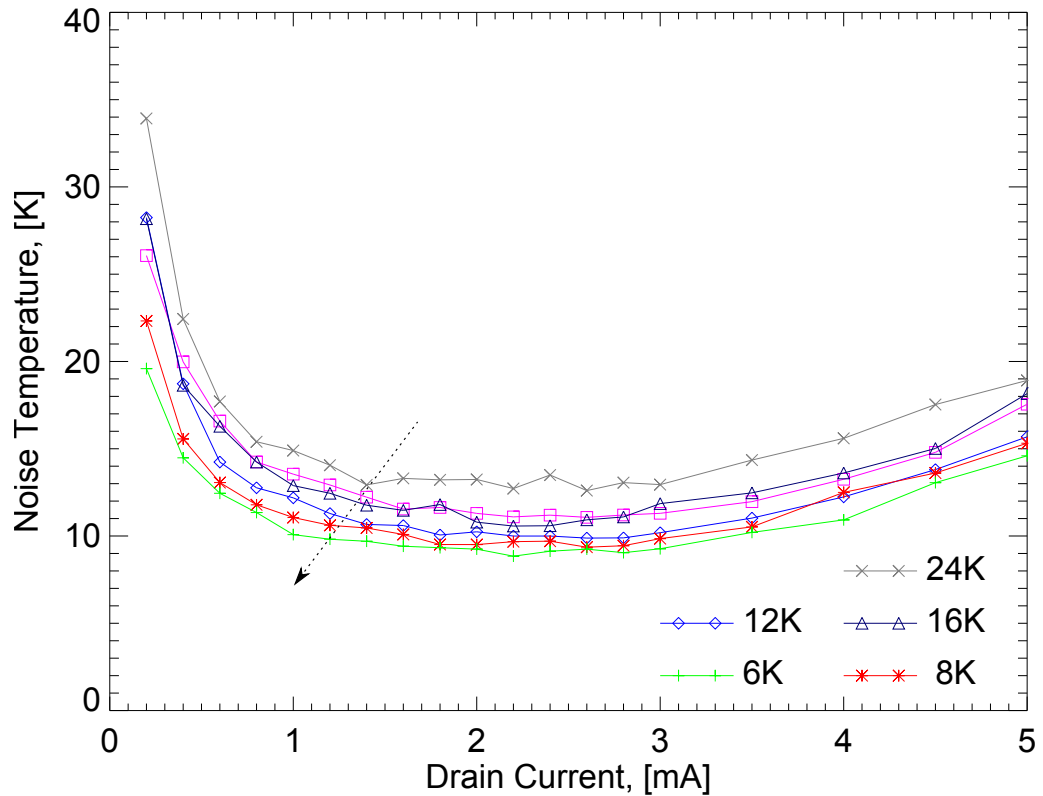


Figure 3.4.2: Mean noise temperature with respect to drain current at various temperatures for the T+MMIC amplifier. $V_d = 0.9$ V. The arrow (drawn by eye) highlights the reduction in I_d for minimum noise.

3.5 Physical Temperature

Whilst seeing a significant reduction in the bias required for minimum noise temperature would have been useful, figures 3.4.1 and 3.4.2 show that the noise temperature continues to fall below 20 K. Therefore further study of this behaviour was deemed appropriate. However, since MMICs are of more interest to future CMB observatories the noise temperature investigations are focused on MMIC based LNAs, although results for the Planck EBB amplifier are reported in [120]. Two amplifiers have been tested and a third produced by the Low Noise Factory²² is awaiting cooling.

²²The Low Noise Factory is based at Chalmers University of Technology, Göteborg, Sweden.

3.5.1 JPL MMIC Amplifier

The JPL MMIC amplifier (figure 3.5.1) is based on a 3 stage Ka-band MMIC [121] that was fabricated by JPL Pasadena at the California Institute of Technology in 2006. Figure 4.1.5 in section 4.1.2 shows a collection of images of the MMIC. The MMIC was integrated into a suitable chassis by E. Artal at the University of Santander.

The amplifier's noise and gain performance can be seen in figure 3.5.2 and the shape of the data is consistent with earlier reported results [121]. Since the noise performance is quite 'noisy' below 30 GHz the noise temperature was measured with the amplifier biased for minimum noise for a 30–36 GHz bandwidth and then averaged. A series of temperature runs covering 2–290 K were carried out and the results are shown in figure 3.5.3. For cryogenic measurements the amplifier was biased at $V_d = 0.7$ V, $I_d = 8.5$ mA, whilst for room temperature this was increased to $V_d = 0.9$ V, $I_d = 20$ mA.

Fit Statistics

The plotting software Gnuplot was used to fit both a linear and a quadratic fit to the data. The results of this analysis are shown in table 3.2.

Fit	a	b	c	Reduced χ^2
Linear	0.495	4.974	-	8.172
Quadratic	0.0005	0.363	7.324	1.411

Table 3.2: Fit statistics for the JPL amplifier. Linear fit: $f(x) = ax + b$, quadratic fit: $f(x) = ax^2 + bx + c$.

Conclusion

Figure 3.5.3 shows that just as was the case for the earlier MIC amplifiers the noise temperature of a MMIC based LNA does continue to fall beyond 20 K, with a near $\sim 30\%$ improvement in the noise temperature between 20 and 4 K. Table 3.2 and figure 3.5.3 also show that the relationship between noise temperature and physical temperature is best

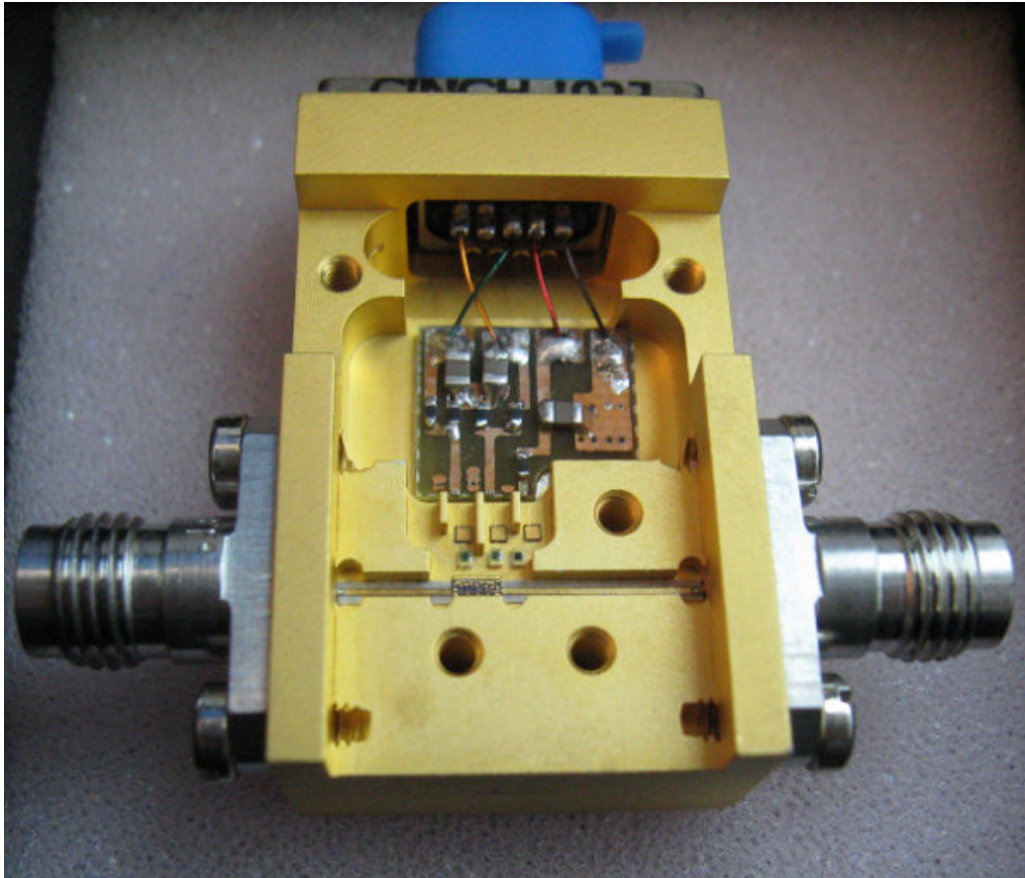


Figure 3.5.1: The JPL MMIC LNA.

described by a quadratic fit, rather than a linear fit. There is however no significant advantage in cooling beyond 4 K with only a negligible improvement in noise temperature being registered.

Figure 3.5.3 also shows that there is good repeatability in the measurement set-up since the temperature runs were taken on different days.

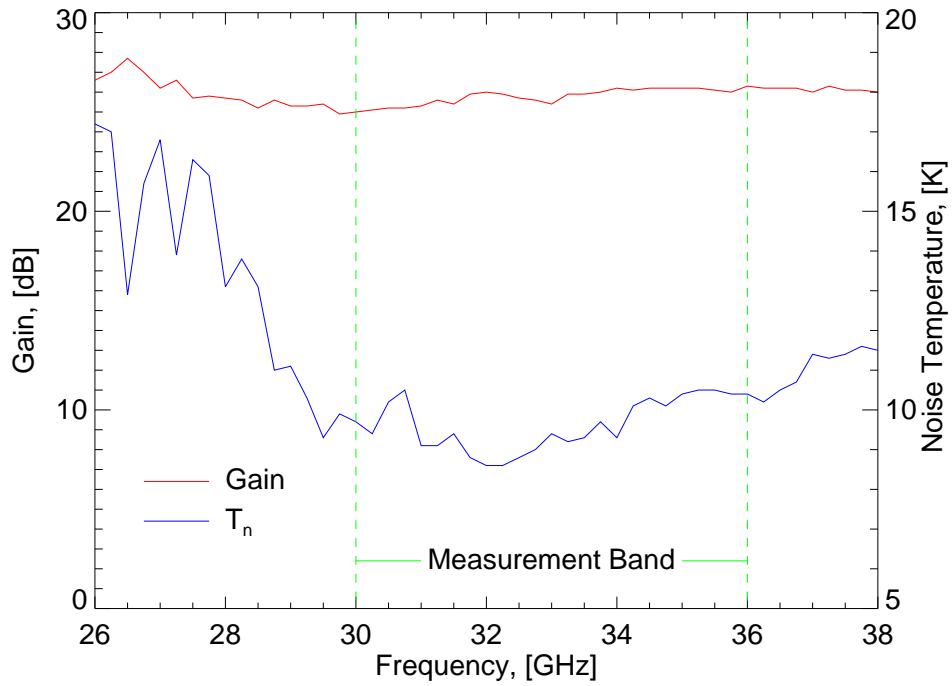


Figure 3.5.2: JPL LNA: noise and gain performance at 6 K physical temperature.

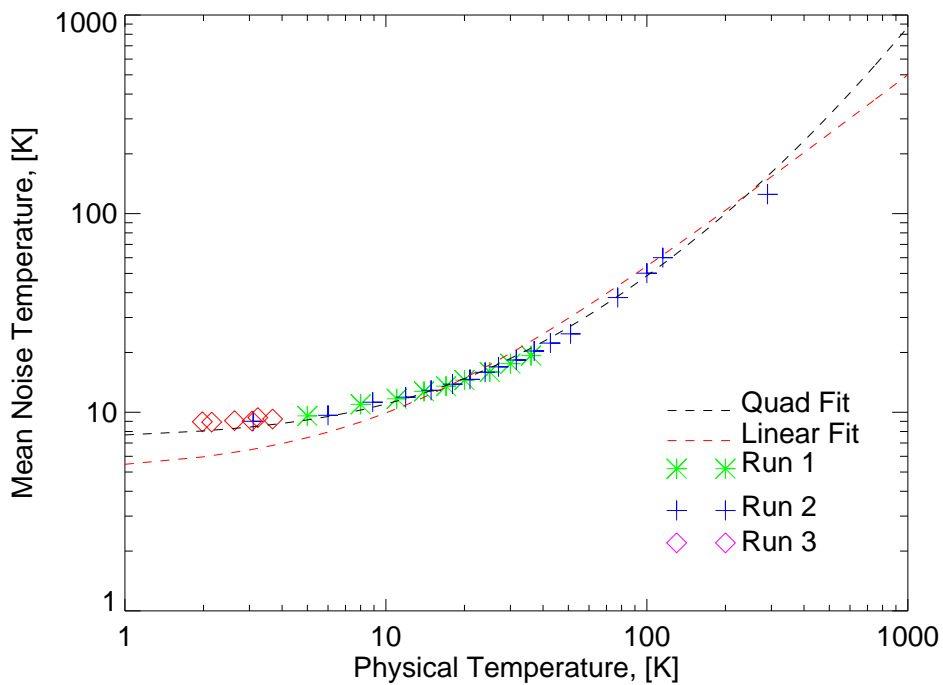


Figure 3.5.3: Mean noise temperature of the JPL MMIC from 2 K to 290 K with a quadratic fit and linear fit.

3.5.2 QUIJOTE 1.3

The QUIJOTE 1.3 amplifier (figure 3.5.4) was a development amplifier that was produced by JBO for the QUIJOTE project. It is based around a 4 stage Ka-band MMIC that was fabricated as part of the European Union's Faraday project. This MMIC and these projects will be discussed further in Chapters 4 and 5. The amplifier's noise temperature was measured across a 28–34 GHz bandwidth in increments of 250 MHz and averaged. The noise and gain of the LNA can be seen in figure 3.5.5. Figure 3.5.5 shows that the gain contains an unusual bump at 30.1 GHz and this also coincides with a jump in the noise temperature. The cause of this bump is unknown, it has been seen in these amplifiers before [122] and the author has raised it with several JBO personnel. Whatever is causing it, it is likely that it is also responsible the feature in the noise temperature.

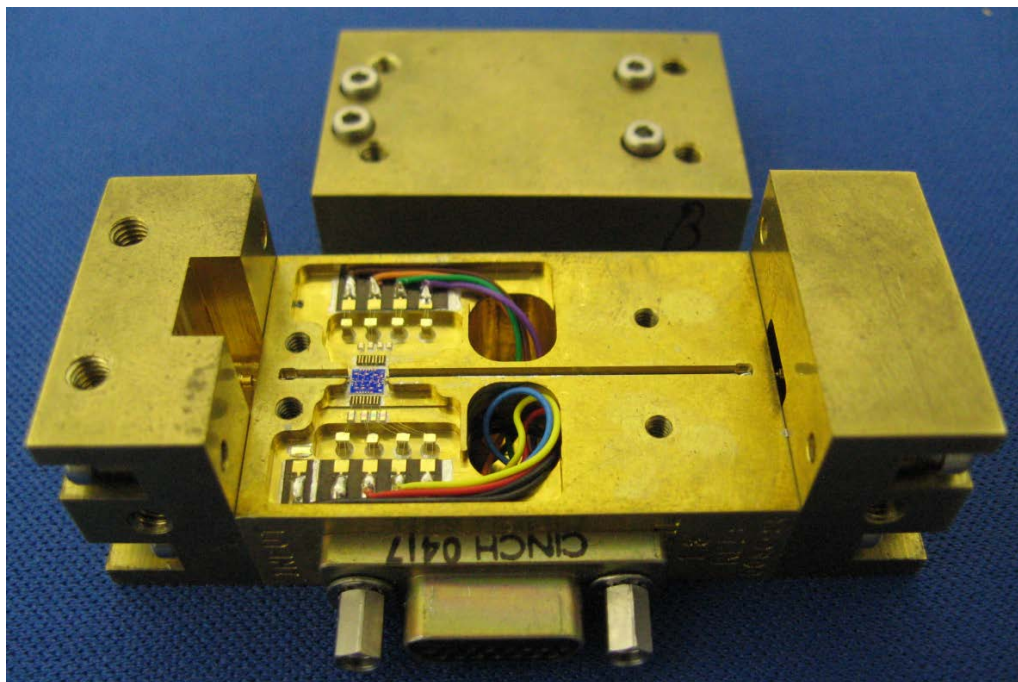


Figure 3.5.4: The QUIJOTE 1.3 LNA. The MMIC can be seen to the left of centre coloured in blue.

As for the JPL MMIC the variation in the mean noise temperature was investigated for a wide range of temperatures (4 -115 K), though it wasn't possible to investigate the

performance at sub 4 K temperatures. This was due to the LNA dissipating too much power and the preventing the condensation of the helium. For cryogenic measurements the amplifier was biased at $V_d = 0.9$ V, $I_d = 5.0$ mA, whilst for the room temperature this was increased to $V_d = 1.3$ V, $I_d = 7.5$ mA.

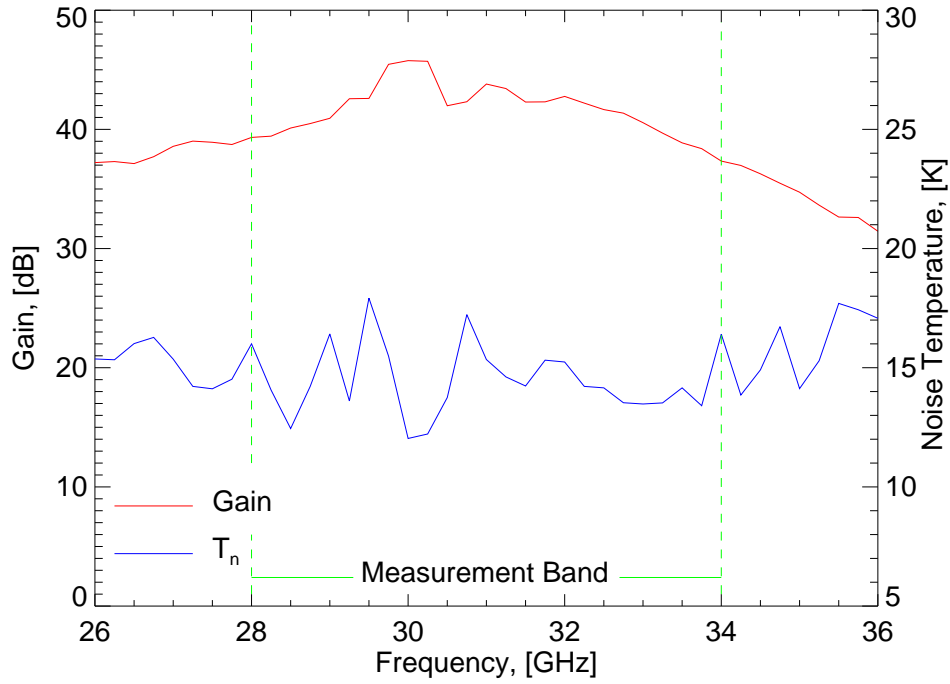


Figure 3.5.5: QUIJOTE LNA: noise and gain performance at 8 K physical temperature. The amplifier was biased at $V_d = 0.9$ V, $I_d = 5$ mA for all stages.

Fit Statistics

The linear and quadratic fit statistics for the QUIJOTE amplifier can be seen in table 3.3.

Fit	a	b	c	Reduced χ^2
Linear	0.626	0.496	-	109.7
Quadratic	0.002	0.176	13.03	3.4

Table 3.3: Fit statistics for the QUIJOTE amplifier.

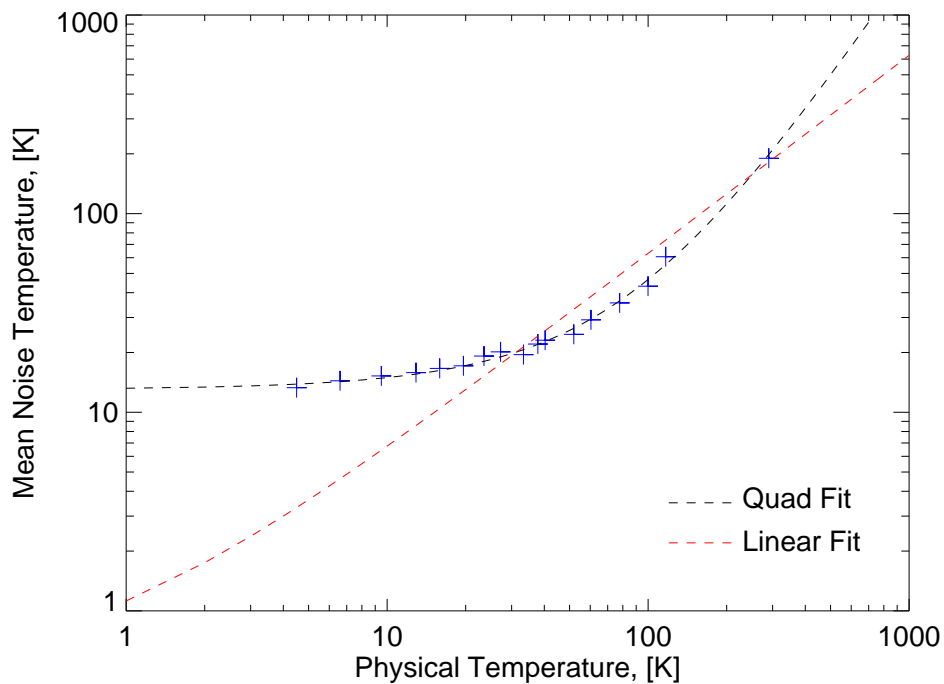


Figure 3.5.6: Mean noise temperature of the QUIJOTE LNA from 4 K to 290 K with a quadratic fit and linear fit.

Conclusion

Just like the JPL amplifier figure 3.5.6 shows that the noise temperature of this MMIC based LNA continues to improve beyond 20 K, with a near there is $\sim 20\%$ reduction in noise temperature when cooling from 20 to 4 K. Again as for the JPL amplifier table 3.3 and figure 3.5.6 show that the relationship between noise temperature and physical temperature is best described by a quadratic fit rather than a linear fit. Interesting for the QUIJOTE amplifier, the preference for a quadratic fit is considerably stronger than was found to be the case for the JPL amplifier.

3.6 Uncertainties

It is estimated that at cryogenic temperatures the uncertainty in our noise measurements is ± 1 K. This estimate is based on a series of repeated observations that were made for

the Planck EBB amplifier²³ and these are shown in figure 3.6.1. Figure 3.6.1 shows the noise temperature of the Planck LNA across its frequency band for a total of 24 frequency sweeps with the sweeps divided into 8 groups with each group containing 3 sweeps. To check for calibration drift between each group the test system was recalibrated and groups 6–8 were also measured the following day. To check for sensitivity to bias the measurements presented in figure 3.6.1 were part of a larger sweep at different first stage drain currents (3.0 mA, 2.0 mA, 1.4 mA and 0.4 mA). For groups 1–4 and 9–10 the sweeps were performed in terms of descending drain current, whilst for groups 7–8 the sweeps were performed in terms of ascending drain current.

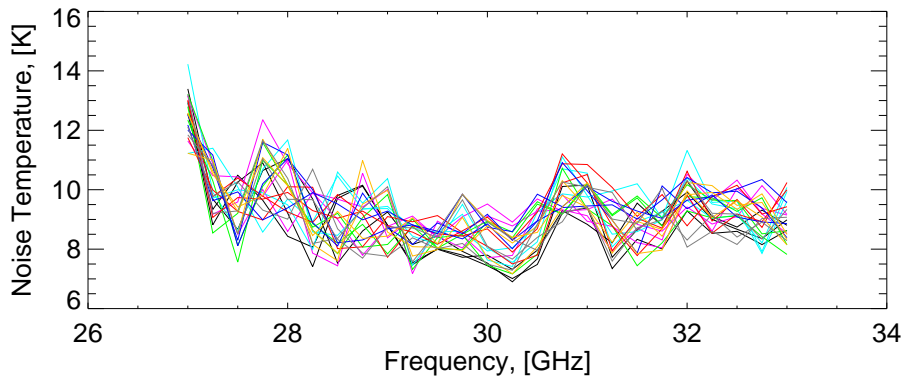


Figure 3.6.1: Repeat measurements of the Planck EBB amplifier. The measurements were performed at 6 K.

For room temperature it is assumed that like noise temperature the error will increase by around an order of magnitude. Thus room temperature uncertainty is estimated as ± 7 K. Both these estimates are consistent with other reported measurements [113] that have used similar techniques.

One potential source of systematic error in the cryogenic measurements is the variable temperature load. In order for the physical temperature of the load to correspond to an equivalent RF temperature it must have a good input match to the input of the amplifier. The quality of the match for the load and thermal break combination is important because

²³The amplifier was biased for all stages at $V_d = 0.7$ V and $I_d = 1.4$ mA

if the match is poor, radiation from the LNA will be reflected back into the LNA by the load. This radiation will then contribute to the radiation from the load that is being used to measure the LNA's noise temperature. The match was measured by a Vector-Network-Analyser (VNA) and was found to be better than -15 dB, which corresponds to a reflection of $\sim 3\%$ which is satisfactory. The match also remained constant with temperature.

3.7 Discussion

The possible minor reductions in the minimum drain current for minimum noise bias point is interesting and is worth further investigation as it may help improve our understanding of transistor noise theory and in particular the exact nature of T_d . To support this potential future research Chapter 5 will outline an amplifier design that may allow this to be done. However, the primary motivation for investigating a reduction in the minimum bias point was to see if it would aid future CMB experiments by allowing more receivers to be cooled to a lower temperature, since it would allow the amplifiers to run at a lower power setting. In this regard, the small gain in noise temperature that would be achieved by reaching a slightly lower physical temperature is unlikely to match the increase in sensitivity that could be achieved by adding extra receivers. Therefore it is unlikely to be of any help.

This particular investigation did however, prove useful in another way since it did allow the author to gain experience in making a large number of measurements with the test equipment

The QUIJOTE amplifier's stronger tendency (when compared to a linear fit) towards a quadratic fit than was found for the JPL amplifier is also of interest and is likely due to the noise temperatures of the two amplifiers. QUIJOTE with its higher noise temperature makes the transition from a state where the noise is principally dominated by thermal effects (T_a and T_g) to one where T_d dominates at a higher physical temperature than is the

case for the JPL amplifier. This may also explain why earlier research showed a relationship between noise temperature and physical temperature that was close to being linear, it is almost linear when T_a and T_g are high but once T_d dominates the true quadratic nature is revealed, in the case of the earlier experiments they simply weren't going low enough in temperature to see the true relationship. This also explains why the JPL amplifier sees a larger reduction in its noise temperature when cooling from 20-4 K than was the case for the QUIJOTE amplifier; the JPL's T_d is lower and so the contribution to its noise temperature from the linear components stays non negligible to a lower temperature. Thus if cooling to 4 K is to be fully exploited, transistors need to be used that possess a low value for T_d , i.e. it will only be effective for the lowest noise transistors.

3.8 Conclusions

This chapter has shown that there may be a small reduction in the minimum drain current required for minimum noise, which supports Pospieszalski's view that T_d is weakly dependent on physical temperature. Figures 3.5.3 and 3.5.6 and the results that are summarised in table 3.4 also show that the noise temperature of MMIC LNAs continues to decrease as you cool beyond 20 K. However, there appears to be no significant advantage in cooling beyond 4 K with only a minor decrease in noise temperature being registered.

Amplifier	297 K	20 K	4 K	2 K
JPL	155	14.5	9.5	8.9
QUIJOTE 1.3	200	17.2	13.2	-

Table 3.4: Noise Temperatures for selected physical temperatures for the JPL and QUIJOTE 1.3 amplifiers.

This chapter has also explained why earlier reports of the relationship between noise temperature and physical temperature showed that it was close to being linear. In reality it is quadratic but the quadratic nature only becomes fully apparent when you cool to very

low temperatures. Again this is consistent with Pospieszalski's findings that at very low temperature only T_d should be of significance.

This research has concluded by showing the importance of a good low T_d transistor for low noise applications. The next step is to investigate the relationship between T_d and T_{phys} , using a variant of the amplifier outlined in the following chapter.

Chapter 4

The Transistor in front of MMIC

(T+MMIC) LNA

MICs and MMICs represent the current two approaches to transistor based LNAs, with each approach possessing certain advantages over the other. This chapter presents the author's work concerning the development of an LNA based on a hybridisation of these two technologies. This hybridisation aimed to use a discrete transistor in front of an existing MMIC based LNA to produce an amplifier with a noise temperature lower than that of the MMIC only amplifier. Known as the T+MMIC, this chapter covers the development of the amplifier from its original theoretical foundations, the development of a suitable module and RF circuit, the author's modeling of the amplifier, its testing, its performance and the author's thoughts on potential improvements. The chapter also elaborates further on the MIC and MMIC approaches to LNAs that were originally mentioned in Chapter 1.

4.1 LNAs

As has been previously outlined LNAs form the most important part of the highly sensitive coherent receivers that are used in radio astronomy. They are designed such that they

Band	Type	Noise Temp (K)	Technology	Reference
C	MMIC	3	130nm InP HEMT	[123]
X	MIC	4	100nm InP HEMT	[110]
Ka	MIC	5	100nm InP HEMT	[124]
Q	MIC	8	100nm InP HEMT	[124]
W	MMIC	22	35nm InP HEMT	[88]

Table 4.1: Current state of the art LNAs for selected frequencies and their respective technologies.

simultaneously possess both a very low noise temperature, and a reasonable amount of gain, typically between 25 and 35 dB depending on the frequency. Table 4.2 shows the current lowest noise temperatures that have been achieved for several frequencies.

At the heart of an LNA are the transistors, for radio astronomy applications they are usually an InP based HEMTs (see section 2.4) and surrounding these transistors are a variety of other components, all of which have a crucial role to play in determining the LNAs overall performance. These components can either be laid out in a module as discrete components, in an arrangement known as a Microwave Integrated Circuit (MIC), or they can be integrated on to a single chip, known as a Monolithic Microwave Integrated Circuit (MMIC).

4.1.1 MIC LNAs

MIC LNAs such as the one in figure 4.1.1 are characterised by the use of discrete components individually placed and glued within a metal module, with the components connected by a series of microstrip lines and bond wires.

The Transistor

The transistor is glued to the module with an epoxy, the required electrical biasing and the RF signal are supplied to the bond pads via bond wires, whilst the source pads are

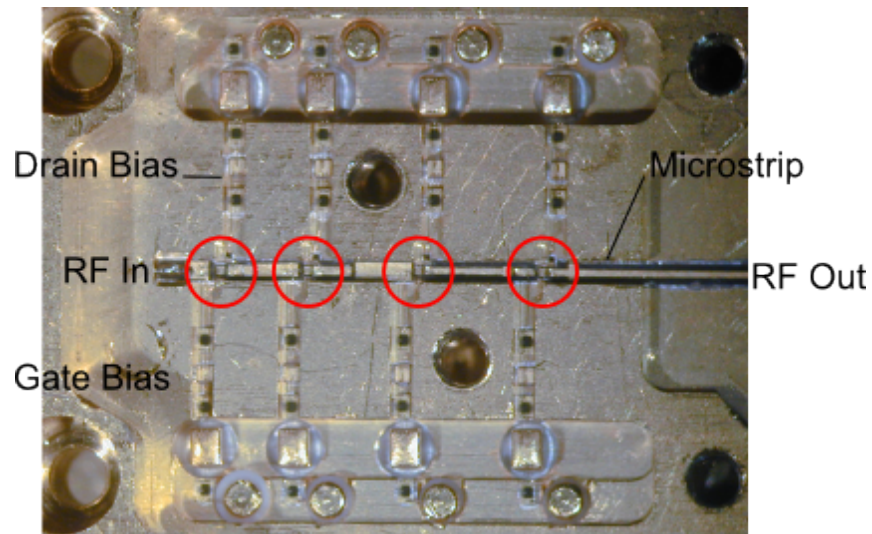


Figure 4.1.1: A MIC LNA. The transistors have been circled and the key features labelled.

directly bonded to the module using bond wires.

The Capacitor

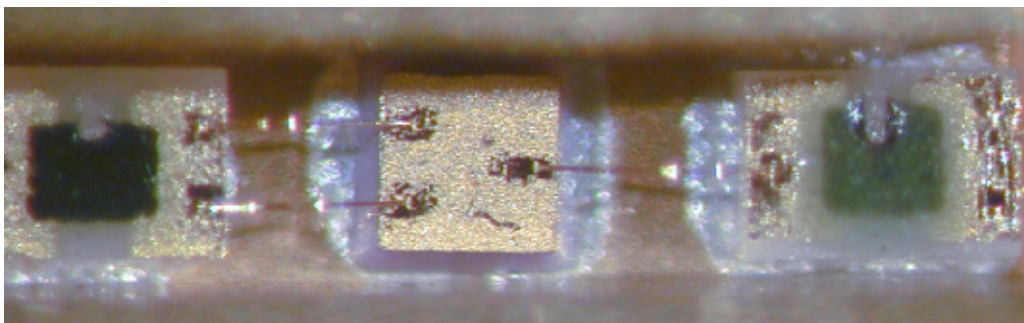


Figure 4.1.2: An MIC resistor and capacitor LNA. From left to right: resistor, capacitor, resistor. Bond wires can be seen connecting the components.

Capacitors (figure 4.1.2) have two roles within the LNA circuit. When placed within the bias circuit they are used to de-couple the RF signal from the external bias circuit. They are also used to block the DC biasing of one transistor from spreading along the RF circuit to the next transistor. Hence DC blocking capacitors can be found on either side of a transistor²⁴. The layout of a blocking capacitor can be seen in figure 4.1.3. By placing

²⁴If the LNA has a waveguide input / output a blocking capacitor is not required between the waveguide and the transistor as the waveguide to microstrip transition will act as a DC block.

the capacitor on the microstrip in such a way the RF signal can propagate via the bond wire and the dielectric, whilst the DC signal is blocked by the capacitor's dielectric.

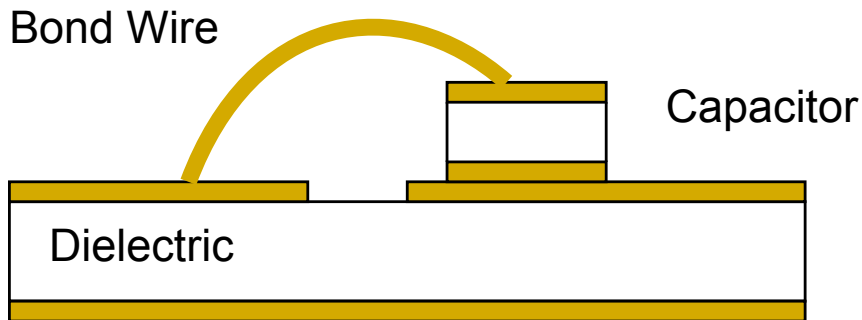


Figure 4.1.3: The layout of a DC blocking capacitor. the discontinuity in the top conductor and the capacitor prevent the propagation of a DC signal.

Resistors

These are generally made using thin film technologies²⁵. Their role is to provide stability to the circuit.

Microstrip

Microstrip is one particular example of an RF transmission line (others include waveguide, co-axial cable and stripline), however unlike co-axial cable and waveguide the electro-magnetic fields propagate in two distinct regions (typically air and dielectric) with differing dielectric constants, as can be seen in figure 4.1.4.

Microstrip is used to connect the transistors to one another, to present the transistor with the correct impedance for minimum noise or maximum power transfer, which is achieved through the use of a matching network and to connect the transistor stages to the amplifier's input and output.

The impedance of a microstrip is determined by the width of the top conductor, the thickness of the dielectric and its dielectric constant (ϵ_r). The characteristic impedance

²⁵State of the ART is one such manufacturer. <http://www.resistor.com/pthin.html>

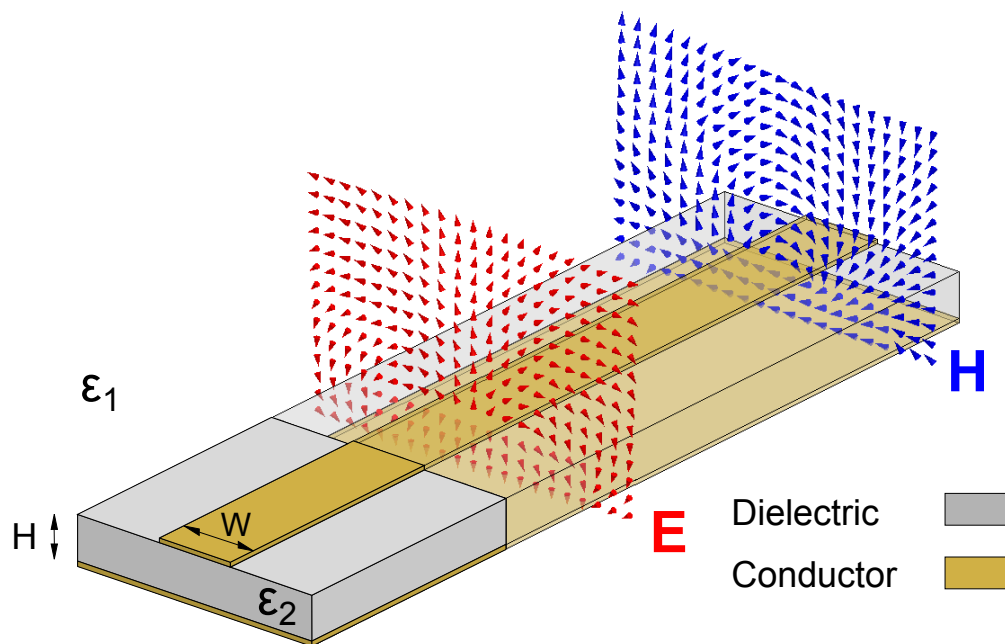


Figure 4.1.4: A cross-sectional view of a typical microstrip, showing the dielectric, the conductors, the directions of the electric (\mathbf{E}) and magnetic (\mathbf{H}) fields and the dimensions that dictate the microstrip's primary characteristics. Note the differing dielectric constants of the two regions.

can be calculated from (4.1.1) where ϵ_e is the effective dielectric constant, which is given by (4.1.2). An effective dielectric constant is used in order to compensate for the fact that parts of the field are propagating through dielectrics with differing dielectric constants.

$$Z_0 = \begin{cases} \frac{60}{\sqrt{\epsilon_e}} \ln \left(\frac{8H}{W} + \frac{W}{4H} \right) & \text{For } \frac{W}{H} < 1 \\ \frac{120\pi}{\sqrt{\epsilon_e [\frac{W}{H} + 1.393 + 0.667 \ln(\frac{W}{H} + 1.444)]}} & \text{For } \frac{W}{H} > 1 \end{cases} \quad (4.1.1)$$

$$\epsilon_e = \frac{\epsilon_r + 1}{2} + \frac{\epsilon_r - 1}{2} + \frac{1}{\sqrt{1 + 12H/W}} \quad (4.1.2)$$

The length l of microstrip line required to give a certain phase shift ϕ (in degrees) can be found by using (4.1.3), where f is the frequency and c is the speed of light. The phase shift produced by a length of microstrip line is also known as the line's electrical length.

Material	ϵ_r	$\tan \delta$
Cuflon	2.05	0.00045
Teflon	2.08	0.004
Quartz	3.78	0.0001
Alumina	9.5	0.0003
GaAs	13.0	0.006
InP	12.3	0.009

Table 4.2: Dielectric constants and loss tangents for typically used dielectrics. Data sourced from [125, 126, 127].

$$l = \frac{\phi(\pi/180^\circ)c}{\sqrt{\epsilon_e}2\pi f} \quad (4.1.3)$$

The third figure of merit for microstrip lines is the loss tangent (δ), which describes the loss that occurs within the dielectric. It is important for noise considerations as the lower the loss tangent the less noise that a given length of microstrip will contribute to the overall circuit noise.

Bond Wires

The bond wires are used to perform the connections between the various components. They are generally made of gold and for Ka-band possess a diameter of between $12.7 \mu\text{m}$ and $17.8 \mu\text{m}$ (0.5 and 0.7 mil). The source bond wires can also be used to ensure that the transistor is simultaneously matched for both noise and gain via a process known as source inductive feedback [128].

Current State of the Art

The current state of the art Ka-band MIC LNAs were developed for ESA's Planck LFI [124] by the Jodrell Bank Observatory (JBO) in the mid 2000's. These LNAs were based on four discrete Indium Phosphide (InP) 100nm gate length HEMTs, and the lowest noise amplifiers possessed an absolute minimum noise temperature of 5 K and average noise

temperature of 8.1 K for a 27–33 GHz bandwidth.

4.1.2 MMIC LNAs

Historical Development

MIC based amplifiers are however not the only route to low noise amplification. Over the last two decades there have also been advances in the development of MMIC LNAs. These amplifiers integrate all of the transistors, transmission lines and matching networks onto an individual chip. The first MMIC was developed in 1964 [129] on silicon, although due to the high loss of the silicon substrate it wasn't very successful. The first successful MMIC LNA was developed in 1968 [130] by Mehal and Wacker on GaAs.

A MMIC LNA

Figure 4.1.5 shows a current state of the art Ka-band MMIC LNA; with close ups of the individual components, illustrating the way in which the various components are integrated onto one chip.

This particular MMIC (figure 4.1.5a) is a 3 stage LNA, the 3 transistors can be seen positioned in the RF line in the lower third of the MMIC. The 3 stages share a common drain voltage, which can be seen by following the lines emanating from the drain voltage bond pad on the top right of the MMIC. The first stage has its own gate voltage, whilst the 2nd and 3rd stages share a common voltage. DC blocking capacitors can be seen just to the right of the transistors, close to the points where the drain voltages join the RF transmission line. Figure 4.1.5b shows how the transistors are integrated into the MMIC's substrate. Figure 4.1.5c shows the way in which other components make use of a MMIC's 3 dimensional architecture in order to integrate themselves into the substrate. *A* is the via (pronounced ve-a) that allows the source rail to gain access to the MMIC's ground plane. *B* is a capacitor, *C* is a resistor.

MMIC vs MIC

MMIC and MIC based LNAs both have their advantages and disadvantages over one another. The MMIC's integrated nature gives it several advantages over the MIC approach. For example individual LNAs are easy and cheap (though there is a large initial cost) to mass produce, which is of importance to future telescopes that will involve large numbers of receivers such as the Q/U-Imaging-Experiment (QUIET) [66]. Mass production also results in many similar LNAs, thus allowing an easier management of their systematic effects. Unfortunately however their integrated nature means that MMICs also have drawbacks.

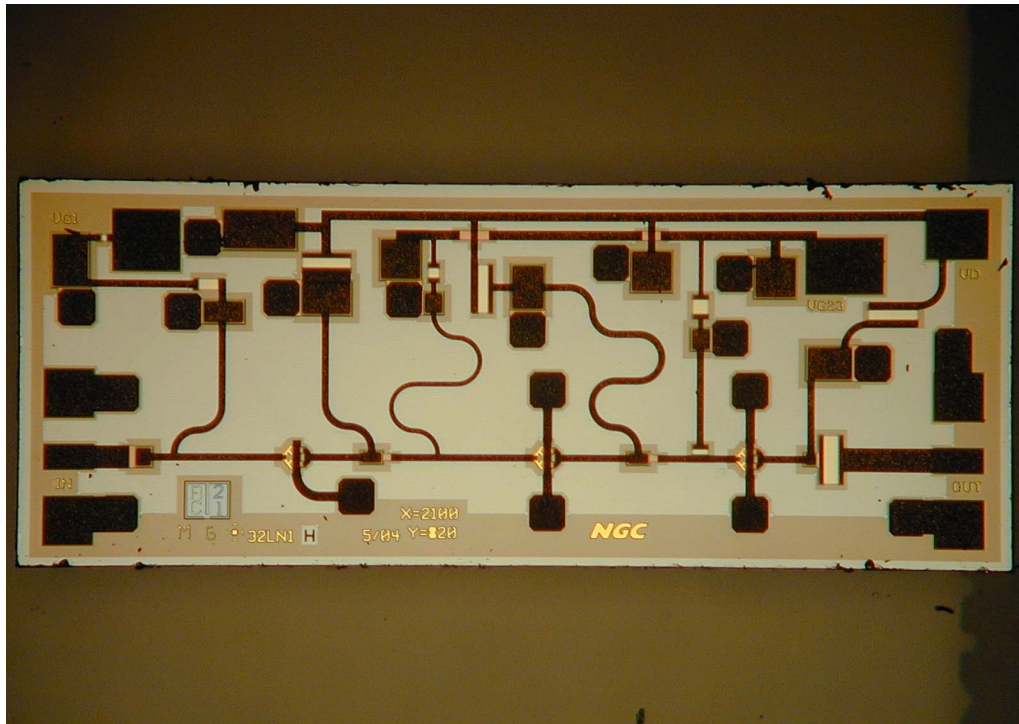
MIC designs by contrast will always possess superior noise performance since the lowest noise transistors can be picked for the first amplification stage. The input matching network can also be tailored for the specific transistor, allowing a very good low noise impedance match to be achieved. The MIC approach can also benefit from post manufacture tuning since the length and number of bond wires can be modified as required.

MIC based amplifiers can also be tested with several different matching networks, therefore allowing the prototype amplifier to be optimised and re-designed. Whereas, the integrated nature of MMICs and the design constraints imposed by the manufacturers results in a compromised design. The high cost of a wafer run also limits the possibilities of optimising the design, the designer is also limited in the level of feedback from cryogenic testing that can be implemented in to the design. Should a fault develop with a component, it is also relatively straight forward to replace it in a MIC design.

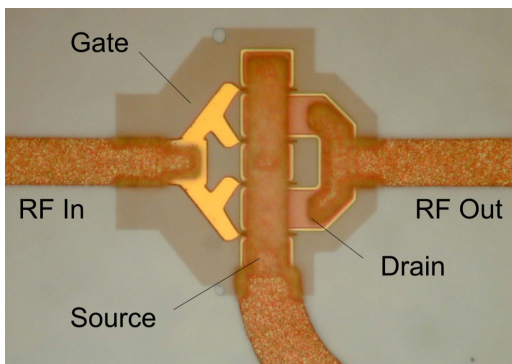
These advantages and disadvantages are summarised in table 4.3

Characteristic	MIC	MMIC
Noise Temperature	Minimum	High loss tangent of the substrate leads to substantial loss. Good but impossible to optimise
Cost	Expensive in terms of labour	High initial cost, but individually cheap
Mass Production	~10s	~1000s
Repeatability	No two LNAs will be the same	Good repeatability
Repair	Damaged components can be replaced	The entire MMIC must be replaced
Design	Plenty of scope to develop prototypes	Very dependent on good computer aided design
Tuning	Bond wires allow some fine tuning	Not possible

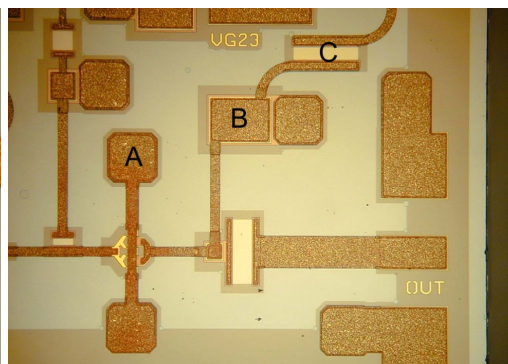
Table 4.3: The advantages and disadvantages of MICs and MMICs.



(a) Ka-Band MMIC



(b) A MMIC's Transistor



(c) Close Up

Figure 4.1.5: Ka-band MMIC based LNA supplied to JBO by T. Gaier at JPL Pasadena. A is a via, B is a capacitor and C is a resistor.

4.2 T+MMIC LNA

From table 4.3 it is clear that ease of manufacture and the repeatability of performance make MMIC based LNAs the obvious option for future CMB observatories, with their large number of receivers. MICs however still offer superior noise performance to MMICs. Therefore the possibility of unifying the two technologies was investigated. This was to be achieved through the use of a very low noise discrete transistor which would allow the design to be optimised for low noise performance through prototyping and tuning, whilst a MMIC with its simplicity of assembly would provide the bulk of the gain.

A similar idea has already been explored at C-band [131] where the MMIC's initial input matching network was removed and fabricated as a discrete element. In this instance the act of integrating the input network on to the MMIC was found to be contributing several degrees more to the noise temperature of the amplifier than for the off chip case. The T+MMIC LNA takes this idea a stage further with removal of the entire first stage, this approach should also avoid the need to develop a special MMIC for the amplifier.

4.2.1 Theoretical Background

The Cascaded Network

It has long been known that the noise temperature of a cascaded system is dominated by both the noise temperature (T_1) and the gain (G_1) of the first component, this can be seen by considering the noise power emanating from initially the first stage of a cascaded system (4.2.2) and then the noise power emanating from the first two stages of the cascaded system (4.2.3). This allows us to write that the cascaded noise N_{cas} for any system can be given by (4.2.4), where T_{cas} is the overall noise temperature and (T_n) is given by the Friss equation (4.2.5) [132].

$$N_{in} = kT_0B \quad (4.2.1)$$

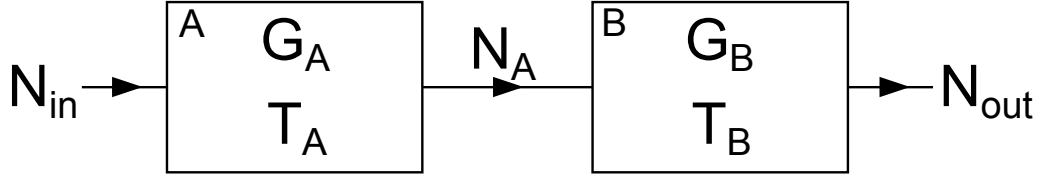


Figure 4.2.1: A cascaded system comprising two sub-systems A and B with gain G_A and G_B and equivalent noise temperatures T_A and T_B . N_{in} is given by 4.2.1

$$N_A = G_A k T_0 B + G_A k T_A B \quad (4.2.2)$$

$$\begin{aligned} N_{out} &= G_A G_B k T_0 B + G_A G_B k T_A B + G_B k T_B B \\ &= G_A G_B k B \left(T_0 + T_A + \frac{T_B}{G_A} \right) \\ &= G_A G_B k B (T_0 + T_{cas}) \end{aligned} \quad (4.2.3)$$

$$T_{cas} = T_A + \frac{T_B}{G_A} \quad (4.2.4)$$

$$T_n = T_1 + \frac{T_2}{G_1} + \frac{T_3}{G_1 G_2} + \dots \quad (4.2.5)$$

The Matching Network

Pospieszalski [104] has also shown that the minimum noise (T_{min}) temperature of any linear two-port device is given by (4.2.6), where T_0 is the standard temperature (290 K), Z_s is the source impedance, Z_{opt} is the optimum source impedance, R_s is the source resistance, R_{opt} is the optimum source resistance and N is given by (2.7.5).

$$T_n = T_{min} + N T_0 \frac{|Z_s - Z_{opt}|^2}{R_s R_{opt}} \quad (4.2.6)$$

(4.2.6) illustrates that it should be possible to present to a device an input impedance that will result in T_n being equal T_{min} , and this is what LNA designers aim to do when they design a transistor's input matching network. Therefore the basis behind the T+MMIC is twofold; through the use of an off chip matching network and a discrete transistor it

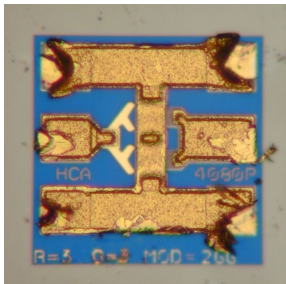
should be possible to not only match the transistor for minimum noise, but also to use transistor's gain to suppress the noise of the following MMIC.

4.2.2 The Transistor and the MMIC

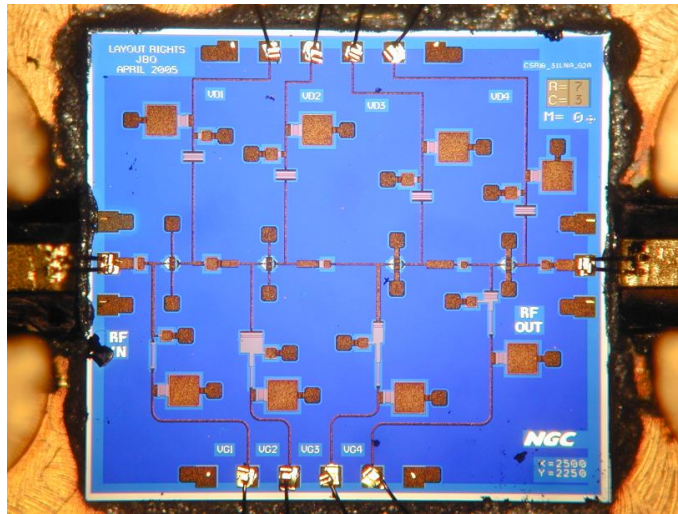
The chosen transistor (figure 4.2.2a) was a $4 \times 20 \mu\text{m}$, 100 nm gate length InP HEMT, that was one of a batch that were originally supplied to the Jodrell Bank Observatory by Nasa's Jet Propulsion Laboratory in Pasadena for use in the European Space Agency's Planck project. This particular transistor was fabricated as part of the Cryogenic HEMT Optimization Program (CHOP) [133], and originates from wafer run 3. Despite being fabricated over a decade ago Cryo-3 transistors still represent the state of the art in terms of noise performance and papers discussing their properties are still being published [134].

This transistor used in the T+MMIC LNA (4080-091) is similar to although not identical to the ones that were used in the Planck LNAs (4080-040), which possessed a slightly thinner passivation layer [135]. Despite this however the performance of the LNA should still be comparable to that of the Planck LNAs.

The MMIC (figure 4.2.2b) was originally developed as part of the European Commission's FARADAY project [136]. These LNAs were developed for radio astronomy and the MMIC possesses a reasonably good cryogenic noise temperature, typically around 20 K (rising to around 190 K at room temperature) and a gain in excess of 40 dB across its 26 to 36 GHz operating band. The FARADAY MMICs were fabricated on InP by Northrop Grumman Space Technologies (NGST) and they consist of four $4 \times 30 \mu\text{m}$ gate width, 100 nm gate length transistors.



(a) Cryo-3 Transistor



(b) Faraday MMIC

Figure 4.2.2: The active devices: (a) a Cryo-3 transistor, (b) a FARADAY MMIC LNA. (Note: not to the same scale).

4.2.3 The LNA Module

Module Design

The T+MMIC LNA (figure 4.2.3) module is responsible for housing the transistor and the MMIC. It is a merger of two existing JBO designed LNA modules. The transistor section is based around the first stage of the Planck 30 GHz front end LFI LNA, and the MMIC section is based on a MMIC test module (known as QUIJOTE 1.3) that was developed as part of the QU-Instrument-JOint-Tenerife Experiment (QUIJOTE) [137].

This approach enabled the use of the existing Planck Cryo-3 input matching network, which avoided the need for a complex re-design of the module and the purchase of new matching networks. This did however restrict the operating bandwidth of the amplifier to 27-33 GHz. Also; the need to incorporate the transistor's bias circuitry in to the module body resulted in a rather long (~ 7 mm) piece of microstrip being required to connect the transistor to the MMIC. The internal components are connected to the outside world via a broadband microstrip to waveguide probe transition. The amplifier's biasing is supplied

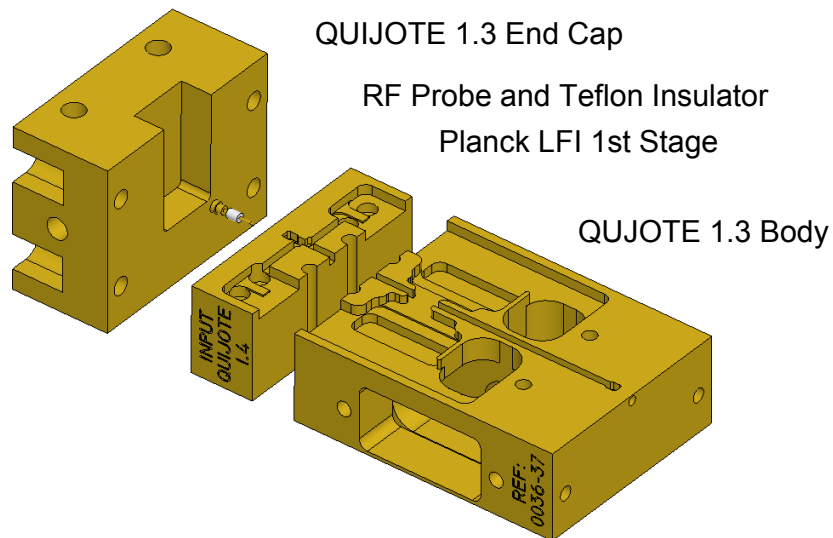


Figure 4.2.3: Computer aided design image of the T+MMIC LNA's module, the input waveguide and input waveguide to microstrip transition. CAD image courtesy of A Gal-tress.

via a 15-pin micro-D connector with independent gate and drain biasing available on each stage. The pin out for the micro-D connector is shown in figure 4.2.4 and table 4.4.

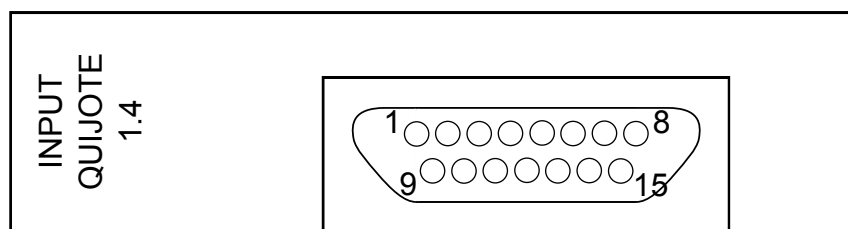


Figure 4.2.4: T+MMIC module pin identification.

Pin	Connection	Pin	Connection
1	Gate 1	9	Ground
2	Drain 1	10	Collector
3	Gate 2	11	Base
4	Drain 2	12	Spare
5	Gate 3	13	Spare
6	Drain 3	14	Drain 5
7	Gate 3	15	Gate 5
8	Drain 3		

Table 4.4: The T+MMIC pin outs. A temperature monitoring diode is installed on pins 10 and 11.

The RF Circuit

The layout of the prototype module can be seen in figure 4.2.5, and the assembled module can be seen in figure 4.2.6. The microstrip lines are gold plated and are fabricated on a $76\mu\text{m}$ Polyflon Cufion substrate, which has an electrical permittivity and a dielectric loss tangent of 2.05 and 0.00045 respectively [126]. A schematic of the T+MMIC LNA is shown in figure 4.2.5, the widths and lengths of the transmission lines are given in table 4.5.

TL	Width (mm)	Impedance Ω	Length (mm)
1	0.21	50	1.05
2	0.64	27	0.85
3	0.21	50	7.20
4	0.21	50	30.0

Table 4.5: The widths and lengths of the T+MMIC LNA's microstrip lines.

The LNA was assembled by hand by E. Blackhurst at the JBO and an image of the assembled LNA can be seen in figure 4.2.6.

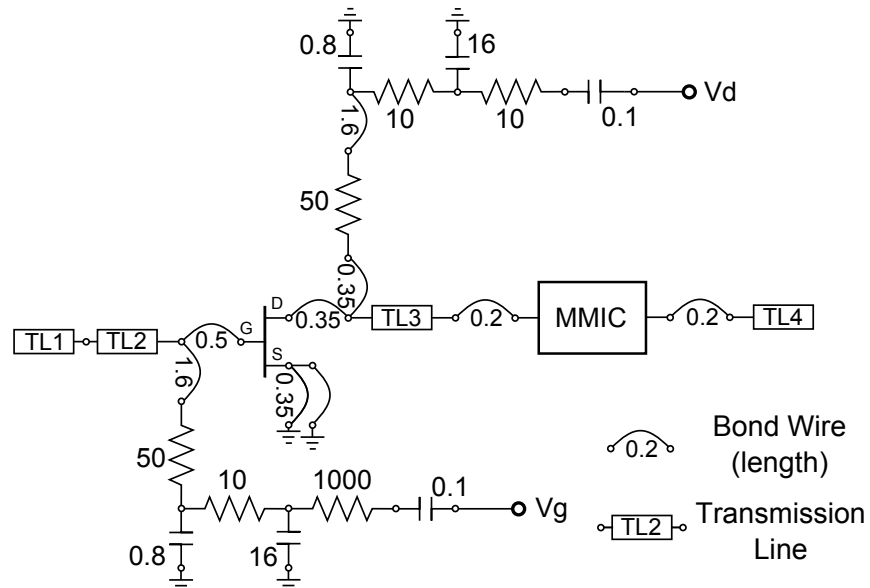


Figure 4.2.5: LNA RF circuit layout. Resistances and capacitances are in Ω and pF respectively, bond wire lengths are in mm.

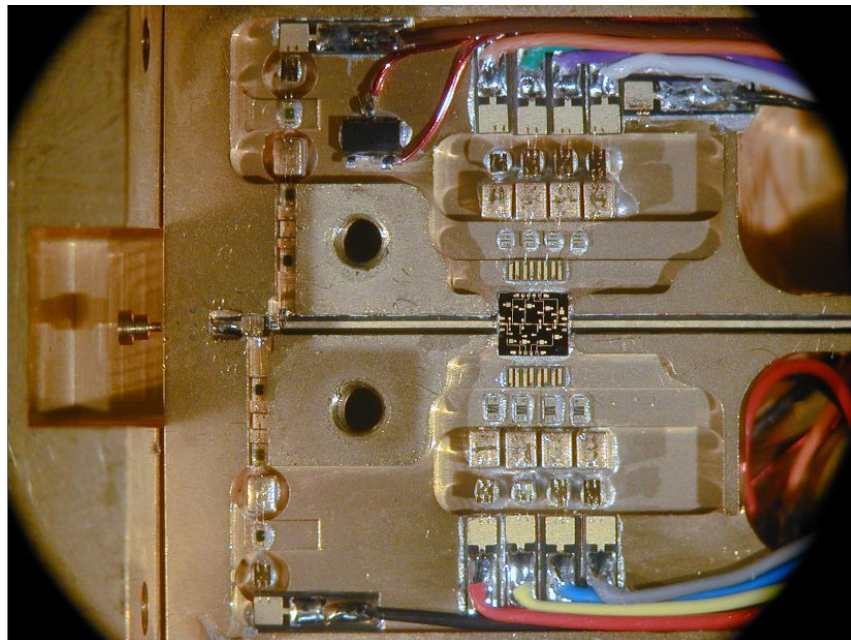


Figure 4.2.6: The assembled LNA. From left to right: probe, input matching network, gate bias, transistor, drain bias, 50Ω microstrip line, MMIC, 50Ω output transmission line.

4.2.4 Theoretical Noise Performance

Since the Planck amplifier used a Cryo-3 transistor for its first 2 stages we can estimate the average noise temperature of our LNA by considering (4.2.5) and the known average

noise performance of both the Planck amplifier and the MMIC. Assuming that only the first two stages of the Planck amplifier contribute to the noise (from (4.2.5) the third and fourth stages are negligible) it is possible to write the following expression (4.2.7) for the average noise temperature of the Planck amplifier ($T_{Planck} = 8.1$ K), where x and G are the noise temperature and gain (8 dB) of the Cryo-3 respectively.

$$T_{Planck} = x + \frac{x}{G} = 8.1\text{K} \quad (4.2.7)$$

For the T+MMIC LNA the following expression (4.2.8) can also be written, where T_{MMIC} is the average noise temperature of the Faraday MMIC (≈ 20 K).

$$T_{T+MMIC} = x + \frac{T_{MMIC}}{G} \quad (4.2.8)$$

Thus, re-arranging (4.2.7) and (4.2.8) and eliminating x gives the expected noise temperature of our LNA as ≈ 10 K (4.2.9).

$$T_{T+MMIC} = \frac{T_{Planck}}{1 + \frac{1}{G}} + \frac{T_{MMIC}}{G} \approx 10\text{K} \quad (4.2.9)$$

4.3 Modeling

The behaviour of the T+MMIC LNA can be modelled through the combined use of two pieces of computer aided design software. Agilent's Advanced Design System (ADS) version 2009 update 1 [138], which is an RF circuit design and simulation software and HFSS. ADS is used to simulate the RF circuit and to perform the de-embedding calculations. The input waveguides and the microstrip to waveguide transitions are modelled using HFSS.

To effectively model the LNA several pieces of information are required:

- The equivalent circuit parameters for the Cryo-3 transistor.

- The Faraday MMIC's S parameters.
- Details of the Faraday MMIC's noise behaviour.
- S parameters for the input and output microwave to waveguide transitions.
- The dimensions of the microstrip.
- the RF-circuit layout.

4.3.1 The Equivalent Circuit Parameters

The procedure for extracting the equivalent circuit parameters has been outlined in section 2.5. The equivalent circuit model for the Cryo-3 transistor was measured as part of the Planck project [139]. For the room temperature simulations only the transconductance, and the Pospieszalski equivalent noise temperatures are assumed to change, with the transconductance being $\sim 20\%$ higher in the cryogenic case [134].

		8 K	290 K
Bias	Vd	0.9 V	1.2 V
	Ids	2 mA	6 mA
Noise	Ta	8 K	290 K
	Tg	8 K	290 K
	Td	400 K	1500 K
Gain	Gm	80 mS	67 mS

Table 4.6: Cryo-3 temperature dependent equivalent circuit parameters.

It is necessary to modify the equivalent circuit shown in figure 2.5.1 (section 2.5) in order to make it compatible with ADS. Figure 4.3.1 shows a suitable design that was developed by Pospieszalski [139]. This design includes a special modification made by Pospieszalski, whereby the source inductance is replaced with ideal transmission lines, these are used to represent the source bond pads.

Extrinsic Parameters		Intrinsic Parameters	
R _g	1 Ω	C _{gs}	52 fF
R _d	5 Ω	C _{gd}	24 fF
R _s	2.2 Ω	C _{ds}	10 ff
C _{pg}	4.6 fF	R _{ds}	135 Ω
C _{pg}	4.6 fF	R _{gs}	4 Ω
C _{pd}	12 fF	τ	0.6 psec
C _{pd}	4.6 fF		
L _g	9 pH		
L _d	16 pH		

Table 4.7: Cryo-3 extrinsic and intrinsic equivalent circuit parameters.

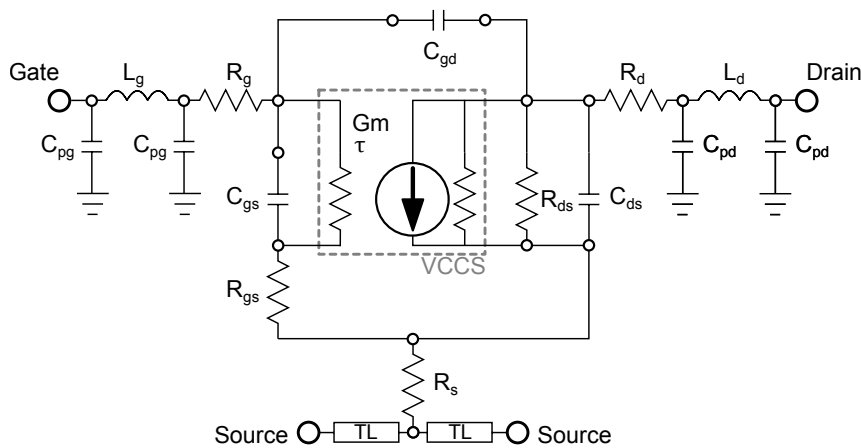


Figure 4.3.1: A transistor equivalent circuit, suitable for use in Agilent Advanced Design system. Developed by M. Pospieszalski [135].

4.3.2 The Faraday MMIC’s S Parameters

To help facilitate an overall model of the T+MMIC LNA the Faraday MMICs S parameters (section 2.1.2) are required to be known.

The MMICs S parameters can be measured in one of two ways, either discretely on a suitable probe station or in situ within a test module. This latter approach was used with the S parameters being measured on an Agilent Technology’s Vector-Network-Analyser (VNA).

De-embedding

Due to the MMIC being situated within a reference module it was necessary to de-embed the MMIC's S parameters from those of the test fixture, in this case the input and output waveguides, microstrips and the respective transitions between them. The set up is illustrated in the form of a signal flow graph in figure 4.3.2.

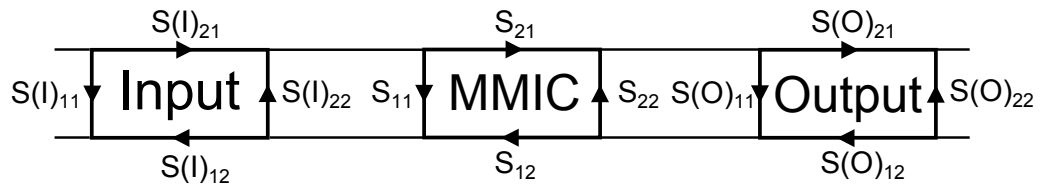


Figure 4.3.2: Signal flow diagram graphically illustrating the S parameters of the MMIC and the input and output fixtures.

To de-embed the MMIC's S parameters, S parameter data is required for the overall system and the input and output sections. This data must be converted to the equivalent scattering transfer parameters (T parameters) (4.3.1).

$$\begin{bmatrix} T_{11} & T_{12} \\ T_{21} & T_{22} \end{bmatrix} = \frac{1}{S_{21}} \begin{bmatrix} S_{12}S_{21} - S_{11}S_{22} & S_{11} \\ -S_{22} & 1 \end{bmatrix} \quad (4.3.1)$$

The T-parameters can then be used to remove the effects of the input and output from the S parameter data. T Parameters like S parameters can be expressed as a matrix, which is given by (4.3.2).

$$\begin{bmatrix} T \end{bmatrix} = \begin{bmatrix} T_{11} & T_{12} \\ T_{21} & T_{22} \end{bmatrix} \quad (4.3.2)$$

The transfer matrix has the property that when multiplied by its inverse the result is an identity matrix, shown (4.3.3).

$$\begin{bmatrix} T \end{bmatrix} \begin{bmatrix} T \end{bmatrix}^{-1} = \begin{bmatrix} 1 & 0 \\ 0 & 1 \end{bmatrix} \quad (4.3.3)$$

Since the reference module is essentially a network of cascaded components (figure 4.3.2), it is possible to write what we actually measure in terms of a $[T]$ matrix (4.3.4).

$$\begin{bmatrix} T_{measured} \end{bmatrix} = \begin{bmatrix} T_I \end{bmatrix} \begin{bmatrix} T_{MMIC} \end{bmatrix} \begin{bmatrix} T_O \end{bmatrix} \quad (4.3.4)$$

Therefore (4.3.3) and (4.3.4) can then be used to to obtain $[T_{MMIC}]$ (4.3.5), which by using (4.3.1) can be used to obtain the MMIC's S parameters.

$$\begin{bmatrix} T_I \end{bmatrix}^{-1} \begin{bmatrix} T_I \end{bmatrix} \begin{bmatrix} T_{MMIC} \end{bmatrix} \begin{bmatrix} T_O \end{bmatrix} \begin{bmatrix} T_O \end{bmatrix}^{-1} = \begin{bmatrix} T_{MMIC} \end{bmatrix} \quad (4.3.5)$$

Further details of the de-embedding process can be found in the relevant Agilent application note [140]

To facilitate the de-embedding of the Faraday MMIC, S parameter simulations of the input and output parts of the module were produced in HFSS. The model of the input probe can be seen in figures 4.3.3 and 4.3.4 and the performance of the input and output probes can be seen in figure 4.3.5. The module was modelled as brass, whilst the probe was modelled as gold. A wave-port was used to simulate an input / output to the waveguide, whilst a 50Ω lumped-port was used for the input / output of the microstrip, vacuum is used as the inter-filling medium.

The simulated performance can then be used in the following ADS circuit (figure 4.3.6) to extract the Faraday MMIC's S Parameters from those measured for the combined module and MMIC.

4.3.3 Passive Components

Capacitors and Resistors

Ideally the capacitors and resistors that make up the transistor's bias chains would be modelled in ADS as lumped components. These would not only include their respective

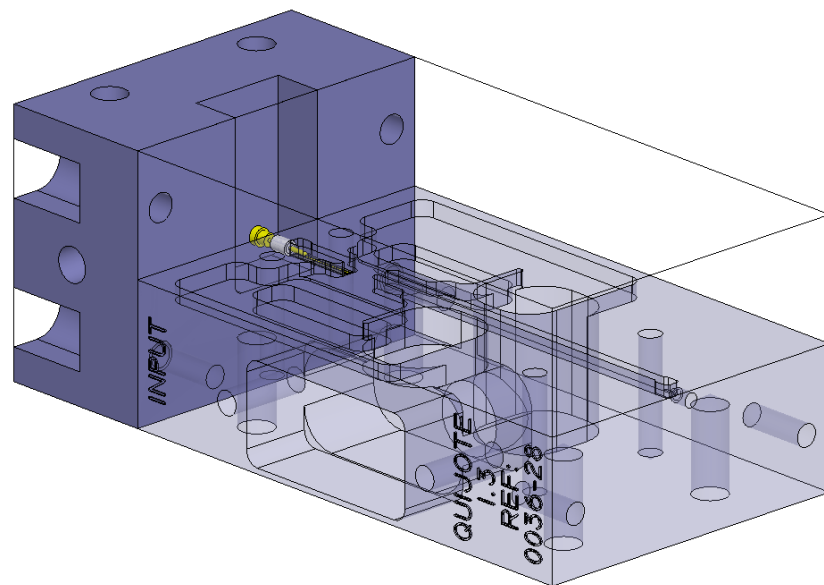


Figure 4.3.3: HFSS model of the QUIJOTE 1.3 input probe.

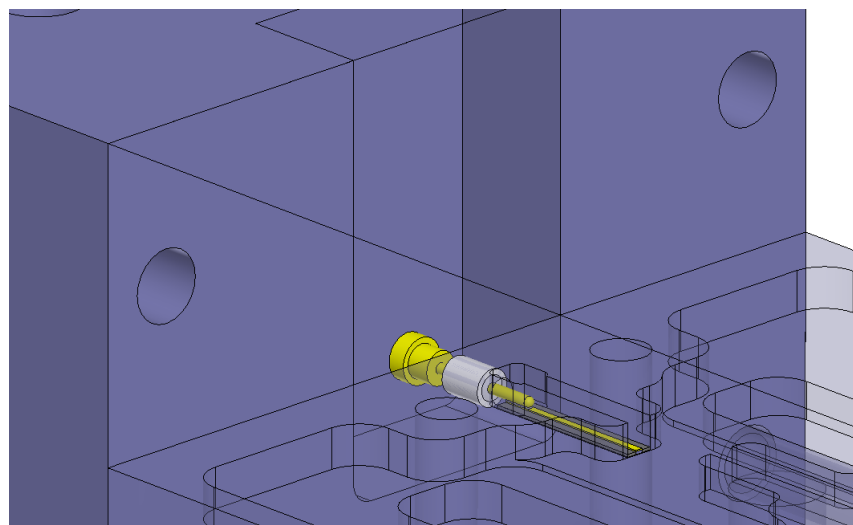


Figure 4.3.4: Close up of the waveguide to microstrip probe transition, the probe and microstrip are in yellow, the cuffon is coloured dark grey, and the white cylinder is the PTFE insulator.

capacitance and resistance, but also their parasitic equivalent series inductance and in the case of the capacitors their equivalent series resistance. However, as these details were not available the resistors and capacitors were modelled in using just ideal components.

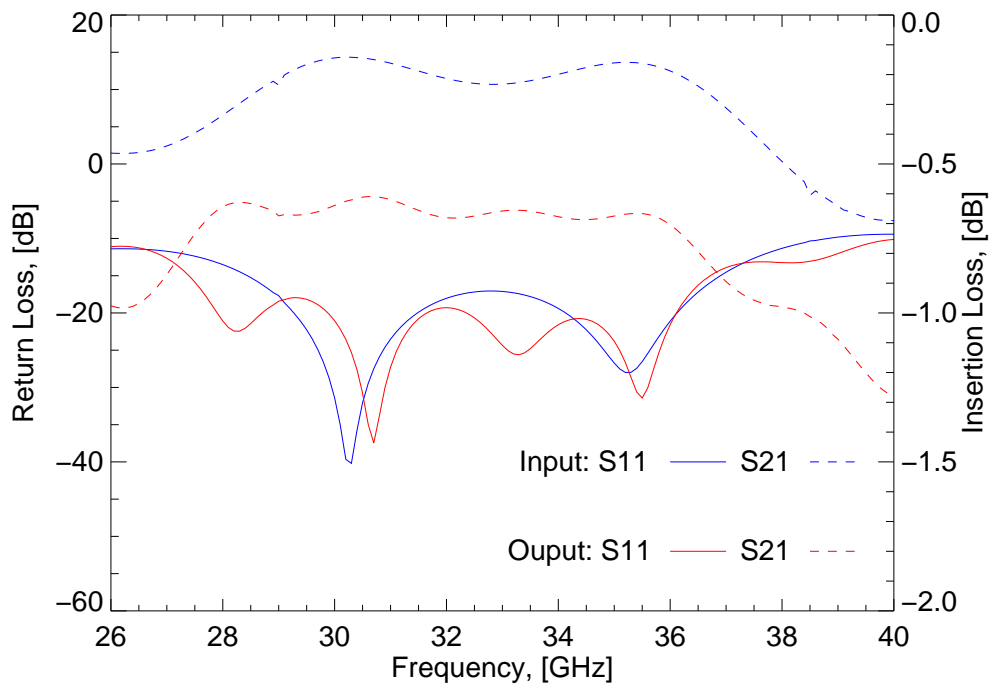


Figure 4.3.5: The simulated performance of the QUIJOTE module input and output probes. The dashed lines show the insertion loss and the solid lines show the return loss.

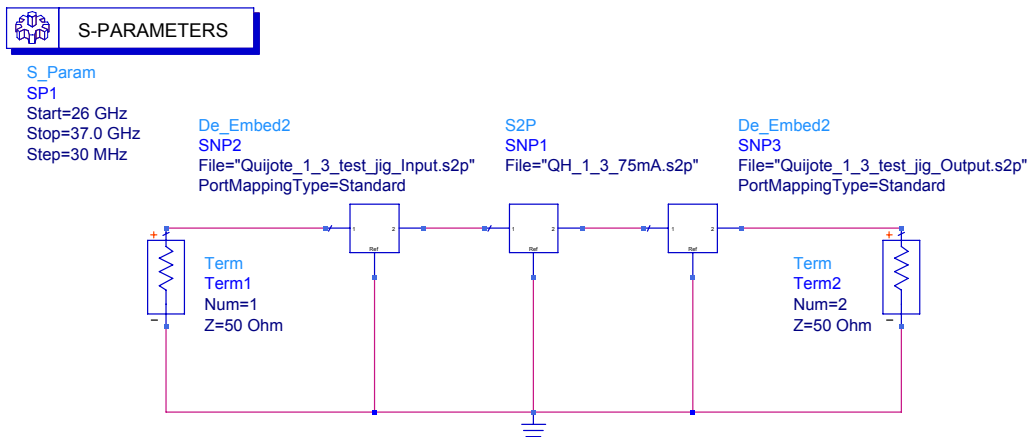


Figure 4.3.6: The ADS de-embedding circuit.

Bond Wires

At frequencies of a few GHz bond wires can be modelled by one of two techniques. One technique is to use ideal inductors, where to a good approximation the inductance

of a wire in free space (4.3.6) can be used to estimate the wire's inductance²⁶ Another technique is to use the bond wire model provided by ADS and although ADS allows the user to define the wire's shape, the model doesn't take into account the capacitance that exists between the wire and other conductors in the vicinity, nor does it take into effect the capacitance that exists between the ground plane and the wire. At frequencies of a few GHz these effects are negligible but at higher frequencies they have the effect of making the bond wire's behaviour more akin to that of a transmission line than an inductor, as can be seen by figure 4.3.7b.

$$L = \frac{l}{5} (\ln(4l/d) - 0.75) \quad (4.3.6)$$

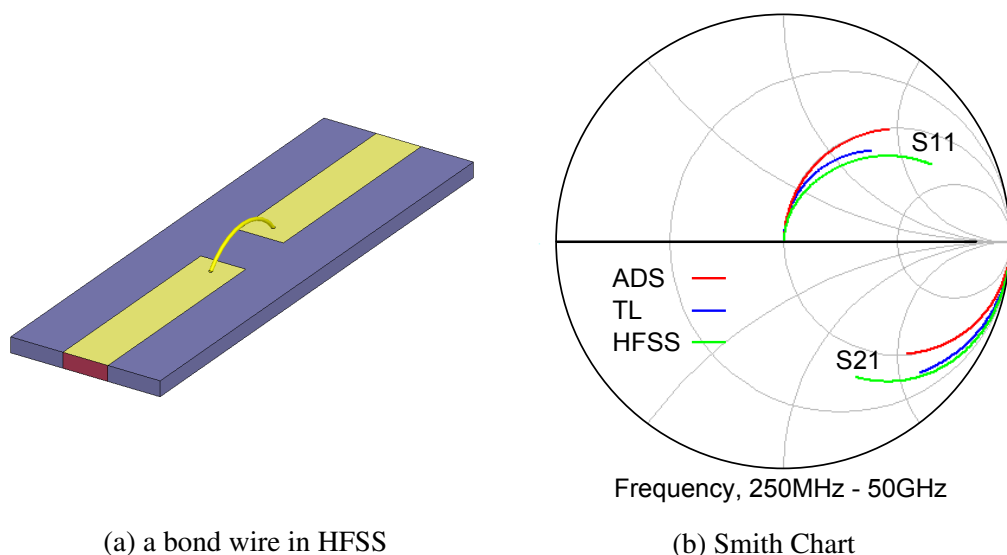


Figure 4.3.7: The transmission line like behaviour of a bond wire. (a) A simple HFSS simulation of a 500 μm bond wire. (b) The behaviour of a HFSS bond wire, an ideal transmission line and the ADS bond wire component. The ADS wire is moving along a line of constant resistance, just like an ideal inductor.

Since the ideal transmission line represents a good approximation to the behaviour of the bond wire at higher frequencies, 150 Ω ideal transmission lines are used to model the effects of the bond wires, an additional 20% is included on top of the linear length to ac-

²⁶the length of the wire should be the linear length plus 10 – 20% to take into account the additional length caused by the curvature of the wire.

count for the curvature of the wire. This particular approach was used in the development of the Planck amplifiers by M. Pospieszalski [139].

4.3.4 The Model

The full ADS schematic of the 8 K model is shown in figure 4.3.8. The S-parameter performance can be determined directly from the model. However, due to the lack of MMIC noise parameters the noise performance was determined through the use of (4.2.5) and a separate model of just the transistor stage and the output transmission line (TL3). The noise and gain of this section are then used as T_1 and G_1 in (4.2.5) respectively.

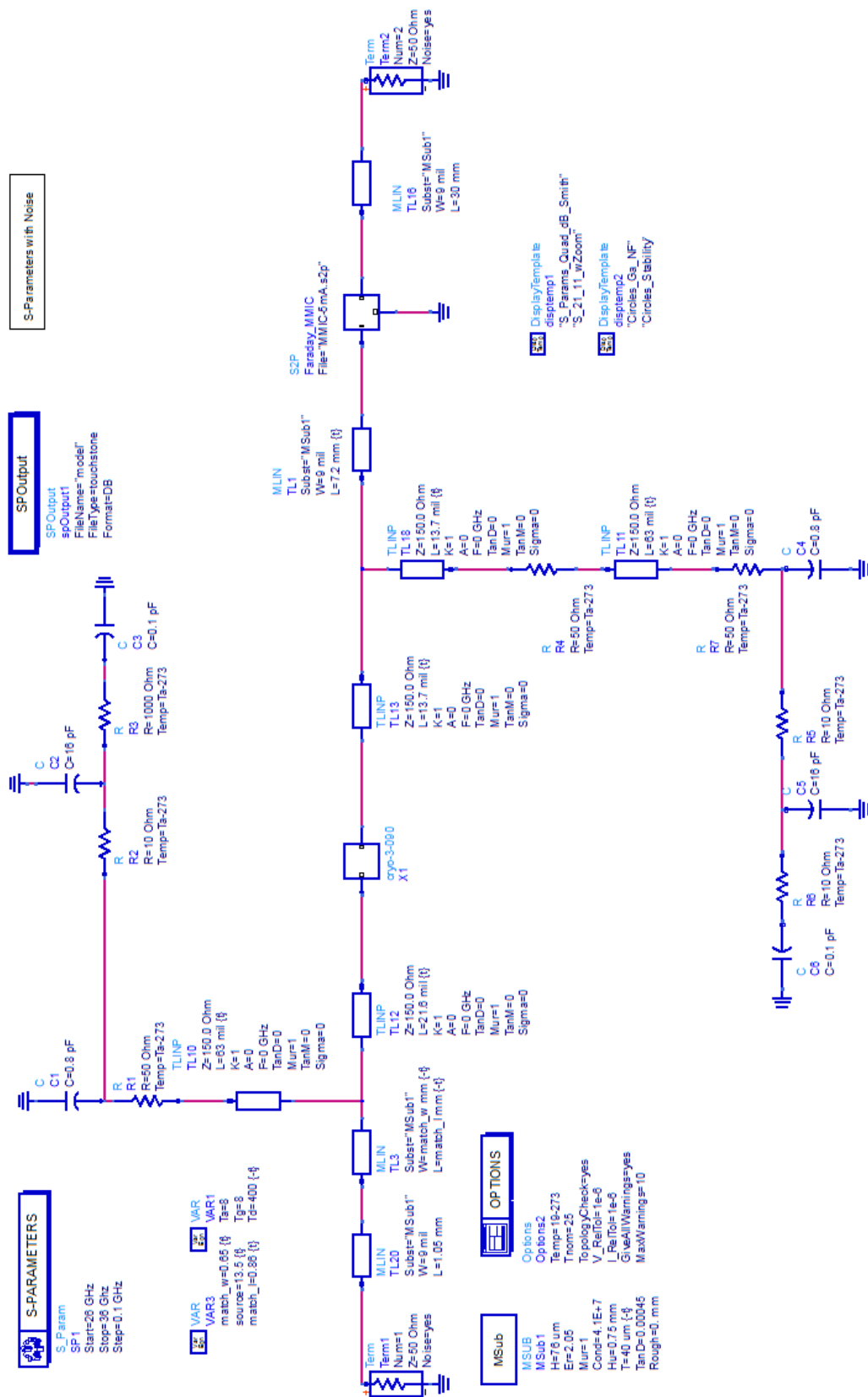


Figure 4.3.8: The full ADS 8 K model.

4.4 Performance

The LNAs were measured using the test set up already described in section 3.3. For the room temperature measurements an Agilent R347B noise source was used to provide two different levels of noise to the LNA's input. Whilst the cryogenic measurements used the same hot cold load technique that was discussed in Chapter 3. The T+MMIC LNA was tested at both room temperature and at cryogenic temperatures and the results were compared with a MMIC only test LNA, the previously mentioned QUIJOTE 1.3 amplifier (section 3.5.2).

4.4.1 27-33 GHz Performance

The performance of the T+MMIC LNA across its optimal frequency band at both room temperature and 8 K can be seen in figures 4.4.1 and 4.4.2. At both room and cryogenic temperatures the improvement in the noise temperature for the T+MMIC over the MMIC only amplifier is quite dramatic with an $\sim 25\%$ improvement across the lower half of the band at room temperature and an $\sim 33\%$ improvement at 8 K. As of 2013 this latter case represents the lowest ever reported noise temperature for a Ka-band MMIC LNA, and whilst some of this improvement has arisen from the lower operating temperature it is still substantially better than the MMIC only case. This noise temperature is comparable to the average noise temperature of the Planck amplifier [124], which indicates that the transistor is indeed dominating the noise temperature as expected. The difference in performance improvement between the room temperature and 8 K cases is likely due to the use of different transistors in the two devices and their responses to cooling.

The behaviour of T+MMIC amplifier's gain is slightly unexpected, since you would expect the difference in gain between the T+MMIC and MMIC only amplifier to be greater at lower frequencies where the gain of the Cryo-3 (see figure 4.4.4) is greatest, than at higher frequencies. However, this is not the case with the largest difference in gain

being at ~ 31 GHz. This could be due to a degradation in the performance of the MMIC LNA (this analysis assumes that the MMICs are identical), the MMIC only modules are several years older than the T+MMIC module or the T+MMIC may be behaving in a more complex way than expected.

An earlier version of this work was presented at the European Microwave Week Conference 2012 in Amsterdam [122], at which the author also presented a poster.

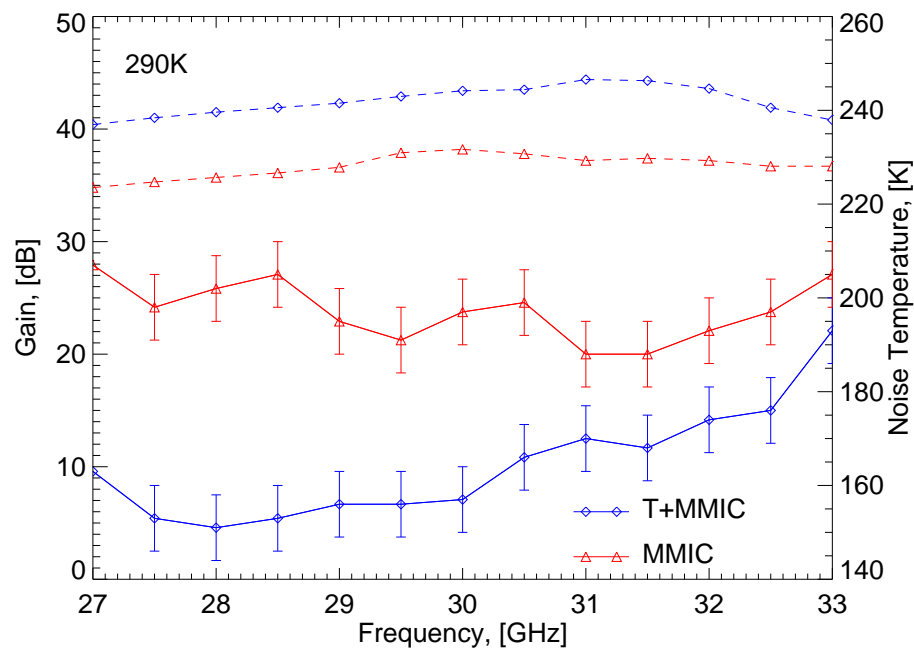


Figure 4.4.1: The room temperature measured noise and gain performance of the T+MMIC LNA with respect to a Faraday MMIC only amplifier.

4.4.2 26-36 GHz (MMIC band) Performance

Clearly the performance of the LNA across its optimal band is very good, however as can be seen in figures 4.4.3 and 4.4.4 the performance outside of the design band is not as good. These figures also illustrate the predicted performance from the model.

The models confirm that the amplifier is behaving as expected from the Friss equation (4.2.5). Fig. 4.4.4 shows that within the intended operating bandwidth (27-33 GHz)

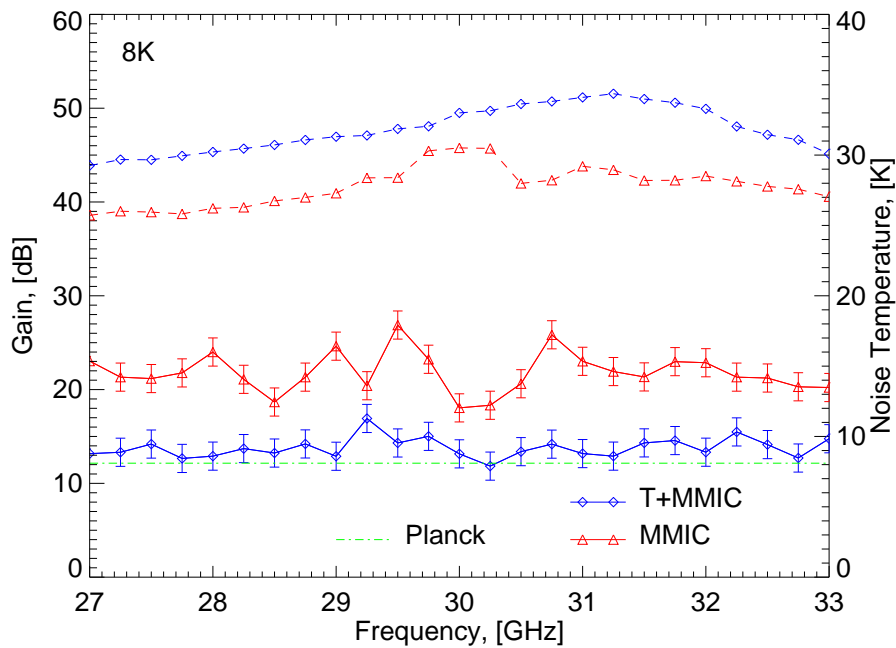


Figure 4.4.2: The cryogenic measured noise and gain performance of the T+MMIC LNA at 8 K physical temperature with respect to a Faraday MMIC only amplifier.

the noise temperature of the T+MMIC LNA sits just above the noise temperature of the transistor (first stage), with the gain suppressing the noise contribution of the MMIC. Outside this band however, once the gain offered by the first stage reduces, the noise of the MMIC becomes more significant and the noise temperature of the T+MMIC LNA drifts away from the noise temperature of the transistor, becoming as can be seen in figure 4.4.3 equivalent to that of the MMIC.

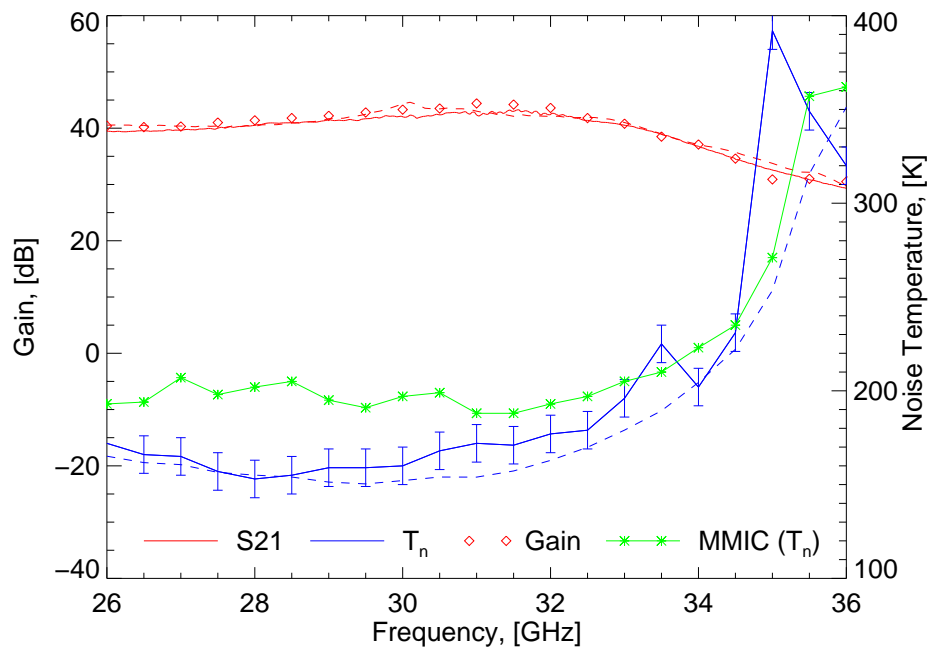


Figure 4.4.3: The modelled (dashed) and measured (solid lines) 290 K physical temperature performance of the T+MMIC LNA. The noise temperature of the MMIC only amplifier the gain recorded by NFM for the T+MMIC LNA are also shown.

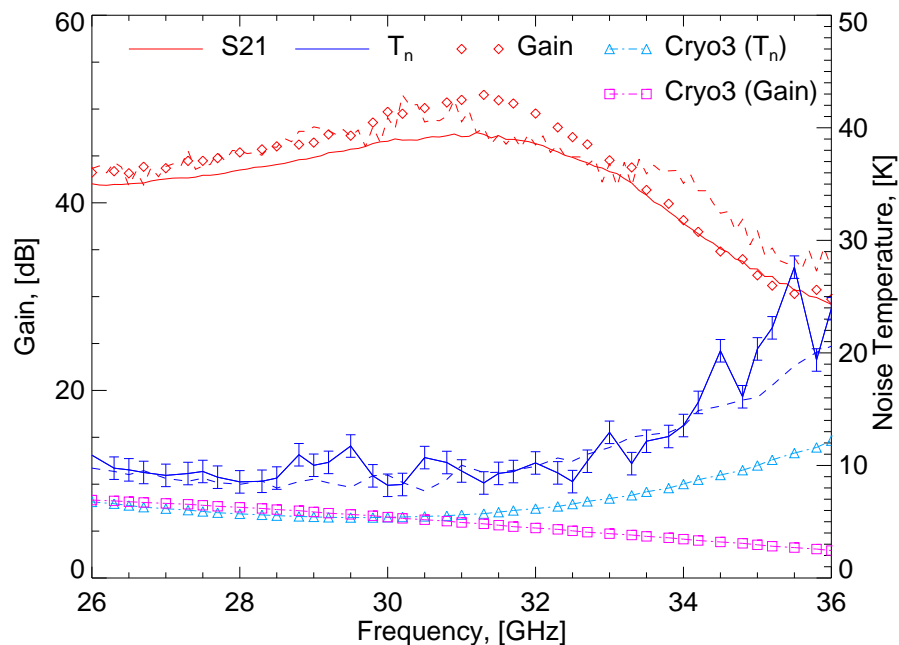


Figure 4.4.4: The modelled (dashed) and measured (solid lines) 8 K physical temperature performance of the T+MMIC LNA. The modelled noise temperature and gain of the transistor is also shown along with the gain recorded by NFM for the T+MMIC LNA.

4.4.3 Stability

An important requirement of amplifier design is that the amplifier is stable, i.e. it should not oscillate. Since the T+MMIC LNA possesses a large amount of gain it is at high risk of instability and therefore its stability was measured. The stability of an amplifier can be determined through S parameter measurements and the amplifier will be unconditionally stable²⁷, provided that it satisfies the Rollet stability condition (4.4.1) and the auxiliary stability condition (4.4.2). The predicted stability at 8 K from the ADS model is shown alongside the calculated stability from the T+MMIC's S Parameters in figure 4.4.5.

$$K = \frac{1 - |S_{1,1}|^2 - |S_{2,2}|^2 + |\Delta|^2}{2|S_{1,2}S_{2,1}|} > 1 \quad (4.4.1)$$

$$|\Delta| = |S_{1,1}S_{2,2} - S_{1,2}S_{2,1}| < 1 \quad (4.4.2)$$

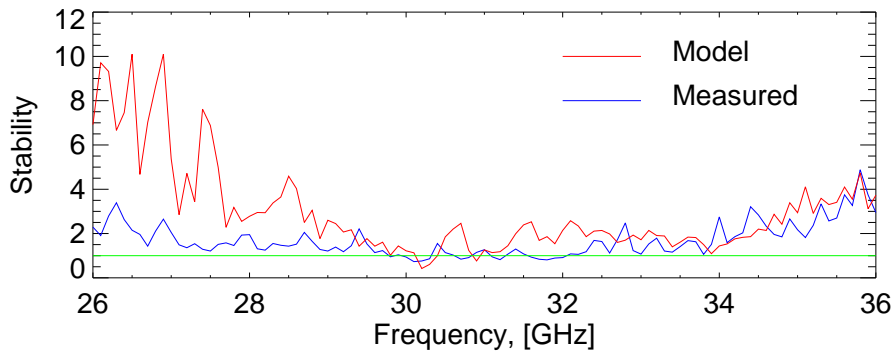


Figure 4.4.5: The Stability of the T+MMIC amplifier at 8 K.

Figure 4.4.5 shows that there is a good match between the predicted and measured stability of the amplifier, but that the amplifier is briefly conditionally stable at several frequency points towards the centre of the band. This may explain why it was observed in testing that the amplifier oscillates in the 20-30 K region. In later measurements this instability was no longer observed and the exact reason for this is unclear, however this

²⁷Stable for all input impedances.

observation of instability presents an interesting discussion point. It is well known that good room temperature performance does not necessarily equate to good cryogenic performance and amplifiers are routinely developed and initially tested at room temperature with good performance being reported, only for considerably more work to be required to make the amplifier work cryogenic-ally. This of course raises the question are LNA designs that would have worked well at cryogenic temperatures being rejected at room temperature. The cryostat used in these experiments presents the possibility of investigating amplifier stability at various temperatures in addition to the usual noise and gain measurements that form part of the development process.

4.5 Discussion

4.5.1 20 K Physical Temperature Performance

In section 4.2.4 using an analogy to the Planck LNA the expected noise temperature of the T+MMIC LNA was estimated as 10 K. The 20-K data (figure 4.5.1) shows that the actual noise temperature is actually slightly higher at 11.4 K. This is likely due to the slight difference between the Cryo-3 transistors used in the Planck amplifiers and the one used in the T+MMIC LNA. The T+MMIC Cryo-3 has a slightly thicker passivation layer and these transistors were found to have a slightly inferior noise performance to the type of Cryo-3 transistors eventually used in Planck [135]. Figure 4.5.1 also shows that the T+MMIC LNA requires the addition cooling to 8 K in order to make it comparable to the 20 K performance of the Planck amplifiers.

4.5.2 Input Matching and Transmission Lines

Owing to the use of the existing Planck architecture (module and biasing network) for the transistor section of the LNA the final bandwidth was always going to be limited to

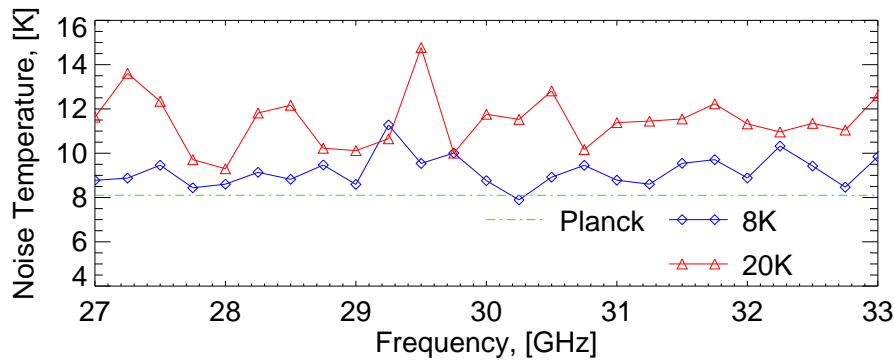


Figure 4.5.1: The noise temperature of the T+MMIC LNA at 19 K and 8 K, compared to the average noise temperature of the Planck amplifiers.

that of the Planck LNA. Clearly in any future design the matching network used for the transistor needs to coincide with the bandwidth of the MMIC. In particular any future design should ensure that the first stage's input matching network takes into account the noise behaviour of the MMIC. For example in the present design the gain of the transistor lowers with frequency, whilst the transistor is configured for minimum noise at 30 GHz and this leads to good noise performance in the lower part of the frequency band where thanks to the high gain of the transistor the MMICs contribution to the overall noise temperature is negligible. However, the performance gets worse at higher frequencies where the transistor's noise is increasing and its gain decreasing. Thus any future design needs to either 'balance' these two effects so that the required performance is achieved or alternatively, the design needs to ensure that the gain and preferably the noise of the transistor are flat across the required frequency band.

The use of Planck architecture also required the use of a long transmission line linking the transistor and the MMIC and ADS simulations show that the gain in particular is very sensitive to the length of this line. This could be due to feedback into the transistor from the MMIC or the lack of an output matching network²⁸ on the transistor. A potential resolution to this problem will be presented in the following chapter.

²⁸This network would transform the out impedance of the transistor to the $50\ \Omega$ of the microstrip line

4.5.3 Applications

One obvious drawback of this technology is the need to develop a new module for the integration of the MMIC and the transistor. A preferred approach would be to mount the transistor into its own module and connect it via waveguide to an existing MMIC-based amplifier module. This combined with the research outlined in Chapter 3 hinting at potential improvements in noise performance with respect to further cooling beyond 20 K makes this approach a potential solution to the problem of cooling a large number of amplifiers. Under such system only the transistor would be cooled to 4 K with the MMIC amplifiers remaining at a higher temperature, which is far easier than attempting to cool all 4 or 5 amplification stages to 4 K. A design for such a system will be explored in the next chapter.

4.6 Conclusion

MMIC LNAs are now the preferred choice for the LNAs required by radio astronomy, but their noise performance is still inferior to that of MIC based LNAs. One possible solution is to use a discrete transistor in front of the MMIC. This chapter has reported on the development of such an LNA, with an average noise temperature of 9.4 K. This is some 4-5 K lower than an equivalent MMIC LNA, representing a near 50% improvement. Cryogenic cooling to 8 K has also resulted in an amplifier that almost matches the noise performance of the lowest-noise Ka-band LNAs so far developed, illustrating that cooling below the typical 15-20 K that is currently used by most radio observatories may prove beneficial. The T+MMIC LNA presented in this chapter also shows the effectiveness of a simple approach to the modeling of such an amplifier, showing that the MMIC can almost be regarded as a “black box” in terms of the amplifier’s development with only the transistor’s equivalent circuit parameters and noise parameters needing to be measured with a probe station. The modelled data also show that we have demonstrated effective

suppression of the (higher) MMIC noise by the lower-noise first-stage transistor, within its operating band.

The work presented in this chapter has been submitted [141] to the IEEE journal *Microwave Theory and Techniques*.

Chapter 5

Future Applications

Chapters 3 and 4 outlined two approaches to enhancing the noise performance of LNAs and whilst each approach had its merits, each approach also had its drawbacks. This chapter outlines the author's preliminary design for an LNA that utilizes the approaches outlined earlier in this thesis.

5.1 Drawbacks to Cooling and the T+MMIC Approach

One particular problem encountered in Chapter 3 was that depending on the power requirements of the LNA it was not always possible to cool the LNA to 4 K or below. Therefore the cooling potential (in terms of absolute temperature) may not be available, especially if this approach were to be applied to a receiver system with many amplifiers.

Chapter 4 showed the potential of using a single low noise transistor to lower the noise temperature of a MMIC LNA but, there were a series of issues associated with the design. The use of a long transmission line to connect the transistor and the MMIC led to issues with the gain, the MMIC is at risk of compression and there are some underlying stability issues.

One potential solution to these problems is to develop a new variant of the T+MMIC

LNA. A design where the transistor and the MMIC are placed within their own discrete modules and connected to one another by waveguide. The single stage transistor amplifier would be cooled to as low as possible, whilst the MMIC section would remain at between 4 and 20 K depending on the level of cooling power available. The basic layout is shown in figure 5.1.1 and figure 5.1.2 shows an impression of the author’s design thoughts for a future test cryostat. Such a cryostat could exploit such an approach to not only investigate the ultra low physical temperature performance of transistors but it could also form the basis for a multi pixel multi frequency receiver.

Owing to the problems with the earlier thermal breaks a new design (figure 5.1.3) is currently being developed by the author and Dr S. Melhuish. To increase rigidity the stainless steel sections have been replaced by carbon fibre rods and these are arranged in the form of a ‘Stuart Platform’. Like the earlier thermal breaks the two waveguide flanges are separated by $0.1 \mu m$.

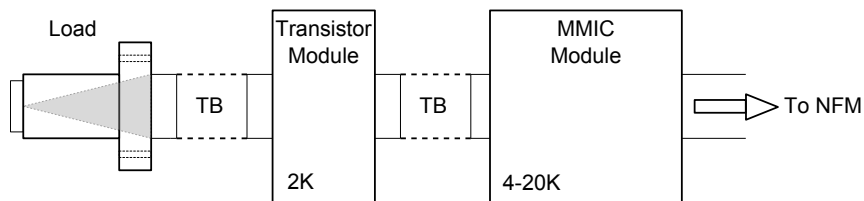


Figure 5.1.1: Proposed layout for the discrete block approach to LNAs. The modules are connected via waveguide and a thermal break would be placed between the load and the transistor module. (TB): Thermal break.

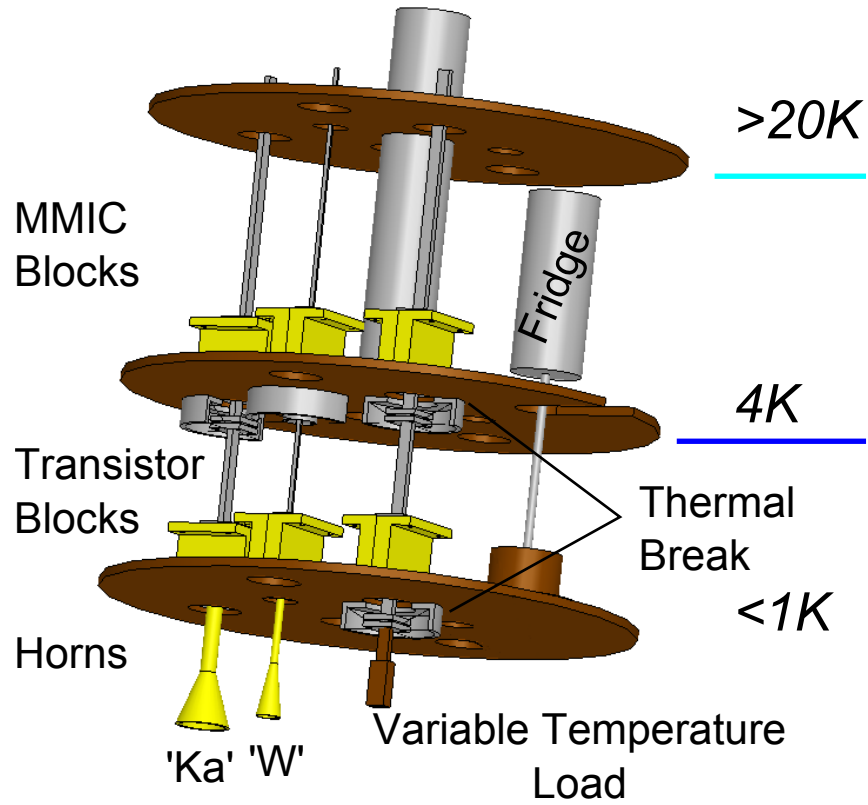


Figure 5.1.2: Future multi-frequency transistor test cryostat.

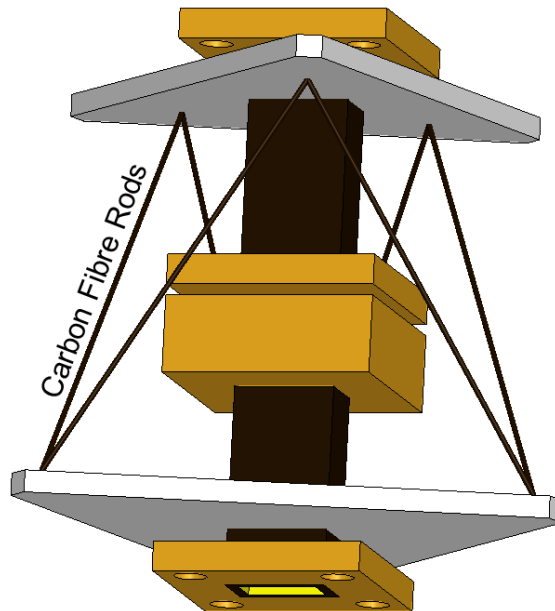


Figure 5.1.3: A next generation thermal break.

5.2 T+MMIC Version 2.0

5.2.1 First Stage Design

In preparation for the manufacture of this cryostat and this LNA the author has carried out preliminary design work in ADS for a single stage transistor amplifier. The chosen transistor is an InP Hughes Laboratories HRL $2 \times 50 \mu\text{m}$ transistor, which JBO acquired in the early phase of the Planck LFI as a potential transistor for the Planck Ka-band amplifiers. Although these transistors were rejected for Planck, their noise performance is only a few Kelvin worse than the Cryo-3 at 20 K (T_{phys}), but as they were unused they are currently available in significant numbers.

The equivalent circuit parameters were measured at room temperature as part of the Planck development project [142] and they are shown in table 5.1. Since these are the room temperature parameters it is assumed that as with the Cryo-3 they remain unchanged on cooling, though this may not be the case and they should be measured cold if possible. For the cryogenic design Gm is increased to 60 mS, T_a and T_g are set to 2 K, whilst T_d is set to 400 K which is consistent with the findings of Pospieszalski [143], and the Planck design work.

In a change from the T+MMIC LNA the RF circuit is designed to be fabricated on a $250 \mu\text{m}$ thick Alumina substrate ($\epsilon_r = 9.5, \delta = 0.0003$). The preliminary ADS design is shown in figure 5.2.1 and the predicted performance at 2 K physical temperature for the single stage amplifier is shown in figure 5.2.2.

Changing to a thicker substrate with a higher ϵ_r also allows the design to take advantage of some other features found in more recent LNAs. The original T+MMIC design utilises an RF feed pin as part of its waveguide to microstrip transition, this amplifier should continue to use waveguide inputs and outputs, but one possible design change worth exploring is to fabricate the probe as part of the substrate [144]. This approach might also allow for the use of an integrated waveguide to microstrip bias tee [145]. The

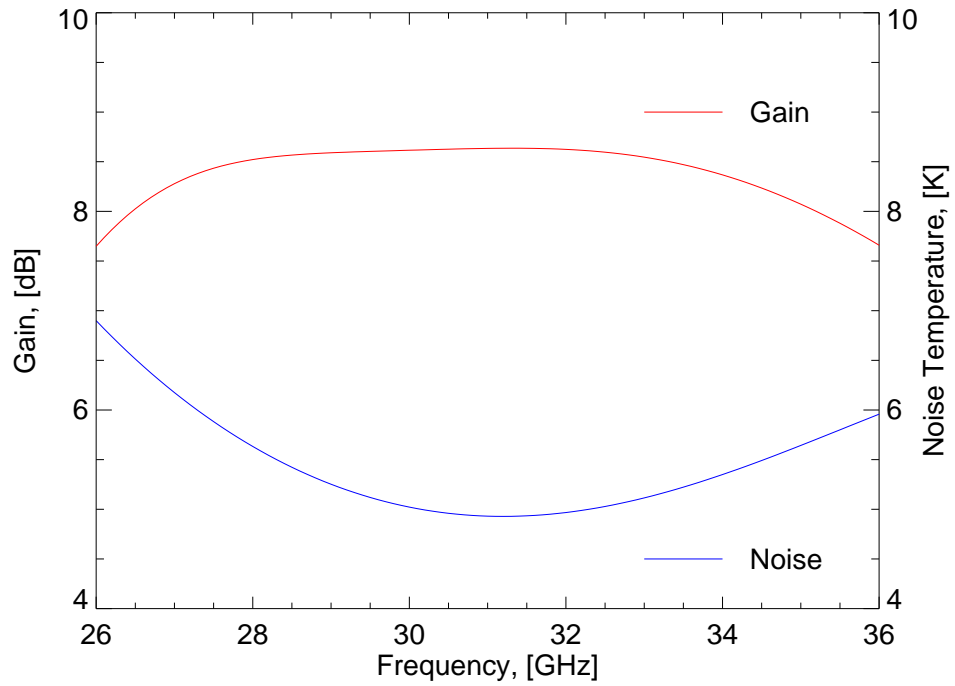
T+MMIC also used long ~ 2 mm bond wires in its drain and gate bias circuits, the use of alumina also allows the length of these wires to be reduced, since they can be fabricated as high impedance microstrip lines, with radial stubs providing additional inductance. These approaches would offer simpler fabrication and make the amplifiers more suitable for mass production.

These techniques may also allow for greater reliability in models of the amplifier, since at present the RF feed pin is bonded to the microstrip by solder and the shape of the solder is difficult to simulate. The profile of the long gate and drain bias wires is also subject to some uncertainty.

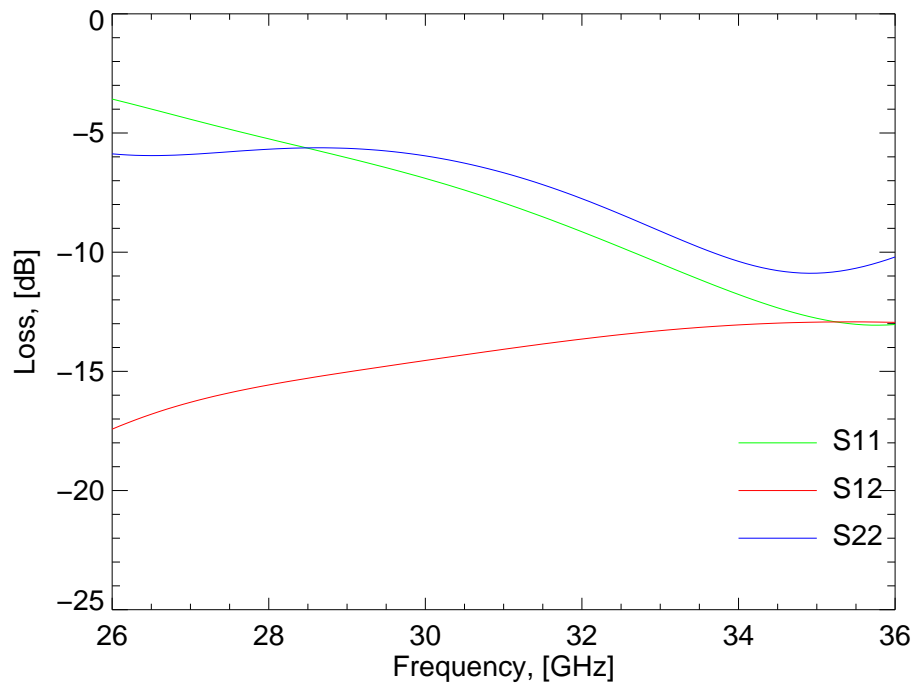
Extrinsic Parameters		Intrinsic Parameters	
Rg	2 Ω	Cgs	40 fF
Rd	10 Ω	Cgd	9 fF
Rs	6.6 Ω	Cds	10 fF
Cpg	10 fF	Rds	190 Ω
Cpd	9 fF	Rgs	2.5 Ω
Lg	10 pH	τ	0.1 psec
Ld	10 pH	Gm	50 mS
Ls	5 pH		

Table 5.1: HRL 2x50 μ m HEMT extrinsic and intrinsic equivalent circuit parameters.

The simulation shows that the design has the potential to offer a noise temperature less than 6 K across most of the 26–36 GHz bandwidth and a fairly flat gain of ~ 8.5 dB for most of the band. Although the design shows promise is still in its early stages and does require some further work; for example ADS shows that the amplifier is only just un-conditionally stable (figure 5.2.3). However, since this design is modular, the stability could be improved by placing an isolator between the transistor and MMIC modules in order to prevent feedback from the MMIC. The low frequency input return loss could also do with some improvement.



(a) Noise and Gain Performance



(b) S Parameters

Figure 5.2.2: Performance of the Single stage HRL $2 \times 50 \mu\text{m}$ HEMT based amplifier at 2 K physical temperature.

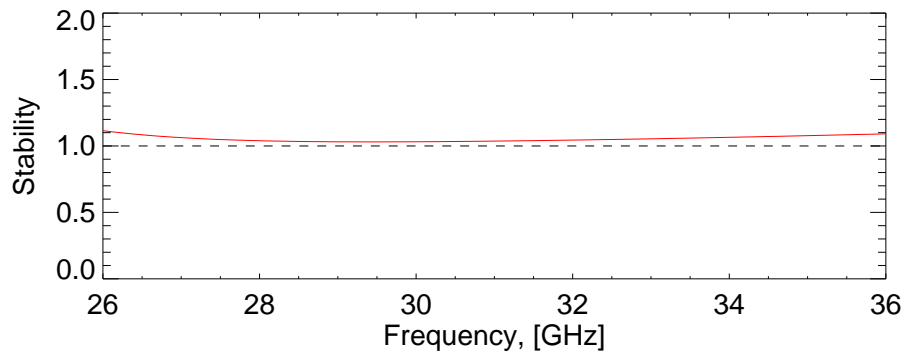


Figure 5.2.3: Performance of the HRL $2 \times 50 \mu\text{m}$ single stage amplifier: stability.

5.3 Potential Performance

As a first approximation, it is possible to combine the predicted performance for the single stage amplifier with the noise and gain performance of the JPL amplifier using the Friss equation (4.2.5). The estimated performance of such an amplifier is shown in figure 5.3.1. For a 26-36 GHz bandwidth the amplifier has a gain in excess of 34 dB and an average noise temperature of 6.8 K which would make this the lowest noise temperature ever reported at Ka-band, surpassing the performance of the Planck amplifiers.

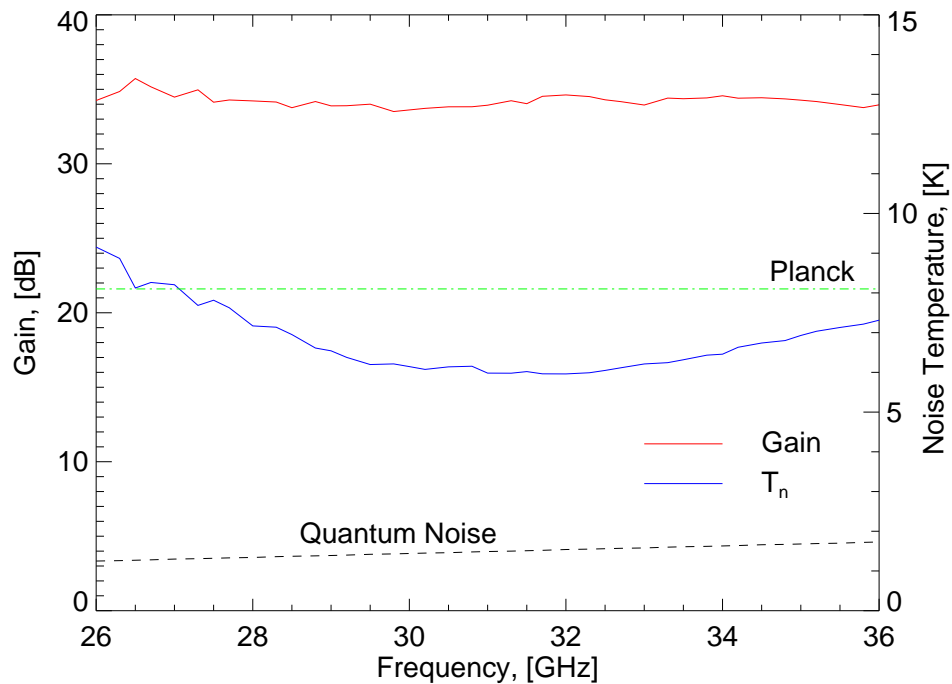


Figure 5.3.1: Potential noise and gain performance of a future Ka-band T+MMIC (discrete block) LNA, compared to the average Planck LFI LNA noise temperature and the quantum noise limit.

This approach could also be developed further through the use of finlines [146], which would allow the MMIC or the transistor to be built into the waveguide itself.

5.4 Drain Temperature Investigation

This design of amplifier could also be used to further investigate the relationship between T_d and T_{phys} , assuming that the equivalent circuit model is known for several drain currents. This could be done by varying the temperature of transistor block, whilst keeping the MMIC at a constant temperature and using its gain to help make the measurements. Measuring the MMIC block's noise contribution would then allow its noise contribution to be removed from the system noise, resulting in the noise temperature of the transistor being known. The Pospieszalski noise equivalent circuit could then be used to further investigate the behaviour of T_d with respect to both drain current and physical temperature.

Chapter 6

Concluding Remarks and the Future

6.1 Conclusion

Chapter 1 illustrated the pivotal role that LNAs have played and continue to play in radio astronomy in general and in developing our understanding of cosmology through studying the CMB in particular. Chapter 1 also showed that despite the considerable amount of knowledge that has been gained from studying the CMB, observations of the CMB's polarisation and in particular the B-mode polarisation would represent a further significant contribution to our understanding of the universe.

Chapter 2 showed that behind most LNAs is the transistor, which owes its existence to discoveries in solid state physics. Over the last few decades our understanding of the transistor has advanced considerably and it is now possible design transistors with noise temperatures close to (~ 3 times) the quantum noise limit. Through the use of an equivalent circuit model, these transistors can then be integrated into an LNA. There is some work however still to do in understanding the transistor's noise behaviour. Whilst, it is true that the 4 noise parameters if known allow the transistor's noise performance to be understood, unlike the equivalent circuit model they do not allow the noise generation mechanisms to be investigated. Pospieszalski's development of the equivalent noise tem-

peratures T_a , T_g , T_d allow some physical understanding of the noise behaviour within transistors to be gained. They also show that further cooling beyond the 20 K typically used for radio astronomy should be beneficial.

Chapter 3 confirmed this improvement in noise temperature for 2 MMIC based LNAs, finding that the noise reduced by a further $\sim 20\text{-}30\%$ when the devices were cooled from 20 K to less than 6 K. It would now be interesting to see whether this improvement is frequency dependent, since if it extends to W-band this would result in a 6-7 K improvement in the noise temperature of the lowest noise W-band LNAs currently in existence. The small reduction in the bias point required for minimum noise is also of interest and worthy of further study.

Chapter 4 illustrated the importance of developing a high quality low noise transistor and how it alone can dramatically lower the noise temperature of a MMIC based LNA. Whilst there are very good MMIC LNAs available, some which even possess noise temperatures close to that of the T+MMIC LNA, they are very expensive and time consuming to develop. This is potentially OK for small scale arrays but could prove problematic for arrays requiring several 1000 LNAs (the QUIET phase 2 proposal called for a receiver with 750 pixels with 2 channels per pixel, 2 LNAs per channel and 2 MMICs per LNA making over 6000 LNAs (including spares)). The successful development of the T+MMIC however shows that rather than spending considerable money developing a very low noise MMIC LNA, or fabricating a time consuming MIC LNA, it is possible to get very low noise performance by using just a single low noise transistor. This paves the way for the potential use of cheap commercial MMICs in conjunction with specially developed transistors.

Finally, Chapter 5 outlined an approach for developing and combining the techniques outlined in Chapters 3 and 4 to produce what could be the lowest noise Ka-band LNA ever developed. A new design for a test cryostat was also presented and the design has the potential to be developed into a receiver system.

6.2 The Future

Over the last few decades there have been great advances in LNA technology and receivers in general. Looking to the future there are in addition to the areas outlined in this thesis three other areas that may offer further improvements in the overall sensitivity of receivers:

- Increasing the number of receivers.
- The transistors themselves.
- New types of Amplifier

6.2.1 Increasing the Number of Receivers

The first of these is relatively straightforward with QUIET showing that building a relatively large N array is feasible. However, incorporating the ideas expressed in Chapters 3 and 4 will not be easy but Chapter 5 has outlined a potential development route.

6.2.2 Transistors

Further developments in transistor technology, such as: smaller gate lengths, the development of very high electron mobility InSb devices, new resists for transistors. new transistor architectures and new techniques (such as the cooling of electrons) could also all lead to further reductions in LNA noise temperature.

Transistors with 35 nm gate lengths [147] and below [87] have already been developed and whilst they may not improve noise temperatures at all frequencies due to other device parasitics [148], they will have a part to play in future HEMT based CMB observatories. Developing even shorter gate lengths however is going to need the development of new resists and manufacturing techniques. As was outlined in section 2.4.3 the transistor is currently T-shaped and this is done to enable a small gate length whilst ensuring that the

transistor has sufficient cross-sectional area to carry the necessary current. Clearly a gate length will be reached where it will be unable to support the upper part of the structure causing failure, such as in figure 6.2.1.

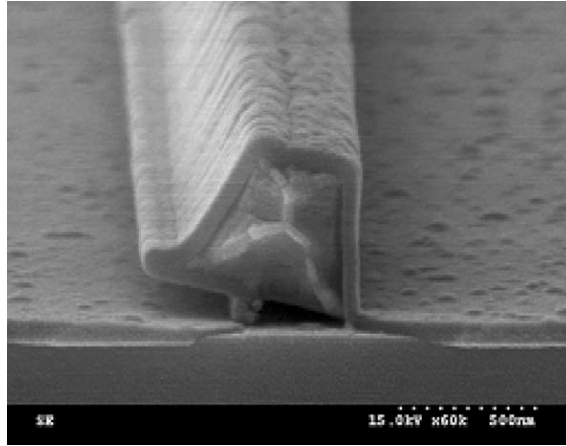


Figure 6.2.1: A collapsed T-gate. Figure 5 from [149].

At present small gate length transistors are fabricated using two or more resists that are arranged in a series of layers [149]. One reason that this is done is that when the resists are written with an electron beam, the electrons scatter within the resist [150] and this limits the ratio of gate height to gate length to about 4:1. New resists however, for example SML, may allow for the development of structures with considerably larger aspect ratios [151]. Increasing the aspect ratio may in turn allow for the development of an I-gate (figure 6.2.2), which could possess a gate length as small as 2 nm but with the structure being 1800 nm high, it would still possess the cross sectional area required to carry the necessary current.

Currently the transistors with the lowest noise are manufactured on InP and this is due to the high (when compared to GaAs) electron mobility of $\text{Ga}_{0.47}\text{In}_{0.53}\text{As}$. However, table 2.1 showed that InSb has an electron mobility 5 times higher than $\text{Ga}_{0.47}\text{In}_{0.53}\text{As}$, making it seem like an ideal candidate for use in future low noise transistors. At present research into InSb devices is still in its early stages, with research currently focussing on the potential use of InSb nanowires in FETs [152, 153].

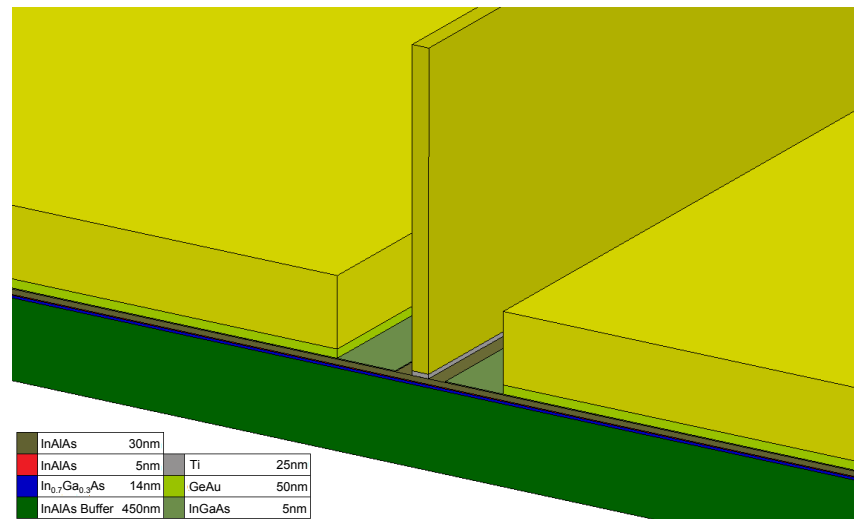


Figure 6.2.2: An impression of a potential future I-gate transistor.

Finally, superconductivity could be used to lower the resistance of the electrodes, indeed work in the 1990's [154] showed that using a superconducting gate lowered the noise temperature of a HEMT by a factor of three. For reasons that are unknown to the author there has however been very little research since then in this area, although the author is aware of renewed interest in the field by researchers at the Chalmers University of Technology in Sweden.

6.2.3 New Types of Amplifier

Superconductivity may also permit the development of completely new forms of LNA, including the potential for LNAs with noise temperatures at or below the quantum noise limit. In 2012 Byeong et al [155] outlined an amplifier comprising a high impedance, 0.8 m long super conducting TiN or NbTiN transmission line (figure 6.2.3). The amplifier which is also known as a travelling wave paramp exploits the non-linear kinetic inductance of a superconductor in order to mix an input signal and pump signal in such a way²⁹ that the input signal is amplified. The author is intending to look into these devices further.

²⁹Amplification is dependent on the travelling waves phase shifting by the correct amount as they pass along the structure, consequently the structure can also attenuate a signal.



Figure 6.2.3: 0.8 m long travelling wave superconducting parametric amplifier. From A New Kind of Amplifier [156].

6.3 Closing Remarks

This thesis set out to examine possible routes to the enhancement of LNA performance. Two such routes; enhanced cooling and the T+MMIC approach have shown promise and with further development have the potential to surpass the performance of the currently reported lowest noise LNA at Ka-band. It is now of great importance to carry on with this line of research, to use it to investigate the very low temperature behaviour of transistors and to extend it to other frequencies, in particular giving its importance to CMB observations W-band.

This thesis has also concluded by presenting a scheme that with not much effort could utilise the approaches outlined in this thesis to fabricate an amplifier with noise performance only 4 times higher than the quantum limit.



Figure 6.3.1: Dusk at the QUIET site, Atacama Desert, Chile.

Appendix A

Derivation of the RMS Thermal Noise

Voltage (V_n)

This proof follows the approach outlined by [157]. Consider the box, figure A.0.1; this box represents an ideal conductor, within the conductor there are lots of photons arising from thermal emission. These photons then induce motion in other electrons which generates an electric field. Other electrons then move to try and nullify this field, but resistance prevents them from fully achieving this. Thus a time varying random electric field is generated, which can be observed as a time varying voltage or noise. However, unlike the electrons the photons are not affected by the resistance and so the cavity can be treated as a perfect vacuum containing nothing but photons. Since photons possess integer spin the photons can be viewed as a Bose-Einstein gas, where the number of photons in a given energy state n_i is given by (A.0.1) the Bose-Einstein distribution function, with g_i equal to the number of possible degenerate states, ϵ_i is the energy of a particle in state i and μ the chemical potential.

$$n_i = \frac{g_i}{e^{(\epsilon_i - \mu)/kT} - 1} \quad (\text{A.0.1})$$

For photons g_i is 2 due to there being two polarisation states, ϵ_i is given by Planck's

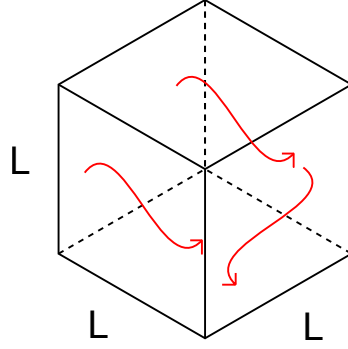


Figure A.0.1: A cuboidal blackbody cavity containing photons representing an ideal conductor.

formula for the energy of a photon (A.0.2), \hbar is the reduced Planck's constant \hbar , ω is the angular frequency and μ is 0. Thus (A.0.1), can be re-written as (A.0.3), and the expected energy per state is then given by (A.0.4).

$$\varepsilon_i = \hbar\omega \quad (\text{A.0.2})$$

$$n_i = \frac{2}{e^{(\hbar\omega)/kT} - 1} \quad (\text{A.0.3})$$

$$\langle E_i \rangle = n_i \varepsilon_i = \frac{2\hbar\omega}{e^{(\hbar\omega)/kT} - 1} \quad (\text{A.0.4})$$

The next step is to calculate the energy density which is given by (A.0.5), where $\frac{dn}{d\omega}d\omega$ is the density of states, which is the number of allowed energy states within a given volume, in this case the box L^3 .

$$U(\omega) = E(\omega) \frac{dn}{d\omega} d\omega \quad (\text{A.0.5})$$

In order to calculate the density of states it is convenient to treat the photons as electromagnetic waves, therefore they can be described by the classical wave equation (A.0.6).

$$\nabla^2 \mathbf{E} = \frac{1}{v^2} \frac{\delta^2 \mathbf{E}}{\delta t^2} \quad (\text{A.0.6})$$

Where \mathbf{E} the electric field is a function of x, y, z, t , however it is only necessary to

consider the one dimensional case and so (A.0.6) reduces to (A.0.7) which shows the wave equation for just the x component.

$$\frac{\delta^2 \mathbf{E}(x,t)}{\delta x^2} = \frac{1}{v^2} \frac{\delta^2 \mathbf{E}(x,t)}{\delta t^2} \quad (\text{A.0.7})$$

Considering the cavity; since the walls are perfect conductors the electric field component must be zero inside the walls, Maxwell's equations also require the fields to be continuous at each wall, therefore the following boundary conditions apply (A.0.8).

$$\mathbf{E}(x,t) = 0 \text{ for } x = 0, L \quad (\text{A.0.8})$$

Solving (A.0.7) using the separation of variables technique (where C is a constant) and the boundary conditions, (A.0.9g) shows that only certain frequencies are allowed.

$$\mathbf{E}(x,t) = X(x)T(t) \quad (\text{A.0.9a})$$

$$\frac{\delta^2 X}{\delta x^2} = -C^2 X \quad (\text{A.0.9b})$$

$$X(0) = X(L) = 0 \quad (\text{A.0.9c})$$

$$X(x) = A \cos Cx + B \sin Cx \quad (\text{A.0.9d})$$

$$\text{For } x = 0 \quad X(0) = A = 0 \quad (\text{A.0.9e})$$

$$\text{For } x = L \quad X(L) = B \sin CL = 0 \quad (\text{A.0.9f})$$

$$C = k_n = \frac{n\pi}{L} = \frac{2n\pi f}{v} \quad \text{for } n = 1, 2, 3 \quad (\text{A.0.9g})$$

This result where k_n is the wavenumber can now be used to calculate the density of states $D(\omega)$:

$$D(\omega)d\omega = \frac{1}{L} \frac{dn}{d\omega} = \frac{1}{L} \frac{dn}{dk_n} \frac{dk_n}{d\omega_n} d\omega = \frac{1}{L} \frac{L}{2\pi} \frac{1}{v} d\omega = \frac{d\omega}{2\pi} \quad (\text{A.0.10})$$

The energy density is then given by (A.0.11)

$$U(\omega) = E(\omega)D(\omega)d\omega \quad (\text{A.0.11})$$

$$U(\omega) = \frac{1}{2\pi} \frac{2\omega}{e^{\hbar\omega/kT} - 1} d\omega \quad (\text{A.0.12})$$

This can be used to calculate the power by calculating the energy flow into or out of the conductor, which is half the energy multiplied by the velocity.

$$P(\omega) = \frac{1}{2} v U(\omega) = \frac{1}{2\pi} \frac{2\omega}{e^{\hbar\omega/kT} - 1} d\omega \quad (\text{A.0.13})$$

this can be converted to a voltage and ω can be converted to frequency.

$$V = \sqrt{PR} = \sqrt{\frac{4hf}{e^{\hbar f/kT} - 1} df} \quad (\text{A.0.14})$$

Which if integrated with respect to f for a given bandwidth B gives

$$V = \sqrt{PR} = \sqrt{\frac{4hfBR}{e^{\hbar f/kT} - 1}} \quad (\text{A.0.15})$$

At microwave frequencies however, $\frac{\hbar f}{kT}$ is very close to zero and so by using a Taylor expansion (A.0.16), it can be shown that equation (A.0.15) simplifies to equation (A.0.18) which is (2.6.1) as required.

$$f(x) = f(0) + \frac{f'(0)}{1!} + \frac{f''(0)}{2!} + \frac{f'''(0)}{3!} + \dots \quad (\text{A.0.16})$$

$$e^{\hbar f/kT} \approx 1 + \frac{\hbar f}{kT} \quad (\text{A.0.17})$$

$$V_n = \sqrt{4kTBR} \quad (\text{A.0.18})$$

As required.

Appendix B

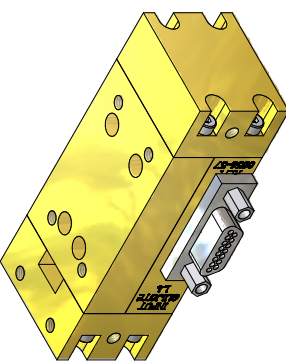
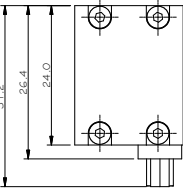
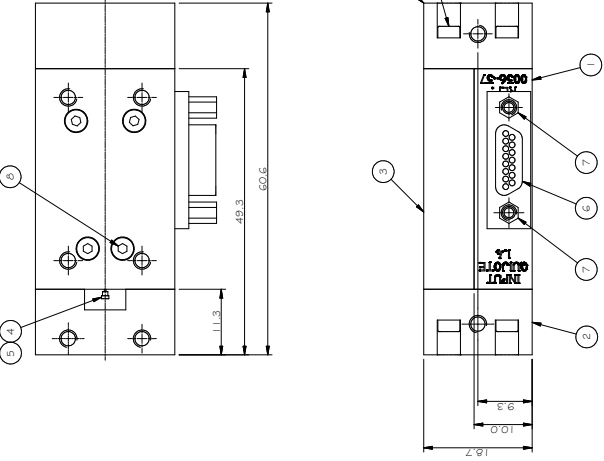
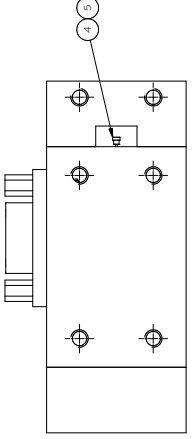
T+MMIC LNA Module: Designs

APPENDIX B. T+MMIC LNA MODULE: DESIGNS

Parts List		
ITEM	QTY	DESCRIPTION
1	1	PRE-MMIC TRANSISTOR LNA BODY
2	2	PRE-MMIC TRANSISTOR LNA END CAP
3	1	PRE-MMIC TRANSISTOR LNA LID
4	2	QUICOTE RF PROBE
5	2	QUICOTE RF PROBE INSULATOR
6	1	CINCH 15-PIN PLUG MICRO D CONNECTOR
7	2	2-56 UNC JACK SCREW
8	12	M2 x 10 LONG SOCKET HEAD CAPSCREW

ITEM	QTY	DESCRIPTION	PART NUMBER	MATERIAL
1	1	PRE-MMIC TRANSISTOR LNA BODY	0036-37	Brass
2	2	PRE-MMIC TRANSISTOR LNA END CAP	0036-30	Brass
3	1	PRE-MMIC TRANSISTOR LNA LID	0036-36	Brass
4	2	QUICOTE RF PROBE	0036-17 ITEM 1	Brass
5	2	QUICOTE RF PROBE INSULATOR	0036-17 ITEM 2	PTFE
6	1	CINCH 15-PIN PLUG MICRO D CONNECTOR		Stainless Steel
7	2	2-56 UNC JACK SCREW		Stainless Steel
8	12	M2 x 10 LONG SOCKET HEAD CAPSCREW		Stainless Steel

NOTE:
ENSURE ALL SURFACES ARE FLAT AND
TIGHT WITH ADJACENT FACE

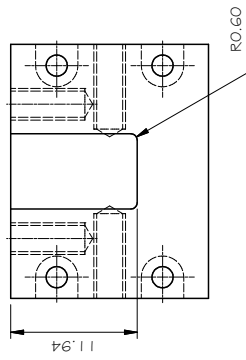
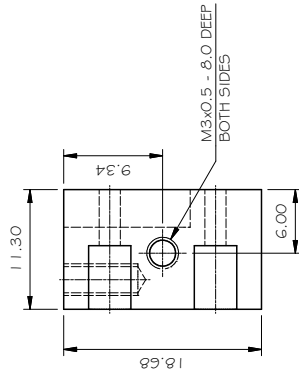
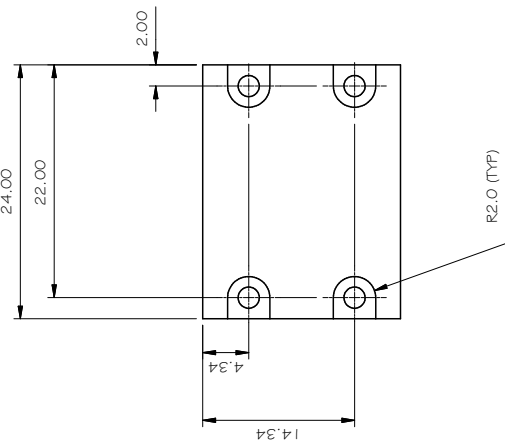
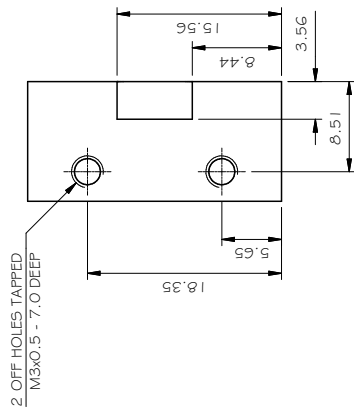
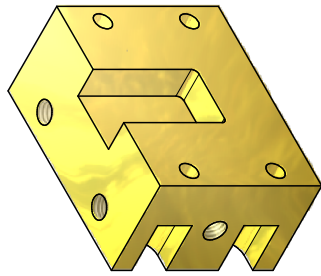





Designed by	Checked by	Approved by	Date	Scale
Adrian Guller		PODBELL BANK OBSERVATORY UNIVERSITY OF MANCHESTER MACCLESFIELD SKEWTON SK11 9BU	07/12/2010	2:1

DESIGNED BY	TITLE	REVISION
UNLESS OTHERWISE STATED ALL DIMENSIONS IN MILLIMETRES UNLESS OTHERWISE STATED	QUICOTE L4 - PRE-MMIC TRANSISTOR LNA - ARRANGEMENT DRAWING	1 / 1

Parts List		DESCRIPTION	MATERIAL
ITEM	QTY	30 x 25 x 1/2" THK PLATE	CZ12IM, BRASS
1	1		

GEOMETRIC REQUIREMENTS:
 ENSURE ALL OF THE FOLLOWING:
 - ALL EDGES ARE SQUARE UNLESS OTHERWISE STATED.
 - ALL FACES ARE FLAT.
 - ALL FACES ARE SMOOTH.
 - ALL HOLES ARE PERPENDICULAR TO FACE.
 - ALL COUNTERBORED HOLES ARE CONCENTRIC UNLESS OTHERWISE STATED.



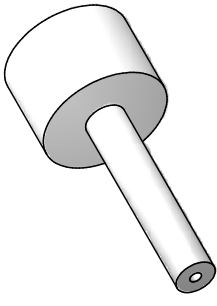
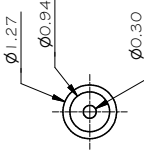
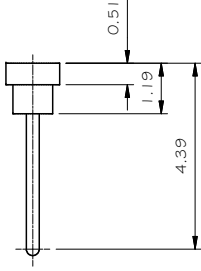
REV	DESCRIPTION	DATE	MODIFIED BY
REVISION HISTORY			
		Date	Scale
		09/07/2009	2.5:1

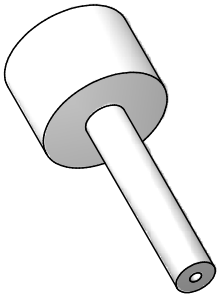
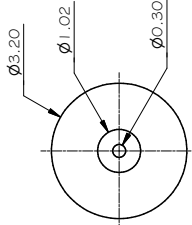
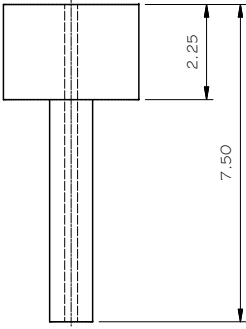
Designed by Adrian Galtriss	Checked by	Approved by	Date
GENERAL TOLERANCE WHOLE NUMBERS ± 0.25 1 DECIMAL PLACE ± 0.10 2 DECIMAL PLACES ± 0.05 ALL ANGLES $\pm 0.10^\circ$ ALL DIMENSIONS IN MILLIMETRES UNLESS OTHERWISE STATED	JODRELL BANK OBSERVATORY UNIVERSITY OF MANCHESTER MACCLESFIELD CHESHIRE SK11 9DL TEL: 01477 571321 FAX: 01477 571618		
MACHINED SURFACES TO UNLESS OTHERWISE STATED		TITLE	
		QUIJOTE 1.3 - END CAP	
		DRAWING NUMBER	Revision
		CO36-30	1 / 1

APPENDIX B. T+MMIC LNA MODULE: DESIGNS

Parts List		ITEM	QTY	DESCRIPTION	MATERIAL
		1	1	1/16" DIA ROD x 1" LONG	B52874 CZ12 IM BRASS
		2	1	1/4" DIA BAR x 1" LONG	PTFE

SURFACE FINISH
 5µm SOFT PURE GOLD ON
 5µm NICKEL TO DEF STAN 03-172

MACHINED SURFACES TO \sqrt{V} UNLESS OTHERWISE STATED			Designed by Adrian Galtress	Checked by	Approved by	Date	Scale	REVISED HISTORY	DATE	MODIFIED BY
GENERAL TOLERANCE WHOLE NUMBERS ± 0.25 1 DECIMAL PLACE ± 0.10 2 DECIMAL PLACES ± 0.05 ALL ANGLES $\pm 0.10^\circ$ ALL DIMENSIONS IN MILLIMETRES UNLESS OTHERWISE STATED			JODRELL BANK OBSERVATORY UNIVERSITY OF MANCHESTER MACCLESFIELD CHESHIRE SK11 9DL TEL: 01477 571321 FAX: 01477 571618			TITLE QUIJOTE - RF PROBE & INSULATION FOR FEM		DRAWING NUMBER 0036-17		Revision 1 / 1

Bibliography

- [1] F. Piacentini et al. The boomerang north america instrument: a balloon-borne bolometric radiometer optimized for measurements of cosmic background radiation anisotropies from 0.3° to 4° . *Astrophysical Journal Supplement Series*, 138(2):315 – 36, 2002.
- [2] B.P. Crill et al. Spider: A balloon-borne large-scale cmb polarimeter. volume 7010, pages The International Society for Optical Engineering (SPIE); SPIE Europe –, Marseille, France, 2008.
- [3] C.R. Lawrence et al. Millimeter-wave mmic cameras and the experiment. In *Proceedings of the SPIE - The International Society for Optical Engineering. (USA)*, volume 5498, pages 220 – 31, USA, 2004.
- [4] T. L. Wilson. *Tools of Radio Astronomy*. 5th edition.
- [5] C. M. Caves. Quantum limits on noise in linear amplifiers. *Phys. Rev. D*, 26:1817–1839, Oct 1982.
- [6] A. Martinez. Quantum noise in linear amplifiers revisited. In *Information Sciences and Systems, 2006 40th Annual Conference on*, pages 1690–1690, 2006.
- [7] V.M. Slipher. Two Nebulae with Unparalleled Velocities. *Popular Astronomy*, 29:128, 1921.

BIBLIOGRAPHY

- [8] A. Einstein. The basis of the general theory of relativity. *Annalen der Physik*, 49(7):769 – 822, 1916.
- [9] A. Einstein. Cosmological deductions from the general theory of relativity. *Abhandlungen der Preussischen Akademie der Wissenschaften*, 6:142 – 152, 1917.
- [10] W. de Sitter. Curvature of space. *Proceedings Koninklijke Akademie van Wetenschappen te Amsterdam*, 20(2):229 – 343, 1917.
- [11] J. Mather. From the big bang to the nobel prize and the james webb space telescope. *Il Nuovo cimento. B*, 122(12):1315–1326, 2007.
- [12] A. Friedman. On the curvature of space. *Zeitschrift fur Physik*, 10(6):377 – 386, 1922.
- [13] G.H. Lemaitre. *The Gravitational Field in a Fluid Sphere of Uniform Invariant Density, According to the Theory of Relativity*. PhD thesis, MASSACHUSETTS INSTITUTE OF TECHNOLOGY, 1927.
- [14] E. Hubble. Distance and radial velocity among extra-galactic nebulae. *Proceedings of the National Academy of Sciences of the United States of America*, 15:168 – 173, 1929.
- [15] A. Einstein and W. de Sitter. Expansion and the mean density of the universe. *Proceedings of the National Academy of Sciences of the United States of America*, 18:213 – 214, 1932.
- [16] W.S. Adams. Results with the coude spectrograph of the mt. wilson observatory. *Astrophysical Journal*, 93:11 – 23, 1941.
- [17] A. McKellar. The problems of possible molecular identification for interstellar lines. *Publications of the Astronomical Society of the Pacific*, 53:233–235, August 1941.

- [18] D.T. Wilkinson and P.J.E. Peebles. Discovery of the cosmic microwave background. volume T85, pages 136 – 41, Sweden, 2000.
- [19] G. Gamow. Expanding universe and the origin of elements. *Physical Review*, 70:572 – 573, 1946.
- [20] R.A. Alpher et al. The origin of chemical elements. *Physical Review*, 73:803 – 804, 1948.
- [21] G. Gamow. The origin of elements and the separation of galaxies. *Physical Review*, 74:505 – 506, 1948.
- [22] R.A. Alpher and R. Herman. Evolution of the universe. *Nature*, 162:774 – 775, 1948.
- [23] F. Hoyle. A new model for the expanding universe. *Monthly Notices of the Royal Astronomical Society*, 108(5):372 – 382, 1948.
- [24] J.A. Wheeler. *Geometrodynamics and the issue of the final state, in Relativity Groups and Topology*. Gordon and Breach, Blackie, 1964.
- [25] R.H. Dicke et al. Cosmic black-body radiation. *Astrophysical Journal*, 142(1):414 – 419, 1965.
- [26] A.A. Penzias and R.W. Wilson. A measurement of excess antenna temperature at 4080 mc/s. *Astrophysical Journal*, 142:419–421, 1965.
- [27] R.W. Wilson. The cosmic microwave background radiation. *Nobel Lectures*, 1978.
- [28] S. Weinberg. *The first three minutes : a modern view of the origin of the universe*. Basic Books, New York, updated edition, 1993.
- [29] W.J. Tabor and J.T. Sibilila. Masers for the telstar satellite communications experiment. *Bell System Technical Journal*, 42:1863–1886, 1963.

BIBLIOGRAPHY

- [30] A. E. Lange. Detectors for future cmb observations. In *FAR-IR, SUB-MM & MM DETECTOR TECHNOLOGY WORKSHOP*, 2002.
- [31] G.F. Smoot. Cobe observations and results. Number 476, pages 1 – 10, USA, 1999.
- [32] D.J. Fixsen et al. The cosmic microwave background spectrum from the full cobe firas data set. *Astrophysical Journal*, 473:576–87, 1996.
- [33] M. J. Devlin et al. Mapping the Cosmic Microwave Background Anisotropy:The First Flight of the QMAP Experiment. *The Astrophysical Journal*, 1998.
- [34] A. Miller et al. The QMAP and MAT/TOCO Experiments for Measuring Anisotropy in the Cosmic Microwave Background. *The Astrophysical Journal Supplement Series*, 2002.
- [35] A.E. Lange et al. Cosmological parameters from the first results of boomerang. *Physical Review D*, 63(4):042001 – 1, 2001.
- [36] P. de Bernardis et al. Mapping the cmb sky: The boomerang experiment. In *New Astronomy Reviews*, volume 43, pages 289 – 96, Netherlands, 1999.
- [37] NASA/WMAP Science Team. 5 year cmb angular power spectrum, 2011. <http://map.gsfc.nasa.gov/media/080999/index.html>.
- [38] The Planck Team. Planck scientific program, 2005.
- [39] R. Hu and S. Weinreb. A novel wide-band noise-parameter measurement method and its cryogenic application. *Microwave Theory and Techniques, IEEE Transactions on*, 52(5):1498 – 1507, 2004.
- [40] L. Verde. Cosmological implications of the first year wilkinson microwave anisotropy probe results. In *International Journal of Modern Physics A*, volume 19, pages 1121 – 31, Singapore, 2004.

- [41] NASA/WMAP Science Team. 9 year microwave sky, 2012.
<http://map.gsfc.nasa.gov/media/121238/index.html>.
- [42] M. Robson et al. The cosmic anisotropy telescope. *Astronomy and Astrophysics*, 277:314, 1993.
- [43] K. Grainge et al. The cosmic microwave background power spectrum out to $l=1400$ measured by the Very Small Array. *Monthly Notices of the Royal Astronomical Society*, 2003.
- [44] R. A. Watson et al. First results from the Very Small Array - I. Observational methods. *Monthly Notices of the Royal Astronomical Society*, 2003.
- [45] J. W. Fowler et al. The Atacama Cosmology Telescope: A Measurement of the $600 < l < 8000$ Cosmic Microwave Background Power Spectrum at 148 GHz. *The Astrophysical Journal*, 2010.
- [46] J. L. Sievers et al. The Atacama Cosmology Telescope: cosmological parameters from three seasons of data. *Journal of Cosmology and Astroparticle Physics*, 2013.
- [47] J. Tauber et al. Simple but challenging: the universe according to planck, 2013.
<http://sci.esa.int/planck/51551-simple-but-challenging-the-universe-according-to-planck>.
- [48] ESA. Planck cmb, 2013.
http://spaceimages.esa.int/Images/2013/03/Planck_CMB.
- [49] D. Baumann et al. Cmbpol mission concept study: Probing inflation with cmb polarization. volume 1141, pages 10 – 120, USA, 2009.
- [50] S. Weinberg. *Cosmology*. Oxford University Press, 2nd edition, 2008.

BIBLIOGRAPHY

- [51] S. Dodelson et al. The Origin of the Universe as Revealed Through the Polarization of the Cosmic Microwave Background, 2009.
- [52] W. Hu and M. White. A cmb polarization primer. *New Astronomy*, 2(4):323 – 44, 1997.
- [53] M. Bowden et al. Scientific optimization of a ground-based cmb polarization experiment. *Monthly Notices of the Royal Astronomical Society*, 349(1):321 – 35, 2004.
- [54] W. Hu. Wayne hu’s homepage.
<http://background.uchicago.edu/~whu>.
- [55] B.F. Burke and F.S. Graham-Smith. *An introduction to radio astronomy*. Cambridge University Press, Cambridge, 2nd edition.
- [56] T.C. Gaier. Coherent radiometers for cosmic microwave background polarization detection. volume 4843, pages 296 – 304, USA, 2003.
- [57] L. Piccirillo et al. Quiet phase 2 proposal.
- [58] W. Hu. Cmb temperature and polarization anisotropy fundamentals. *Annals of Physics*, 303(1):203 – 25, 2003.
- [59] J.M. Kovac et al. Detection of polarization in the cosmic microwave background using dasi. *Nature*, 420(6917):772 – 787, 2002.
- [60] E.M. Leitch et al. Experiment design and first season observations with the degree angular scale interferometer. *Astrophysical Journal*, 568(1):28 – 37, 2002.
- [61] E.M. Leitch et al. Measurement of polarization with the degree angular scale interferometer. *Nature*, 420(6917):763 – 771, 2002.

- [62] J. R. Hinderks et al. QUaD: A High-Resolution Cosmic Microwave Background Polarimeter. *The Astrophysical Journal*, 692:1221–1246, 2009.
- [63] C. Pryke et al. Second and third season quad cosmic microwave background temperature and polarization power spectra. *The Astrophysical Journal*, 692(2):1247, 2009.
- [64] S. Padin et al. The Cosmic Background Imager. *The Publications of the Astronomical Society of the Pacific*, 114:83–97, January 2002.
- [65] A. C. S. Readhead et al. Polarization Observations with the Cosmic Background Imager. *Science*, 306:836–844, October 2004.
- [66] I. Buder. Q/u imaging experiment (quiet): A ground-based probe of cosmic microwave background polarization. In *Proceedings of SPIE - The International Society for Optical Engineering*, volume 7741, San Diego, CA, United states, 2010.
- [67] K. A. Cleary. Coherent polarimeter modules for the quiet experiment. In *Millimeter, Submillimeter, and Far-Infrared Detectors and Instrumentation for Astronomy V*, volume 7741, page 77412H. SPIE, 2010.
- [68] C. Bischoff et al. First season quiet observations: Measurements of cosmic microwave background polarization power spectra at 43 ghz in the multipole range 25 1 475. *Astrophysical Journal*, 741(2):111 (18 pp.) –, 2011.
- [69] A. Kogut. WMAP polarization results. *New Astronomy Reviews*, 47:977–986, December 2003.
- [70] L. Page et al. Three-Year Wilkinson Microwave Anisotropy Probe (WMAP) Observations: Polarization Analysis. *The Astrophysical Journal Supplement Series*, 170:335–376, June 2007.

BIBLIOGRAPHY

- [71] D.L. Pulfrey et al. *Introduction to Microelectron Devices*. Prentice-Hall, Englewood Cliff, NJ, 2nd edition.
- [72] J.J. Bautista. Cryogenic, low-noise high electron mobility transistor amplifiers for the deep space network. *The Telecommunications and Data Acquisition Progress Report*, 42-115:65–80, 1993.
- [73] I.D. Robertson. *RFIC and MMIC Design Technology*. The Institution of Electrical Engineers, London, UK, 2nd edition.
- [74] J. J. Bautista. *Low-Noise Systems in the Deep Space Network*, volume 10, chapter 5. NASA JPL, Pasadena, CA, 2013.
- [75] W. Shockley. A unipolar "field-effect" transistor. *Proceedings of the IRE*, 40(11):1365–1376, 1952.
- [76] D.N. McQuiddy et al. Monolithic microwave integrated circuits: An historical perspective. *Microwave Theory and Techniques, IEEE Transactions on*, 32(9):997–1008, 1984.
- [77] G. E. Ponchak. Metal-semiconductor junctions, 2009.
http://people.sabanciuniv.edu/burc/SU%20web%20material_files/MAT%20509%20Material/m-sc%20contact/3-ii.pdf.
- [78] J. M. Golio. *Microwave Mesfets and HEMTs*, chapter 1. Artech House, Norwood, MA, 2nd edition, 1991.
- [79] T. Mimura et al. A new field-effect transistor with selectively doped $\text{GaAs/n-Al}_x\text{Ga}_{1-x}\text{As}$ heterojunctions. *Japanese Journal of Applied Physics*, 19(5):L225–L227, 1980.

- [80] M.W. Pospieszalski et al. Noise parameters and light sensitivity of low-noise high-electron-mobility transistors at 300 and 12.5 k. *Electron Devices, IEEE Transactions on*, 33(2):218–223, 1986.
- [81] C. Matthai and R. H. Williams. *Physics and Technology of Heterojunction Devices*, chapter 1. Peter Peregrinus, London UK, 1st edition, 1991.
- [82] P. J. Tasker. *Physics and Technology of Heterojunction Devices*, chapter 5. Peter Peregrinus, London UK, 1st edition, 1991.
- [83] A.J. Hill and P.H. Ladbroke. High electron mobility transistors (hemts)-a review. *GEC Journal of Research Incorporating the Marconi Review*, 4(1):1 – 14, 1986.
- [84] T.J. Drummond et al. Modulation-doped gaas/(al,ga)as heterojunction field-effect transistors: Modfets. *Proceedings of the IEEE*, 74(6):773 – 822, 1986.
- [85] F. Ali and A. Gupta. *HEMTs and HBTs: devices, fabrication and circuits*. Artech House, London, first edition, 1991.
- [86] Cornell nanoScale Science & Technology Facility. Advanced electron beam lithography processes, 2013.
http://www.cnf.cornell.edu/cnf_process_ebl_advanced.html.
- [87] A. Leuther et al. 20 nm metamorphic hemt with 660 ghz ft, 2011.
- [88] E.W. Bryerton et al. A w-band low-noise amplifier with 22k noise temperature. In *Microwave Symposium Digest, 2009. MTT '09. IEEE MTT-S International*, pages 681–684, 2009.
- [89] M.W. Pospieszalski et al. Fet's and hemt's at cryogenic temperatures their properties and use in low noise amplifiers. *Microwave Theory and Techniques, IEEE Transactions on*, 36(3):552 –560, 1988.

BIBLIOGRAPHY

- [90] M. Berroth and R. Bosch. Broad-band determination of the fet small-signal equivalent circuit. *IEEE Transactions on Microwave Theory and Techniques*, 38(7):891–5, 1990.
- [91] G. Dambrine et al. A new method for determining the fet small-signal equivalent circuit. *Microwave Theory and Techniques, IEEE Transactions on*, 36(7):1151–1159, 1988.
- [92] R. Tayrani et al. A new and reliable direct parasitic extraction method for mesfets and hemts. pages 451–453, sep. 1993.
- [93] J. B. Johnson. Thermal agitation of electricity in conductors. *Phys. Rev.*, 32:97–109, 1928.
- [94] H. Nyquist. Thermal agitation of electric charge in conductors. *Phys. Rev.*, 32:110–113, 1928.
- [95] S. et al Prasad. *High-Speed Electronics and Optoelectronics: Devices and Circuits*. Cambridge University Press, Cambridge, UK, 1st edition.
- [96] A. van der Ziel. Thermal noise in field-effect transistors. *Proceedings of the IRE*, 50(8):1808–1812, 1962.
- [97] A. Van Der Ziel. Gate noise in field effect transistors at moderately high frequencies. *Proceedings of the IEEE*, 51(3):461–467, march 1963.
- [98] N. Jarosik et al. Design, Implementation, and Testing of the Microwave Anisotropy Probe Radiometers. *The Astrophysical Journal Supplement Series*, 145:413–436, April 2003.
- [99] H. Fukui. Design of microwave gaas mesfet's for broad-band low-noise amplifiers. *Microwave Theory and Techniques, IEEE Transactions on*, 27(7):643–650, 1979.

- [100] A. Cappy and W. Heinrich. High-frequency fet noise performance: a new approach. *Electron Devices, IEEE Transactions on*, 36(2):403–409, 1989.
- [101] R.A. Pucel et al. Signal and noise properties of gallium arsenide microwave field-effect transistors. *Advances in Electronics and Electron Physics*, 38:195–265, 1975.
- [102] M.W. Pospieszalski. Modeling of noise parameters of mesfets and modfets and their frequency and temperature dependence. *Microwave Theory and Techniques, IEEE Transactions on*, 37(9):1340–1350, 1989.
- [103] M.W. Pospieszalski. Interpreting transistor noise. *Microwave Magazine, IEEE*, 11(6):61–69, oct. 2010.
- [104] M.W. Pospieszalski. On the measurement of noise parameters of microwave two-ports (short paper). *Microwave Theory and Techniques, IEEE Transactions on*, 34(4):456–458, 1986.
- [105] M.W. Pospieszalski. A new approach to modeling of noise parameters of fet's and modfet's and their frequency dependence. Technical Report 279, National Radio Astronomy Observatory Electronics Division, 1988.
- [106] M.R. Murti et al. Temperature-dependent noise parameters and modeling of inp/inalas/ingaas hemts. In *Microwave Symposium Digest., 2000 IEEE MTT-S International*, 2000.
- [107] M.R. Murti et al. Temperature-dependent small-signal and noise parameter measurements and modeling on inp hemts. *Microwave Theory and Techniques, IEEE Transactions on*, 48(12):2579–2587, 2000.
- [108] M.W. Pospieszalski. Extremely low-noise amplification with cryogenic fets and hfets: 1970-2004. *Microwave Magazine, IEEE*, 6(3):62–75, sept. 2005.

BIBLIOGRAPHY

- [109] A. Endoh et al. Monte carlo simulations of electron transport in $\text{in}_{0.52}\text{al}_{0.48}\text{as}/\text{in}_{0.75}\text{ga}_{0.25}\text{as}$ high electron mobility transistors at 300 and 16k. *Japanese Journal of Applied Physics*, 49(11):114301, 2010.
- [110] J.J. Bautista et al. Cryogenic, x-band and ka-band inp hemt based Inas for the deep space network. In *Aerospace Conference, 2001, IEEE Proceedings.*, 2001.
- [111] A. Chincarini et al. Gain and noise analysis of hemt amplifiers from room temperature to superfluid he. *Classical and Quantum Gravity*, 23(8):S293, 2006.
- [112] QUIET II Module Development Program. Temperature hemts. private communication, 2010.
- [113] S. Munoz et al. Drain temperature dependence on ambient temperature for a cryogenic low noise c-band amplifier. In *Microwave Conference, 1997. 27th European*, volume 1, pages 114 –118, sept. 1997.
- [114] K. H. Duh et al. 32-ghz cryogenically cooled hemt low-noise amplifiers. *Electron Devices, IEEE Transactions on*, 36(8):1528–1535, 1989.
- [115] M.W. Pospieszalski et al. Very low noise and low power operation of cryogenic alinas/gainas/inp hfet's. In *Microwave Symposium Digest, 1994., IEEE MTT-S International*, volume 3, pages 1345 –1346, may 1994.
- [116] C.F. Whiteside et al. Velocity fluctuation noise measurements on algaas gaas interfaces. *Electron Devices, IEEE Transactions on*, 34(12):2530 – 2534, 1987.
- [117] J. L. Cano. *Cryogenic Technology in the Microwave Engineering: Application to MIC and MMIC Very Low Noise Amplifier Design*. PhD thesis, UNIVERSIDAD DE CANTABRIA, 2010.
- [118] ANSYS. Ansys hfss, 2013.
<http://www.ansys.com>.

- [119] R.H. Dicke. The measurement of thermal radiation at microwave frequencies. *Review of Scientific Instruments*, 17:268 – 275, 1946.
- [120] S.J. Melhuish et al. Lna noise behaviour below 10k physical temperature. In *Microwave Integrated Circuits Conference (EuMIC), 2012 7th European*, pages 393–396, 2012.
- [121] Yu-Lung Tang et al. Full ka-band high performance inp mmic lna module. In *Microwave Symposium Digest, 2006. IEEE MTT-S International*, pages 81–84, 2006.
- [122] M. A. McCulloch et al. A low noise ka-band amplifier for radio astronomy. In *Microwave Conference (EuMC), 2012 42nd European*, pages 1261–1264, 2012.
- [123] J. Schlee et al. Cryogenic broadband ultra-low-noise mmic lnas for radio astronomy applications. *Microwave Theory and Techniques, IEEE Transactions on*, 61(2):871–877, 2013.
- [124] R.J. Davis et al. Design, development and verification of the 30 and 44 ghz front-end modules for the planck low frequency instrument. *Journal of Instrumentation*, 4(12):T12002 (36 pp.), 2009.
- [125] D. M. Pozar. *Microwave Engineering*. Wiley, Hoboken, NJ, third edition, 2005.
- [126] Polyflon Company. Polyflon cuflon data sheet.
- [127] J.A. Hejase et al. Terahertz characterization of dielectric substrates for component design and nondestructive evaluation of packages. *Components, Packaging and Manufacturing Technology, IEEE Transactions on*, 1(11):1685–1694, 2011.
- [128] I.D. Robertson. *RFIC and MMIC Design Technology*. The Institution of Electrical Engineers, London, UK, 2nd edition.

BIBLIOGRAPHY

- [129] Tom M. Hyltin. Microstrip transmission on semiconductor dielectrics. *Microwave Theory and Techniques, IEEE Transactions on*, 13(6):777–781, 1965.
- [130] E.W. Mehal and R.W. Wacker. Gaas integrated microwave circuits. *Microwave Theory and Techniques, IEEE Transactions on*, 16(7):451–454, 1968.
- [131] B. Aja et al. Cryogenic low-noise mhemt-based mmic amplifiers for 4 -12 ghz band. 21(11):613 –615, nov. 2011.
- [132] H.T. Friis. Noise figures of radio receivers. *Proceedings of the IRE*, 32(7):419–422, 1944.
- [133] J. Shell. The cryogenic dc behavior of cryo3/az1 inp 0.1-by-80-micrometer-gate high electron mobility transistor devices, 2007.
- [134] M.W. Pospieszalski. Cryogenic amplifiers for jansky very large array receivers. In *Microwave Radar and Wireless Communications (MIKON), 2012 19th International Conference on*, volume 2, pages 748–751, 2012.
- [135] M. W Pospieszalski. Evaluation of q-band amplifiers modified with trw cryo3 80 μ m devices. private communication, 2004.
- [136] D. Kettle et al. A lattice matched inp chip set for a ka band radiometer. pages 4 pp. –, 2005.
- [137] Rubiño-Martín et al. The QUIJOTE CMB Experiment. In *Highlights of Spanish Astrophysics V*, page 127, 2010.
- [138] Agilent Technologies. Advanced design system 2009 update 1, 2009.
<http://www.home.agilent.com>.
- [139] M. W. Pospieszalski. Notes on modeling of five stage q-band amplifier using cryo-3 80 μ m hemts. private communication, 2004.

- [140] Agilent Technologies. *De-embedding and Embedding S-Parameter Networks Using a Vector Network Analyzer*, application note 1364-1 edition. <http://literature.agilent.com/litweb/pdf/5980-2784EN.pdf>.
- [141] M. A. McCulloch et al. A cryogenic ultra-low-noise mmic-based Ina with a discrete first stage transistor suitable for radio astronomy applications. Submitted IEEE MTT, 2013.
- [142] F. Winder. Comparison of hrl 50um and trw 80um inp hemt model values. private communication, 2002.
- [143] M.W. Pospieszalski et al. Millimeter-wave, cryogenically-coolable amplifiers using alinas/gainas/inp hemts. In *Microwave Symposium Digest, 1993., IEEE MTT-S International*, volume 2, pages 515 –518, 1993.
- [144] Yoke-Choy Leong and S. Weinreb. Full band waveguide-to-microstrip probe transitions. In *Microwave Symposium Digest, 1999 IEEE MTT-S International*, volume 4, pages 1435–1438 vol.4, 1999.
- [145] C. Risacher et al. Waveguide-to-microstrip transition with integrated bias-t. *Microwave and Wireless Components Letters, IEEE*, 13(7):262–264, 2003.
- [146] P. J. Meier. Two new integrated-circuit media with special advantages at millimeter wavelengths. In *Microwave Symposium, 1972 IEEE GMITT International*, pages 221–223, 1972.
- [147] X.B. Mei et al. 35nm inp hemt for millimeter and sub-millimeter wave applications. In *Indium Phosphide Related Materials, 2007. IPRM '07. IEEE 19th International Conference on*, pages 59–62, 2007.
- [148] T. Gaier. private communication, 2011.

BIBLIOGRAPHY

- [149] S.C. Kim et al. Sub-100 nm t-gate fabrication using a positive resist zep520/p(mma-maa)/pmma trilayer by double exposure at 50 kv e-beam lithography. *Materials Science in Semiconductor Processing*, 7(1-2):7 – 11, 2004.
- [150] S. Lewis et al. Characterization of an ultra high aspect ratio electron beam resist for nano-lithography. In *Nanotechnology 2010: Electronics, Devices, Fabrication, MEMS, Fluidics and Computational - Technical Proceedings of the 2010 NSTI Nanotechnology Conference and Expo, NSTI-Nanotech 2010*, volume 2, pages 195 – 198, Anaheim, CA, United states, 2010.
- [151] Mohammad Ali Mohammad, Steven K. Dew, and Maria Stepanova. Sml resist processing for high-aspect-ratio and high-sensitivity electron beam lithography. *Nanoscale Research Letters*, 8(1):1 – 7, 2013.
- [152] P. Caroff et al. High-quality inas/insb nanowire heterostructures grown by metalorganic vapor-phase epitaxy. *Small*, 4(7):878–882, 2008.
- [153] J. Sato et al. Analysis of performances of insb hemts using quantum-corrected monte carlo simulation. In *Indium Phosphide and Related Materials (IPRM), 2012 International Conference on*, pages 237–240, 2012.
- [154] L.O.A. Myer et al. A comparative study of the noise performance of aluminium-gallium-arsenide/gallium-arsenide high electron mobility transistors with and without superconducting gate electrodes. *Electron Device Letters, IEEE*, 13(5):273–275, 1992.
- [155] B. Ho Eom et al. A wideband, low-noise superconducting amplifier with high dynamic range. *Nature Physics*, 8:623–627, August 2012.
- [156] M. Woo. A new kind of amplifier, 2012.
<http://www.caltech.edu/content/new-kind-amplifier>.

- [157] C. S. Turner. Johnson-nyquist noise. Technical Report V15, Wireless Systems Engineering, 2007.